Insights into The Role of Conformational Change, Membrane Interactions and ATP Hydrolysis in The Min Protein Regulators of Bacterial Cell Division

By

Saud Ayed

A thesis submitted to the
Faculty of Graduate & Postdoctoral Studies
In partial fulfillment of the requirements for the
Doctorate in Philosophy degree in Chemistry

Department of Chemistry and Biomolecular Sciences
Faculty of Science
University of Ottawa

uOttawa

Candidate

Supervisor

Saud Ayed

Natalie K. Goto

Abstract

The bacterial cell division regulators MinD and MinE together with the division inhibitor MinC undergo coordinated pole-to-pole oscillation to help ensure that the cytokinetic division septum forms only at the mid-cell position. This dynamic localization is driven by MinD-catalyzed ATP hydrolysis, stimulated by interactions with the MinE anti-MinCD domain. This domain is buried in the 6-β–stranded MinE "closed" structure, but is liberated for interactions with MinD, giving rise to a 4-β–stranded "open" structure. Questions remain regarding how MinE undergoes this conformational change and whether the membrane plays a role in modulating MinD and MinE structure and function. In this thesis we investigated these questions using a combination of enzyme kinetics, circular dichroism spectroscopy and solution NMR spectroscopy. We showed that membrane binding induces a structural change in MinE that resembles the open conformation. However, MinE mutants lacking the MinE membrane-targeting sequence (ΔMTS) stimulated higher ATP hydrolysis rates than the full-length protein, indicating that direct interactions between MinE and the membrane are not required to trigger this conformational transition in MinE. These results led to an updated model where MinE is brought to the membrane through interactions with MinD and remains bound to the membrane in a state that does not catalyze additional rounds of ATP hydrolysis. Solution NMR was used to study the interaction between MinE and MinD, both in the presence and absence of lipid membranes. Our results suggest that conserved MinE residues in a loop region may interact weakly with MinD before conformational change is induced in MinE. In addition, we found that the membrane charge and fluidity, but not curvature, can modulate MinD activity, with faster rates being observed for membranes containing negatively charged headgroups and alkyl chains that promote higher membrane fluidity. In contrast to results with *E. coli* lipids, the MinE-membrane interaction is not rate limiting when lipids are used that promote the highest MinD-catalyzed ATP hydrolysis rates. Overall, our findings have general implications for Min protein oscillation cycles, including those that regulate cell division in bacterial pathogens that could potentially be targeted in for future development of new antimicrobial compounds.

Acknowledgments

Starting with my great graduate school supervisor, Dr. Natalie Goto, I would love to thank her for taking a chance and believing in me despite my poor scientific background when I joined her laboratory. I always like to use the phase “Natalie gambled when she accepted me in her lab”, hopefully, I proved that I was a winning gamble. I appreciate her patience providing me with help throughout my studies. Since English is not my first language and I didn’t do high school in an English-speaking country, learning new concepts in new language was difficult for me. Thus, I appreciate her for trying her best to prepare me for presentations and written documents which was difficult. She successfully made me a professional scientist and she will be always my hero.

I also would like to thank my thesis committee members Drs. Roberto Chica, Maxim Berezovski, François-Xavier Campbell-Valois, Tony Mittermaier and Bill Willmore for providing me with feedbacks and helping to guide this work to contribute significantly to the field. I would like to thank previous and current Goto lab members, Fatima Hafizi, Laura McLeod, Adam Cloutier, Kristopher Fequet and Anwar Hassan. I greatly thank Adam Damry for his endless help with NMR. Finally, I would love to thank Dr. Alexander Foo for his great help throughout my studies and for putting up with my silly jokes.

I also would like to credit Drs. Jeffery Keillor, Roberto Chica, John Pezacki, Tom Moon and Jan Mennigen for allowing me to use their instruments to conduct my research. I also would acknowledge NMR facility manager Dr. Glenn Facey for his generous help with troubleshooting NMR experiments. I greatly thank funding resources specially Dr. Yu for his generosity for the scholarships that covered my 2015 and 2016 academic years. Dr. Yu scholarships relieved my financial stress, I was able to focus more on my research and contribute to the scientific community with a recent publication.

I want to thank my family members, my lovely wife Anwar and my two angels Ridha and Joory along with my father, mother and siblings along. Lastly, I deeply thank all my friends and relatives who were beside me to encourage me all the time.

Table of Contents

List of Abbreviations

2D	2-dimensional
3D	3-dimensional
AEBSF	4-(2-aminoethyl) benzenesulfonyl fluoride hydrochloride
ADP	Adenosine Diphosphate
ATP	Adenosine Triphosphate
ATPγS	Adenosine 5′-O-(3-thio)Triphosphate
BCA	Bicinchroninic Acid
BSA	Bovine Serum Albumin
CD	Circular Dichroism
CT	C-terminus
DMSO	Dimethyl Sulfoxide
DOPG	1,2-dioleoyl-*sn*-glycero-3-phospho-(1'-*rac*-glycerol)
DOPC	1,2-dioleoyl-*sn*-glycero-3-phosphocholine
DSS	2,2-dimethyl-2-silapnetane-5-sulfonic acid
ec	*Escherichia coli*
E. coli	*Escherichia coli*
EDTA	Ethylenediaminetetraacetic Acid
ES	Enzyme-Substrate Complex
FPLC	Fast Protein Liquid Chromatography
FRET	Förster Resonance Energy Transfer
GFP	Green Fluorescent protein
hp	*Helicobactor pylori*
HSQC	Heteronuclear Single Quantum Coherence
IPTG	Isopropyl β-D-1-thiogalactopyranoside
k_{cat}	Rate Constant
kDa	Kilodalton
K_M	Michaelis Constant
LUV	Large Unilamellar Vesicle
MHz	Megahertz
MRE	Mean Residue Ellipticity
MS	Mass Spectrometry
MTS	Membrane Targeting Sequence
MWCO	Molecular Weight Cut-off
ng	*Neisseria gonorrhoeae*
N. gonorrhoeae	*Neisseria gonorrhoeae*
Ni-NTA	Nickel-Nitrilotriacetic Acid
NMR	Nuclear Magnetic Resonance
OD	Optical Density
PC	Phosphatidylcholine

PCR	Polymerase chain reaction
PDB	Protein Database (RCSB)
PE	Phosphatidylethanolamine
PG	Phosphatidylglycerol
PL	Phospholipids
POPG	1-palmitoyl-2-oleoyl-*sn*-glycero-3-phospho-(1'-*rac*-glycerol)
ppm	Parts Per Million
rpm	Revolution Per Minute
S.E.	Standard Error
S.D.	Standard Deviation
SDS-PAGE	Sodium Dodecyl Sulfate Polyacrylamide Gel Electrophoresis
shRNA	Short hairpin Ribonucleic Acid
SUV	Small Unilamellar Vesicle
TIRF	Total Internal Reflection Fluorescence
TSD	Topological Specificity Domain
Tm	Melting Point
VEGFA	Vascular Endothelial Growth Factor A Precursor
WT	Wild Type

List of Figures

List of Tables

List of Equations

Chapter 1

Introduction to the Min System

1.1: Min Proteins and Bacterial Cell Division

Bacterial cells reproduce by a process called binary fission, whereby the DNA is replicated and a cell division septum forms at the mid-cell location to produce two viable daughter cells. Formation of the division septum is initiated by a tubulin-like protein called FtsZ[1,2], which recruits other division proteins such as FtsA, FtsK and ZapA to form an annular polymeric structure called the Z-ring around the inner circumference of the cell[3]. The Z-ring acts as a scaffold for other proteins to form a protein complex called the divisome that drives cell division, constricting the cell membrane as new membranes for daughter cells are synthesized. Since placement of the divisome determines the location of cell division, it is critical for dividing bacterial to ensure that it is appropriately placed at the mid-cell location.

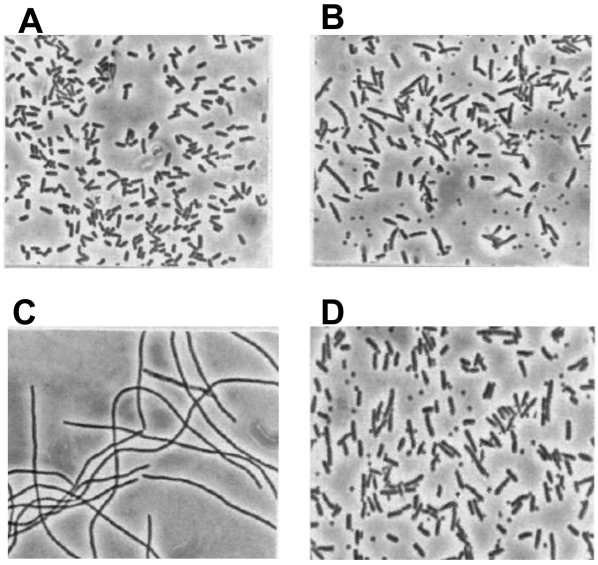

Figure 1.1. Phase contrast microscopy showing the role of the Min system in *E. coli* bacterial division. A) WT *E. coli* cells exhibit normal rod-shape morphology. B) An *E. coli minB* knockout shows minicells and filamentous morphologies. C) Overexpression of MinC and MinD in a *minB* knockout strain shows filamentous morphology. D) Overexpression of MinE in WT *E. coli* cells shows minicells. (Figure reproduced from De Boer *et al*,[4] with permission)

In gram-negative bacteria, the nucleoid occlusion system and the Min system ensure proper placement of the cell division septum[5,6,4]. The Min system is composed of three proteins encoded by the *minB* gene; MinC, MinD and MinE[7,8]. Deletion of the *minB* gene resulted in division septum formation at the cell poles, leading to minicells that lack

chromosomal material, and are unable to carry out subsequent rounds of cell division (Fig 1.1B)[4,9,10]. This suggests a critical role for the Min system in determining where cell division can occur in dividing bacteria by preventing division at polar sites and restricting division to the midcell position.

A number of microbiological studies have been conducted in order to identify the role of Min proteins in regulating bacterial cell division. For instance, phase-contrast microscopy studies showed that overexpression of individual Min proteins did not restore a normal phenotype in *minB* knockout *E. coli* cells that exhibit minicell morphology[4]. In the same study, overexpression of MinC and MinD, but not MinE with MinC or MinD, resulted in filamentous cells, a phenotype associated with inhibition of cell division (Fig 1.1C). Moreover, overexpression of either MinC or MinD in wild-type *E. coli* cells also resulted in filamentous cells[4,11]. Similar effects were also observed in the coccus *Neisseria gonorrhoeae*, where a knockout of MinC or MinD resulted in abnormal cell division, with daughter cells of different sizes, including mini-cells[12,13]. Taken together, these studies suggest that MinC works together with MinD to inhibit cell division.

The role of MinE in the Min system was revealed in a similar set of experiments that showed that expression of MinE at similar levels to MinD and MinC in a *minB* knockout *E. coli* strain resulted in wild-type cell division[4,14]. This indicates that MinE counters the inhibitory effects on cell division caused by MinC and MinD. This was supported by the filamentous phenotype observed in a MinE knockout in *E. coli* cells[15,16]. However, overexpression of MinE in wild-type *E. coli* cells resulted in formation of minicells (Fig 1.1D)[4,17,18], illustrating that high concentrations of MinE prevent MinC and MinD from inhibiting cell division at the cell poles, with all three proteins being required to produce viable, equally sized daughter cells that are able to undergo subsequent rounds of reproduction.

Due to its role in the regulation of bacterial cell division, the Min system has the potential to be used as a target for the development of a new class of antimicrobials, particularly since MinE does not have a homologue in humans. In addition, the production of minicells is being increasingly explored as a biotechnological tool, for example as a new vehicle for drug delivery[19]. Minicells derived from bacteria have

favorable size, safety, and biodegradability that offer intriguing advantages as a new drug delivery mechanism. This was illustrated in a recent study conducted with *E. coli* minicells produced from a PB114 strain (*minB* knockout) that had been transformed with an expression vector for short hairpin RNA (shRNA) against vascular endothelial growth factor A precursor (VEGFA). The surface of these minicells were conjugated with folic acid to target cancerous cells since cancer cells that express folate receptors. When these minicells were injected into a tumor xenograft made of A549, KB and LNCaP cells in an immune-compromised mouse model, tumor volume was reduced, showing that the anti-angiogenic effect of the shRNA was conferred to the tumors by this treatment[19,20].

Based on the potential of the Min system to be used as a target in antibiotic development, and to be harnessed as a biotechnological tool, there is high interest in understanding how the Min system works to regulate bacterial cell division, particularly since the molecular details of this are still not completely understood. Elucidation of these details is the primary goal of this thesis, with a focus on the interactions involving MinD and MinE.

1.2: Thesis Focus on the Min System in *N. gonorrhoeae*

While most knowledge about the Min protein system has been developed using *E. coli* proteins, we are interested in studying the Min system in *N. gonorrhoeae* since this pathogen causes gonorrhea, a sexually transmitted disease that is widespread in Africa and increasing in prevalence in Canada[2122,23]. Multi-drug resistant strains of *N. gonorrhoeae* have also become more prevalent[21], leading the government of Ontario to recommend combination antibiotic treatments in order to reduce its occurrence[24]. While this approach is effective for the short-term, development of antibiotic resistance by this strain remains a threat[25,26]. Thus, there is an urgent need to identify a new class of antimicrobial agent that can be used to treat and limit the spread of multi-drug resistance strains of *N. gonorrhoeae* in the future. For this reason, the Goto lab has focused on characterizing structure function-relationships in Min proteins from this pathogen.

A distinct feature of *N. gonorrhoeae* that differs from *E. coli* is that it is coccus-shaped, and therefore lacks obvious cell poles. Nonetheless, *N. gonorrhoeae* still

positions the cell division septum in a specific manner, by dividing along alternating perpendicular planes, resulting in the formation of a tetrad of daughter cells[27], a process that is also regulated by Min system. In spite of the different morphology of *E. coli* versus *N. gonorrhoeae* cells, Min system function is highly conserved across species, since expression of Min proteins from *N. gonorrhoeae* (*ng*Min) in place of *E. coli* Min proteins (*ec*Min) restores normal cell division[28]. In addition, overexpression of *ng*MinC in a *minC* knockout of *E. coli* cells results in a filamentous phenotype[12] similar to the phenotype resulting from the overexpression of *ec*MinC. Similarly, overexpression of *ng*MinD in *ec*MinD knockout *E. coli* cells also resulted in filamentous cells[29,30], and overexpression of *ng*MinE in *E. coli* cells gave rise to minicells [18]. Taken together, these data suggest that *N. gonorrhoeae* Min proteins can functionally complement *E. coli* proteins. This is not unexpected, given the high sequence similarities between *N. gonorrhoeae* (Ng) and *E. coli* (Ec) Min proteins (i.e. 42 % sequence identity for MinE, 75 % for MinD and 35 % for MinC), suggesting proteins from both species adopt similar structural folds. Therefore, the Min system is highly conserved and plays a role in the regulation of bacterial cell division across a wide range of gram-negative species.

1.3: Min Protein Interactions

A number of biochemical studies on Min proteins have been conducted in order to understand the molecular events that give rise to Min protein oscillation *in vivo*. These include size exclusion chromatography experiments showing that *ec*MinD is monomeric when bound to ADP, and forms a dimer upon nucleotide exchange with ATP[31]. Yeast two hybrid experiments also demonstrated that *ec*MinD is able to self-interact[29,32]. In addition, sedimentation experiments with lipid vesicles illustrated that *ec*MinD binds to lipid membranes, but only when in the dimeric-ATP bound state[31,33,34]. In the same study it was shown that *ec*MinC co-sediments with lipid-bound *ec*MinD[35], but cannot bind lipid vesicles itself, indicative of a direct interaction between MinD and MinC, as was confirmed by yeast two-hybrid experiments[31,36,37]. In addition, sedimentation assay results demonstrated that the C-terminus of *ec*MinC is able to co-sediment with *ec*MinD protein suggesting that this domain contains the MinD-binding site [35,38].

Biochemical studies have been performed in order to understand how the Min system interferes with formation of the Z ring. Sedimentation of *ec*FtsZ polymers *in vitro* showed that the amount of FtsZ that localizes to the pellet decreases as the *ec*MinC concentration increases, suggesting that MinC depolymerizes FtsZ[37]. Electron microscopy studies also illustrated that *ec*MinC is able to inhibit *ec*FtsZ polymerization [37]. The N-terminal domain of *ec*MinC was demonstrated to be sufficient to inhibit *ec*FtsZ sedimentation[38]. Dynamic light scattering experiments have also shown that *ec*MinC is able to actively disassemble the *ec*FtsZ polymer[39]. To understand how MinC interferes with FtsZ polymerization, *in vitro* FRET experiments with purified proteins showed that *ec*MinC interacts with monomeric *ec*FtsZ, suggesting that MinC interacts directly with monomeric FtsZ to prevent FtsZ polymerization required for Z ring formation[40]. Fluorescence anisotropy experiments confirmed this interaction, since there was an increase in anisotropy upon addition of *ec*MinC, consistent with the increase in the proportion of *ec*FtsZ that was monomeric[39]. In agreement with these studies, a recent sedimentation study also showed that *ec*MinC co-sediments with monomeric *ec*FtsZ[41]. Taken together, these data indicate that MinC inhibits FtsZ polymerization by sequestering monomeric FtsZ, thereby preventing FtsZ filament formation.

While these studies showed that MinC is a negative regulator of FtsZ, and MinD serves to target MinC to the membrane where it can inhibit FtsZ polymerization, the role of MinE in this system remained to be elucidated. This was addressed by vesicle sedimentation experiments which showed that *ec*MinE co-sediments with membrane-bound *ec*MinD. When done in the presence of *ec*MinC, the amount of co-sedimented *ec*MinC was reduced, suggesting that MinC was displaced by MinE[35]. Additionally, yeast three hybrid experiments showed that *ec*MinE is able to disrupt the *ec*MinD-MinC interaction, suggesting that MinC and MinE may bind overlapping sites of MinD. However, addition of *ec*MinC to the membrane-bound *ec*MinD/MinE complex did not affect the level of sedimented MinE with MinD and the amount of sedimented MinC did not increase[35], suggesting that MinE has a higher binding affinity for MinD.

In vitro vesicle sedimentation experiments suggested that *ec*MinE destabilizes the interaction between *ec*MinD and the membrane[35]. In addition, ATP hydrolysis by MinD from Ng and Ec have been shown to be stimulated by interactions with MinE, since *in*

vitro measurements of MinD ATPase activity showed 10 fold higher activity in the presence of MinE[42,43]. These assays of MinD ATPase activity show that it requires the presence of lipid vesicles, indicating that it is the membrane-bound version that is responsible for this activity[42].

Based on these *in vitro* results, a cycle of Min protein interactions was proposed as shown in Fig 1.2. In this cycle, MinD exists in an ADP-bound monomeric state. Upon nucleotide exchange with ATP, MinD forms a homodimer that localizes to the cell membrane. Membrane-bound MinD recruits MinC to the membrane to form a MinCD complex, referred as the inhibitory complex, which interferes with the formation of the Z ring. MinE binds to membrane-bound MinCD complex, displacing MinC, and stimulating ATP hydrolysis by MinD. The ADP-bound MinD dissociates from the membrane into a monomeric state where it is then free to diffuse to the other side of the cell where the cycle can start again.

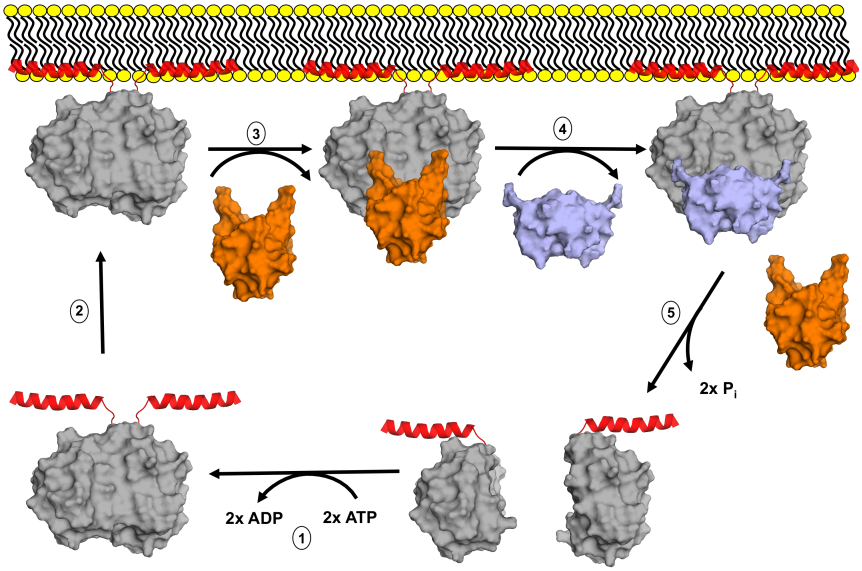

Figure 1.2. The Min protein interaction cycle. 1) Monomeric MinD (grey) undergoes nucleotide exchange with ATP to form a dimer that induces a conformational change that exposes the MTS (red), priming it for interactions with the membrane . 2) The MinD dimer localizes to membrane (yellow) where the MTS is inserted into the bilayer. 3) Membrane-bound MinD recruits MinC (orange) to form the MinCD inhibitory complex. 4) MinE (light blue) displaces MinC and stimulates ATP hydrolysis by MinD. 5) Stimulation of ATP hydrolysis leads to dissociation of MinD from the membrane to generate monomeric MinD where the cycle repeats itself.

1.4: The Min Oscillation Cycle

Mid-cell positioning of the division septum by the Min system was initially thought to be a static process[44,45]. However, *in vivo* studies with fluorescently labeled Min proteins[46,47] revealed that the localization of Min proteins is dynamic. As illustrated in Fig 1.3, fluorescence microscopy of live cells showed that MinD colocalizes with MinC at the inner membrane surface at one pole of the cell, forming a concentrated zone of MinC and MinD that grows from the pole towards the mid-cell. As the MinCD zone grows, a MinE-rich zone forms at the membrane on the growing edge of the MinCD zone, referred to as the E ring, which appears to stimulate the dissociation of MinCD from the membrane. The MinCD zone then shrinks back towards the cell pole and dissipates, followed by dissipation of the E-ring when it reaches the pole[48–50]. At this point a new zone of membrane-localized MinD and MinC becomes established at the opposite cell pole that grows and becomes capped by a new E ring as it reaches the mid-cell location. The cycle continues with the result that Min proteins oscillate in this coordinated fashion from pole to pole such that the time-averaged concentration of the MinCD complex is highest at the cell poles. This low time-averaged concentration of the MinCD complex at the mid-cell location creates a permissive zone that allows formation of the division septum at the mid-cell location required to produce two symmetrical daughter cells.

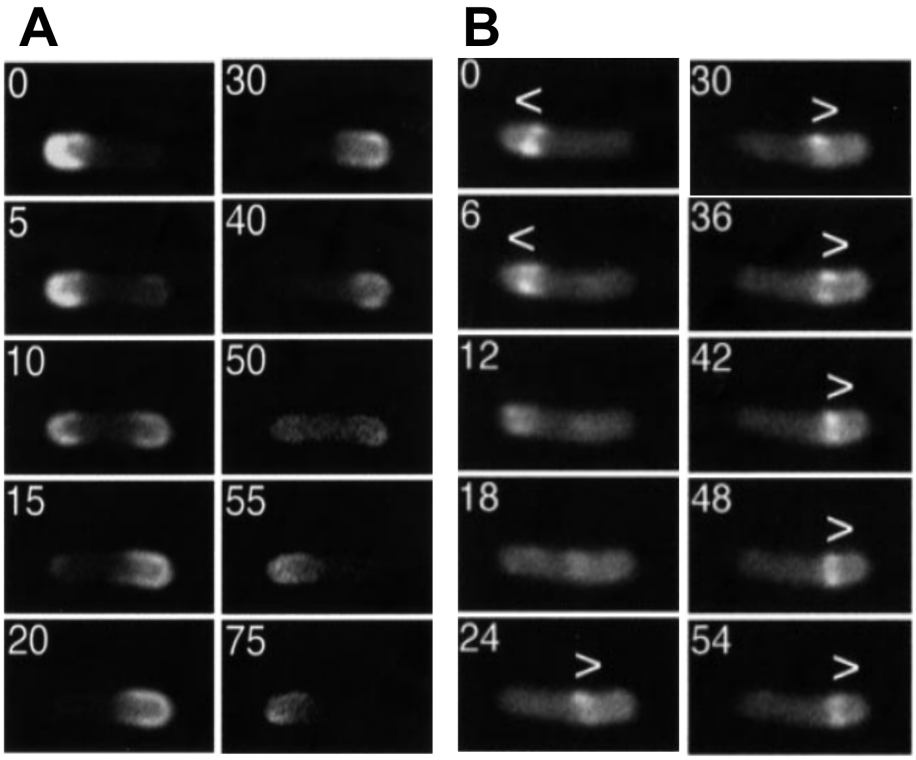

Figure 1.3. Fluorescence micrographs of the pole-to-pole oscillation cycle of GFP-labeled Min proteins in *E. coli.* A) Pole to pole oscillation of GFP-MinD expressed in *E. coli*. B) Oscillation cycle of GFP-MinE. The time in seconds that has elapsed from the first frame is indicated in the corner of each image. (Figures reproduced from Hale *et al*, [50] with permissions)

Min proteins are also capable of forming dynamic patterns when reconstituted on planar lipid surfaces *in vitro*[52–56]. Using total internal reflection fluorescence (TIRF) microscopy of fluorescent-labeled MinD and MinE on a planar lipid membrane, it was found that in the presence of ATP, MinD forms band-like zones on the membrane that move across the bilayer surface in propagating waves, where the trailing edge of each wave is capped with a MinE-rich zone (Fig 1.4A and B). Cross-sections of these waves show that MinD fluorescence on the membrane accumulates at a steady rate until it reaches a plateau at the mid-point of the wave, while the density of MinE at the trailing edge of the MinD wave continues to increase linearly beyond the MinD plateau until the ratio of MinE to MinD reaches approximately 1:1 (Fig 1.4C). At this MinE-MinD ratio, the fluorescence intensities of both MinD and MinE drop rapidly at the trailing edge of the wave. MinE dissociation was delayed, beginning after MinD dissociation had begun,

but dissociating with a faster rate than MinD. The delay between the start of MinE dissociation and MinD dissociation suggests that MinE lingers on the lipid bilayer surface after MinD has left the membrane.

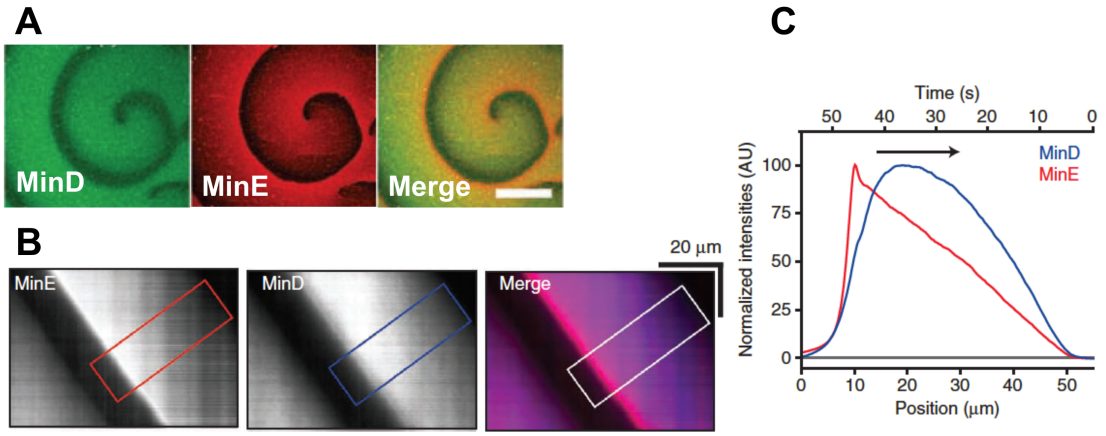

Figure 1.4. Min wave propagation on supported lipid bilayers *in vitro*. A) Fluorescent-labeled MinD (green) and MinE (red) form self-organized propagating waves on a supported lipid membranes. B) Kymographs of propagating waves obtained from TIRF micrographs showing MinD (blue), MinE (pink) and MinD/MinE overlapping (purple). C) Normalized profiles of MinD (blue) and MinE (red) fluorescence intensities obtained from kymographs. Note that the time profile for the intensity begins on the right hand side, and the increase in intensity over time is shown in the direction from right to left. (Figures reproduced from Loose *et al*,[53] and Loose *et al*,[55] with permissions).

These first studies of pattern formation by Min proteins were done by the Schwille group using a fixed total concentration of each protein in a chamber containing a renewable source of ATP. However, subsequent experiments by the Mizuuchi group using a flow apparatus showed a different type of pattern formation by Min proteins. In these experiments, a constant concentration of Min proteins was allowed to flow over a fixed planar membrane of defined lipid composition[56]. At early stages of the experiment, propagating Min waves similar to those that had been observed by the Schwille group were observed, but stalled over time, before developing into irregular shapes described as 'ameoba-like', with a MinD-rich core surrounded by a concentrated zone of MinE at its edge. However, the concentration of MinD and MinE on the membrane tended to increase over the duration of the experiment, leading to the suggestion that the accumulated protein caused membrane deformation, and that this might explain the change in Min patterns observed. To test this hypothesis, the Mizuuchi group conducted a

follow-up study[54], where the supply of Min proteins in the mobile aqueous phase was not continuously replenished. This led to a gradient of Min protein concentrations across the membrane surface, giving rise to Min patterns of various shapes and oscillation patterns at different locations of the flow cell (Fig 1.5). At the inlet location where the MinD:MinE ratio was highest, amoeba-like shapes were observed, in agreement with previous observations. Further from the inlet where the density of membrane-bound MinD dropped, these amoeba-like shapes were replaced by propagating waves. Propagating waves became regular spirals further away from the inlet point. At the other end of the flow cell where the outlet is located, and the MinD-MinE ratio is low, a pattern was observed where a central MinD zone undergoes expansion and then retraction while a MinE zone surrounds this MinD core until this core disappears. These experiments gave rise to the hypothesis that fluctuations in Min protein densities on the membrane are the driving force that give rise to the Min oscillation pattern observed *in vivo*, based on the depletion of Min protein from the cytoplasmic phase. However, these studies raised some interesting questions about the molecular details of pattern formation. In particular, why and how is MinE dissociation delayed after MinD dissociation, and how do membrane properties such as fluidity, charge and heterogeneity modulate Min pattern dynamics? These are fundamental questions, and have formed the basis for the work presented in this thesis.

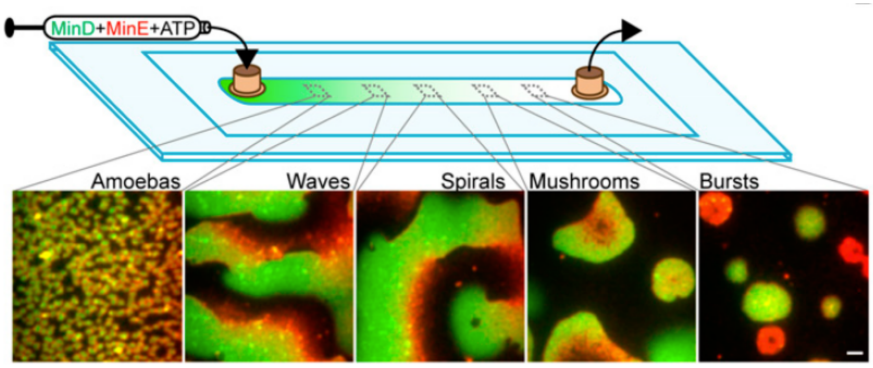

Figure 1.5. Min patterns induced by a concentration gradation of MinD and MinE across the membrane surface in a flow cell. Confocal images of fluorescent-labeled MinD (green) and MinE (red) passed through a flow cell coated with a supported lipid bilayer made from *E. coli* lipids. Different local Min densities on the membrane resulted in different Min pattern morphologies. (Reproduced from Vecchhiarelli *et al*,[54] with permission).

1.5: MinD-Membrane Interactions

These studies of Min protein localization performed *in vivo* and *in vitro* highlighted the importance of the MinD interaction with the membrane surface. In addition, *in vitro* studies of ATP hydrolysis by MinD showed that lipid membranes are required for the reaction to occur. The region of MinD responsible for the interaction with the membrane was shown to reside at the C-terminus, since deletion of ~10 residues from the C-terminus of *ec*MinD (Δ10CT) resulted in a mutant that failed to sediment with lipid vesicles in the presence of ATP. Deletion of these MinD residues also resulted in a cytoplasmic localization when this mutant was expressed in *E. coli*[36,57,58]. To determine if residues in this region were directly involved in membrane interactions, a unique tryptophan residue was introduced at various locations in this sequence, and tryptophan fluorescence spectroscopy performed to look for changes in the maximal fluorescence emission wavelength. These experiments revealed an increase in fluorescence intensity and a ~10 nm blue-shift in fluorescence in the presence of ATP and lipids[58], confirming that the C-terminus was exposed to a hydrophobic environment in the presence of lipids, suggesting that it directly interacts with the membrane. This was supported by circular dichroism (CD) spectroscopy experiments with a peptide comprised of the sequence from the MinD C-terminus which showed that it is largely unstructured, but adopts a helical configuration upon addition of small unilamellar vesicles[59]. Altogether, these results indicated that the C-terminal 10 residues of MinD are responsible for its membrane binding activity, leading to its designation as a membrane targeting sequence (MTS)[36].

The role of membrane properties such as fluidity and charge have been shown to affect MinD binding. For example, vesicle sedimentation studies showed that *ec*MinD has a 9-fold higher affinity for membranes containing anionic lipids compared to those comprised of neutral lipids[33]. MinD binding affinity was also significantly enhanced by PG/PC lipid mixtures that form microdomains of fluid-anionic lipid in gel-phase bilayers relative to a fully fluid PG/PC mixture. Moreover, there is also evidence that MinD alters membrane properties upon binding, as shown by experiments with membranes made from lipids doped with fluorescent probes that can monitor the degree of lipid acyl chain order. In membranes comprised of PG/PC lipids, MinD binding was found to increase the

disorder of PG lipids, but not PC lipids that were prepared above the phase transition temperature. This suggests that MinD induces lipid domain segregation to create microdomains that are enriched in negatively charged lipids. Large-scale changes in membrane morphology have also been observed upon MinD binding, as observed by electron microscopy. Specifically, at high *ec*MinD-lipid ratios, large unilamellar vesicles made from *E. coli* lipids were deformed into tubules[34,60]. However, since the concentration of MinD used in these studies was higher than *in vivo* concentrations, MinD-induced membrane deformation is not observed *in vivo*. Nonetheless, these results may reflect localized changes in lipid membrane properties at the cell pole where MinD concentrations are higher, potentially facilitating binding by additional MinD to promote growth of the MinD-rich zone.

The role of membrane properties such as fluidity and charge have also been investigated in Min pattern formation on planar lipid membranes[56]. In this study, a flow cell with different types of lipid mixtures fixed to the surface were exposed to a constant flow of a reaction solution containing various levels of fluorescent-labeled *ec*Min proteins. MinD and MinE propagating waves were observed on bilayers made from mono-unsaturated acyl chains with headgroups mimicking *E. coli* lipids, similar to the pattern observed on membranes made from *E. coli* lipids at room temperature[56]. However, an amoeba-like pattern was observed with a central core of MinD surrounded by a MinE zone when the experiment was replicated at a higher temperature that promoted a more fluid phase of the lipid bilayer. In addition, Min pattern morphology was found to depend on the amount of anionic PG lipid present in the lipid mixture. For instance, MinD and MinE proteins were shown to bind to a bilayer surface made from PC lipids, but exhibited no pattern formation, while a spiral pattern was observed when the membranes contained ~30% PG, similar to what had been observed with *E. coli* lipids. However, as the levels of PG were further increased, the wavelength of the MinD wave became narrower, and the velocity of wave propagation was reduced. Overall these results indicate that membrane fluidity and charge modulate MinD binding and Min pattern formation. However, given the different affinity that MinD exhibits for binding to lipid membranes of various fluidities and compositions, the different Min patterns may

simply reflect the difference in effective ratio of MinD to MinE as was previously observed[33,52,56].

In vivo experiments have also been carried out to understand the role of membrane properties in the Min oscillation cycle. Specifically, in an *E. coli* knock-out of PE lipid synthase, a filamentous cell morphology was observed, with a disrupted MinD oscillation pattern, as MinD moved as clusters on the membrane in a zigzag pattern[33]. Additionally, an *E. coli* strain with low levels of PG lipids showed MinD localized to the cell poles and midcell where anionic lipids such as cardiolipin are concentrated[57,61]. Although the differences in membrane composition relative to the WT strain are relatively large for these mutants, these results raise the possibility that local differences in membrane composition in the bacterial membrane may also play a role in the modulation of the Min oscillation cycle.

While a number of studies have been done on the effect of membrane properties on MinD binding and pattern formation, little is known about how membrane properties modulate MinD catalytic activity. Given the central role that ATP hydrolysis plays as the chemical driver of the Min protein cycle, I will explore in this thesis the role of membrane properties such as charge and fluidity in the modulation of MinD ATP hydrolysis *in vitro*.

1.6: Structure of MinD

MinD is a member of the Par-family of ATPases which is characterized by a deviant Walker A motif with sequence XKGGXXK(T/S) which is involved in binding ATP[38]. X-ray crystal structures of archaeal MinD show a central β sheet with 8 parallel β strands flanked by 11 peripheral α helices[62–64]. A common feature of the Par ATPase family is the P-loop, a conserved sequence between β1 and α1 that binds to ATP phosphate groups[65,66,67]. Specifically, in the MinD structure from *P. furiosus*, P-loop residues Gly13, Gly15 and Lys16 directly interact with the β and γ phosphate groups of ATP, while Thr17 and Thr18 hydrogen bond with the α phosphate group[68]. In addition, Par-family motifs called switch I (residues 40-46) and switch II (residues 117-123) loops are involved in sensing the presence of the γ phosphate group in the binding pocket and

undergo small conformational changes to get closer to the nucleotide which leads to stabilization of the MinD-ATP complex[68]. Additionally, residues Asp118 and Cys119 in switch II interact with water that is coordinated with the catalytically essential Mg^{2+} ion.

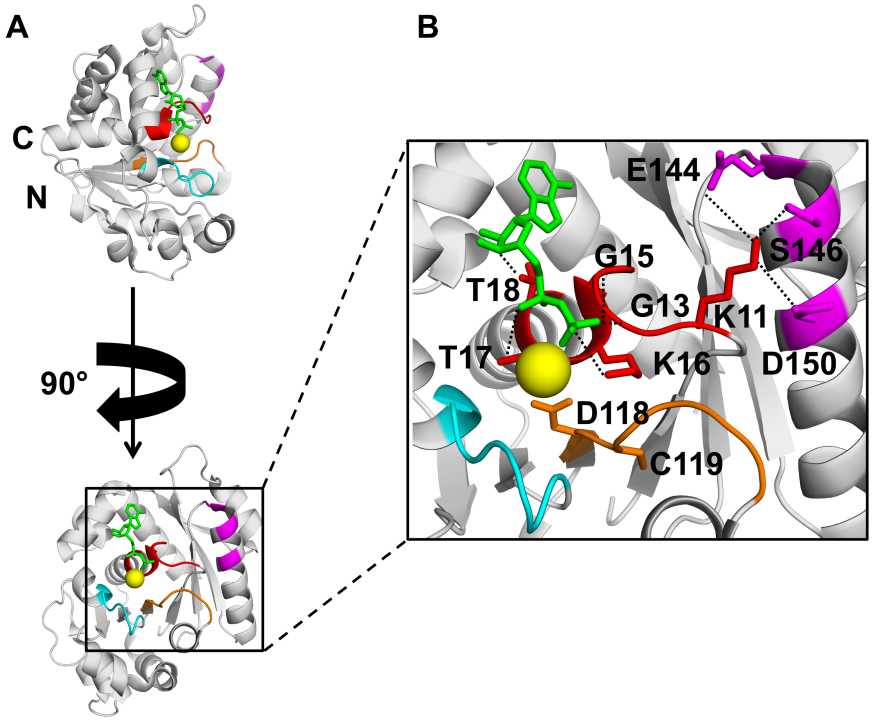

Figure 1.6. X-ray structure of ADP-bound MinD from *P. furiosus* (PDB ID: 1G3Q). A) Structure of MinD bound to ADP (green) and Mg^{2+} (yellow sphere), with the P-loop highlighted in red, switch I in cyan and switch II in orange. B) Expanded view of MinD-ADP interactions shows the signature Lys11 side-chain forms interactions with Glu144, Ser146 and Asp150 (purple).

A dimeric structure was more recently determined for MinD from *E. coli*, obtained using an ATP-hydrolysis-deficient mutant (D40A) that is still able to bind MinE and MinC (Fig 1.7). Since size-exclusion chromatography experiments showed that the MinD ΔCT10 is able to form a dimer in presence of ATP[36], the C-terminal MTS was also removed from this construct to improve sample solubility. This structure showed that one molecule of ATP is bound to each MinD subunit in a cleft buried within the MinD dimeric interface. Intermolecular interactions were observed between each subunit and the molecule of ATP that was bound to the other subunit, with these intermolecular interactions giving rise to localized conformational changes (Fig 1.7B). For example, in monomeric MinD, the signature lysine at position 11 that is located in the Walker A

motif makes hydrogen bonds with Ser148 and undergoes electrostatic interactions with Glu146 and Asp152. However, in the ATP-bound dimer, Lys11 no longer interacts with Asp152, but instead interacts with the β and γ phosphate groups of the ATP molecule that is bound to the other MinD subunit. The importance of this residue in MinD dimerization was confirmed in size-exclusion chromatography experiments of the MinD K11A mutant that showed an absence of dimerization in the presence of ATP[31].

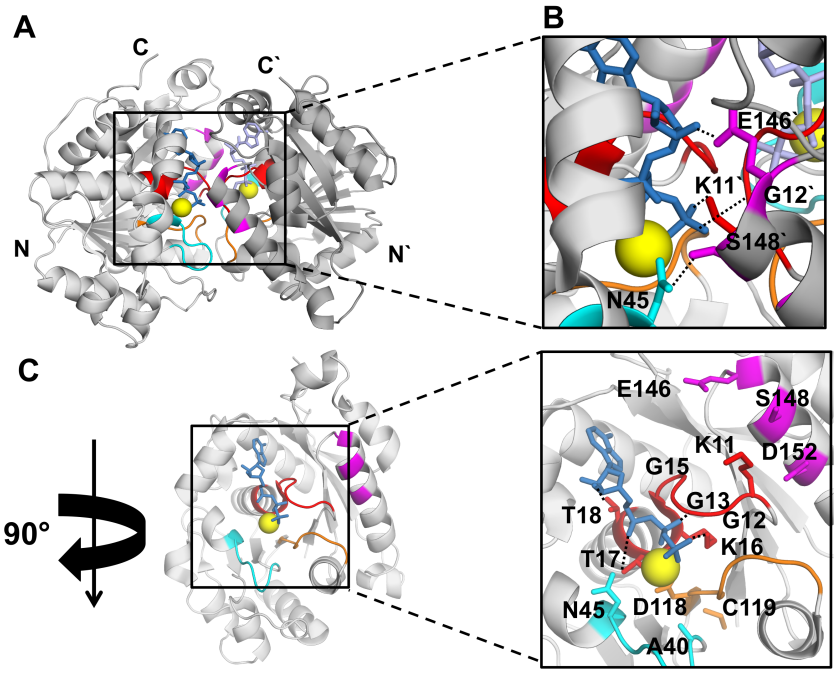

Figure 1.7. The dimeric structure of MinD Δ10CT (D40A) from *E. coli* (PDB ID 3Q9L). A) The MinD dimer structure (each subunit coloured light or dark grey) bound to ATP (dark and light blue). B) Expanded view highlights interactions that cross the dimeric interface and involving the ATP molecule (dark blue) bound to other MinD subunit. C) A 90° rotated view of one MinD subunit where the expanded view shows the MinD special motifs and interactions with ATP (dark blue) bound to the same the MinD subunit.

A number of other intermolecular interactions in ATP-bound MinD were also observed in the dimer structure, including one involving Gly12 that makes direct contact with the γ phosphate of ATP bound to the other subunit, while Glu146 interacts intermolecularly with the ribose ring of ATP. In addition, Asn45 in the switch I loop retains the same orientation in monomeric and dimeric MinD but also interacts with Ser148 in the other subunit[32,69](Fig 1.7C). Although Glu146 and Ser148 make

interactions across the MinD dimer interface, it has been found that these residues are not required for MinD dimerization, but are important for the stimulation of MinD-catalyzed ATP hydrolysis by MinE[70].

The crystal structure of the MinD dimer confirmed that the mechanism of ATP hydrolysis by MinD is likely to be similar to other members of the Par-family. Residue Asp40 is located close to the nucleotide binding site at the dimeric interface, at a location that is consistent with its role as a base catalyst that helps to activate water for nucleophilic attack. Mg^{2+} ions bind to a site close to the γ phosphate group of ATP to shield its negative charge and facilitate binding to the active site. Additionally, Mg^{2+} ions and residues Asp118 and Cys119 coordinate water molecules in a catalysis-suitable orientation such that residue Asp40 can interact and align the attacking water molecules, while residue Asn45 interacts with the γ phosphate group of ATP to stabilize the transition state[69].

Guided by the MinD dimer structure, it was possible to characterize MinE and MinC binding sites, which were proposed to be overlapping. When MinD residues identified to be important for MinE and MinC binding were mapped onto the MinD structure, they localized to a cleft formed by the dimeric interface of MinD (Fig 1.8). While some residues were only important for binding MinE (e.g. Leu48, Asp67, Val147, Leu194, Asp198, Ile202, L218, Ser221 and Asn222) or MinC (e.g. Arg44, Val57, Gln90, Thr91, Arg92, Arg151, Gly158, Ile159, Ala161 and Pro173), there was also a subset of residues that were found to be important for interactions with both proteins (e.g. Leu43, Asp47, Val56, Tyr58, Asp59, Val61, Lys94, Glu146, Val150, Asp154, Leu157, Ile 159 and Val188). Also, MinE-binding residues were not located close to the MinD catalytic site, suggesting that MinE is not directly involved in ATP hydrolysis, but rather causes conformational changes in residues that are more directly involved in ATP catalysis to stabilize the catalytic active state of MinD.

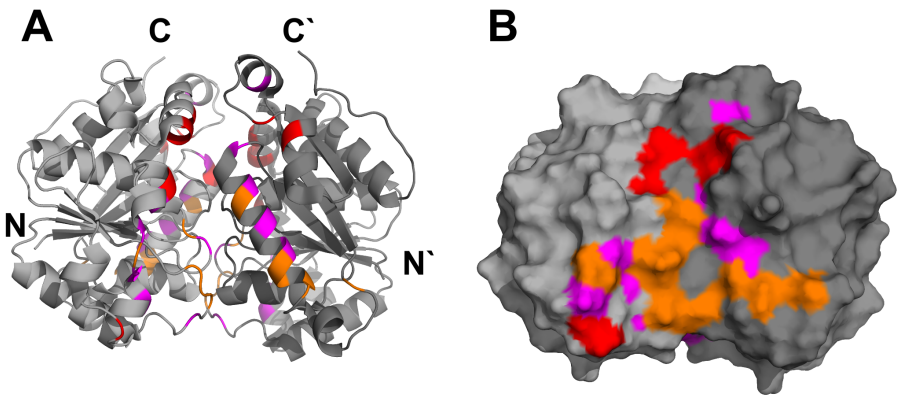

Figure 1.8. MinE and MinC binding sites on the *ec*MinD dimer structure. A) Cartoon representation of the *ec*MinD structure (grey) (PDB: 3Q9L) highlights regions important for binding MinE (red), MinC (orange) or both MinE and MinC (magenta), previously identified by yeast 2-hybrid experiments. B) Surface representation of the structure shown in (A) shows that the MinE/MinC binding regions are located at the MinD dimeric interface illustrating why MinD dimerization is required for binding.

1.7: Structural and Functional Characterization of MinE

A number of experiments have been done to identify the MinE residues involved in MinD binding and stimulation of ATP hydrolysis. One of the earliest of these showed that the filamentous morphology of a *minB* knockout *E. coli* strain transformed with a plasmid expressing *ec*MinC and *ec*MinD could be inhibited by expression of a *ec*MinE fragment containing just the first 22 residues (MinE(1-22))[9]. In contrast, if a C-terminal MinE fragment containing residues 30 to 88 was overexpressed in system in place of MinE(1-22), the cells remained filamentous. This suggested that the N-terminal region of MinE is sufficient to bind MinD and disrupt the MinCD complex. Consistent with this, yeast two-hybrid experiments showed that MinE missing the first 11 residues retained its ability to interact with MinD, while MinE missing the first 26 residues did not[18]. Subsequent yeast two hybrid experiments demonstrated that MinE residues 1-31 are sufficient for the MinD interaction. More importantly, this MinE fragment was able to disrupt MinD-MinC interactions in yeast three hybrid experiments, which led to assignment of this region as the anti-MinCD domain[71]. This system was used to show that anti-MinCD residues Ala18, Leu22 and Ile25 are crucial for disrupting the MinCD complex. In addition, mutations in Ala15, Lys19, Val26 or Arg30 showed reduced

capability for disruption of the MinCD complex. These residues are also important for Min protein oscillation *in vivo*, since mutation of any of these residues in MinE showed a loss of Min protein oscillation in *E. coli*[71].

The interaction between MinE and MinD was also investigated in *in vitro* MinD ATPase experiments with a range of MinE mutants[42,60,72]. These studies showed that *ec*MinE mutants K19Q, R21A, K19A/E20A and I17A/A18R failed to stimulate *ec*MinD ATP hydrolysis[42]. Additionally, overexpression of these mutants in a *minB* knockout that expresses MinC and MinD did not inhibit the filamentous phenotype, and did not promote pole-to-pole oscillation of MinD. Similarly, mutations in *ng*MinE anti-MinCD residues Ala18, Arg19, Arg20 and Leu22 disrupted its ability to stimulate *ng*MinD-catalyzed ATP hydrolysis, confirming the importance of these residues in the MinD interaction and stimulation of its ATPase activity [43].

Interestingly, when pure MinE was subjected to limited proteolysis by trypsin, a 7 kDa fragment corresponding to residues 31-88 was found to be resistant, whereas the anti-MinCD region was completely digested[73]. This suggested that the antiMinCD domain could be unstructured since protease cleavage occurs more rapidly at unstructured sites that are well-exposed to solvent. To verify this hypothesis, solution NMR experiments were done with a peptide containing the first 22 residues from *ec*MinE[73]. Chemical shifts and NOE patterns were found to be consistent with a largely unstructured region and some sampling of nascent helix conformations. This suggested that the anti-MinCD domain is largely unstructured, but could adopt an α-helix conformation upon interaction with MinD.

Experimental efforts to dissect the functional role of the C domain of MinE (31-88) included the overexpression of MinE residues 22-88 or 36-88 in wild-type *E. coli*, which produced a minicell morphology, reflecting the loss of proper positioning of the cell division septum[9,45,73,74]. These experiments indicated that the biological function of this C-terminal domain is to maintain proper placement of cell septum, in other words, to confer topological specificity to the action of the anti-MinCD domain. This led to the assignment of the C-terminal domain of MinE, containing residues 32 – 88, as the topological specificity domain (TSD).

The solubility and stability of the TSD allowed its structure to be solved using solution NMR[14]. As shown in Fig 1.9A, the TSD forms a homodimer comprised of a 4-stranded β sheet with an α-helix from each subunit packed against the core β sheet while also forming coiled coil interactions with the corresponding helix in the other subunit to form part of the dimeric interface. Interactions between these α-helices involve an extensive network of van der Waals interactions. The dimeric interface is also stabilized by hydrogen bonds formed between conserved polar residues located on α-helix that is packed against the core β sheet[75]. In addition, residues 31-35 formed a helix that, when coupled with the NMR data on residues 1 to 22 from the anti-MinCD domain, suggests a helical conformation for the full anti-MinCD domain[14]. Taken together, this led to a model for the full-length MinE structure where the anti-MinCD domain forms a helical structure that projects away from the TSD structure, primed for interactions with MinD.

Residues Asp45 and Val49 were previously identified to be important for topological specificity function, since mutations in these residues abrogated the ability of the TSD to interfere with cell division septum placement in wild-type *E. coli*. In addition, when these mutants were introduced into full-length MinE and expressed in place of the WT protein in *E. coli*, Min protein oscillation rates decreased and showed reduced E-ring formation, giving rise to a filaments and minicells. In the TSD dimer structure, these residues were found to map to a contiguous surface close to the dimeric interface formed by the coiled-coil. Size-exclusion chromatography showed that these *ec*TSD mutants formed stable dimers, while solution NMR experiments also showed minimum chemical shift perturbations[14]. Therefore, while these residues appear to play a role in the topological specificity function of MinE, they do not appear to act by altering MinE structure.

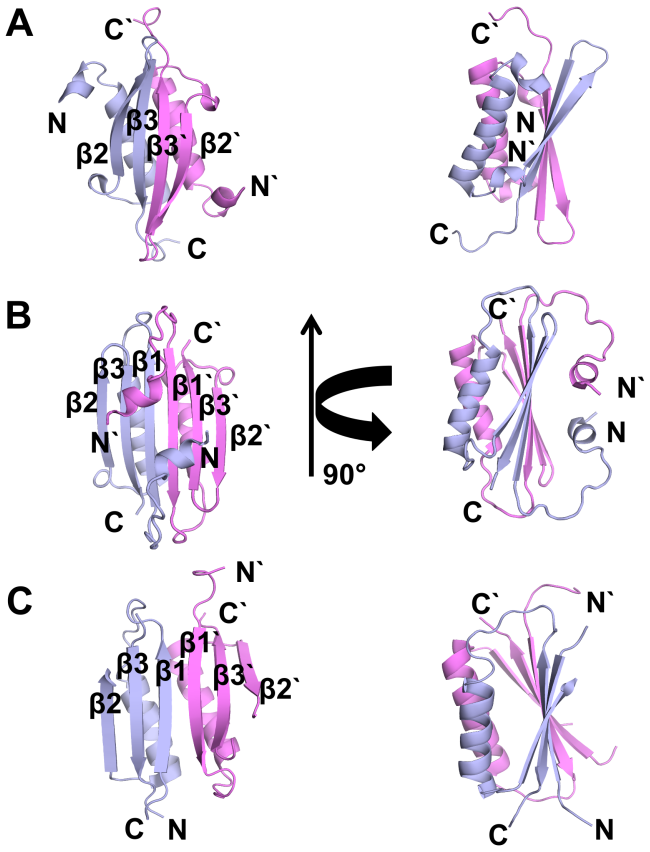

Figure 1.9. Comparison of MinE structures. A) *ec*TSD solution NMR structure (PDB ID: 1EV0) shows a 4-stranded β sheet. B) Full length *ng*MinE solution NMR structure (PDB ID: 2KXO) shows a 6-stranded β sheet. C) X-ray structure of residues 13-76 from *H. pylori* MinE (PDB ID: 3KU7) also shows a 6-stranded β sheet. Each subunit in the MinE dimer is colored differently.

Subsequent structure determination of a full length MinE protein from *Niesseria gonorrhoeae* with a solubility-enhancing mutation (E46A) showed surprising differences from this model based on the TSD structure[43]. As shown in Fig 1.9B, the structure of *ng*MinE is a homodimer comprised of a 6-stranded β sheet with an α helix from each subunit packed against the β-sheet, as was observed with the *E. coli* TSD structure. However, unlike the TSD structure, residues 21-30 from the anti-MinCD domain are located in a central β1 strand at the dimeric interface, with extensive van der Waals interactions between side chains and backbone hydrogen bonding between β-strands across the dimer interface. This fold was consistent with a crystal structure determined at approximately the same time for MinE from *Helicobactor pylori* (Fig. 1.9C), which also showed a 6-stranded sheet [75]. Unique to the *ng*MinE structure, however, was the presence

of an amphipathic α helix formed by residues 3 to 9 that packs against the β-sheet, making van der Waals interactions with residues from the other subunit in the dimer. Although a homologous sequence is present in *hp*MinE, electron density could not be resolved for these N-terminal residues in its crystal structure.

Surprisingly, some residues that had been previously identified to be important for MinD interactions[43,71] were not part of the solvent-accessible surface in this *ng*MinE structure. Specifically, residue Leu22 is buried in the hydrophobic core at the dimeric interface, and Ile25 is buried by interactions with the N-terminal amphipathic helix. However, this structure called into question the importance of Leu22 in the MinD interaction since its mutation to a polar residue would be expected to disrupt the hydrophobic core, potentially reducing the activity of any mutants of this residue through indirect effects. In support of this, structural studies with L22D *ng*MinE using CD and NMR revealed a significant structural perturbation induced by this mutation. In order to determine whether Leu22 was involved in direct interactions with MinD, *ng*MinE-stimulated *ng*MinD-catalyzed ATP hydrolysis was tested using the MinE peptide containing residues 1 – 22, with the mutation L22A. ATP hydrolysis rates were measured over a range of peptide concentrations and used as a measure of MinD binding by assuming that the rate of MinD ATP hydrolysis stimulated by MinE is proportional to amount of MinE bound to MinD. When fit to the Hill equation for binding, the amount of MinE required to reach half maximal stimulation of MinD ATPase activity was found to be significantly higher for the L22A MinE(1-22) compare to the WT peptide. In contrast, the R21A mutant of MinE(1-22) did not stimulate MinD ATP hydrolysis, even at elevated concentrations. Similarly, a shorter peptide comprised of only the first 17 residues of MinE was found to be completely inactive in this assay. These results suggest that Leu22 is directly involved in the MinD interaction, and that Arg21 is critical for stimulation of ATP hydrolysis[43]. In addition, similar studies with a MinE peptide containing residues 1-27 showed weaker apparent MinD binding affinity for the I25R mutant compared to the wild-type peptide[43]. Taken together, these results suggest that MinE residues 18 to 25 region are required for maximal stimulation of MinD ATP hydrolysis. However, given the buried location of many of these residues in the full-length MinE structure, these results raised questions regarding the mechanism by which

MinD can gain access to these residues. In this thesis, I explore the potential mechanism by which MinD gains access to these residues in order to stimulate its ATP hydrolysis.

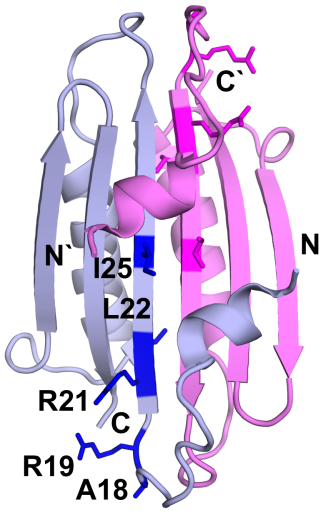

Figure 1.10. Location of MinD-binding residues mapped onto the *ng*MinE structure (PDB ID 2KXO). Some MinE residues (dark blue and magenta) involved in stimulation of MinD ATP hydrolysis are located on the central β1 sheet.

1.8: MinD Accesses Buried MinE Residues

Although a simple mechanism to increase the solvent exposure of anti-MinCD residues Arg21, Leu22 and Ile25 would be through dissociation of the *ng*MinE dimer, analytical ultracentrifugation showed only a dimeric form could be detected at the lowest possible concentration that could be assayed (~3 μM)[43]. Backbone amide solvent exchange NMR experiments also showed that the central region of the dimeric interface is the most protected region from exchange, suggesting the hydrogen bonding interactions across the dimeric interface are the most stable in this structure. These results suggested that MinE remains dimeric, and hence there must be another mechanism by which MinD can gain access to buried residues in the anti-MinCD domain of MinE (Fig 1.11), namely a significant conformational change.

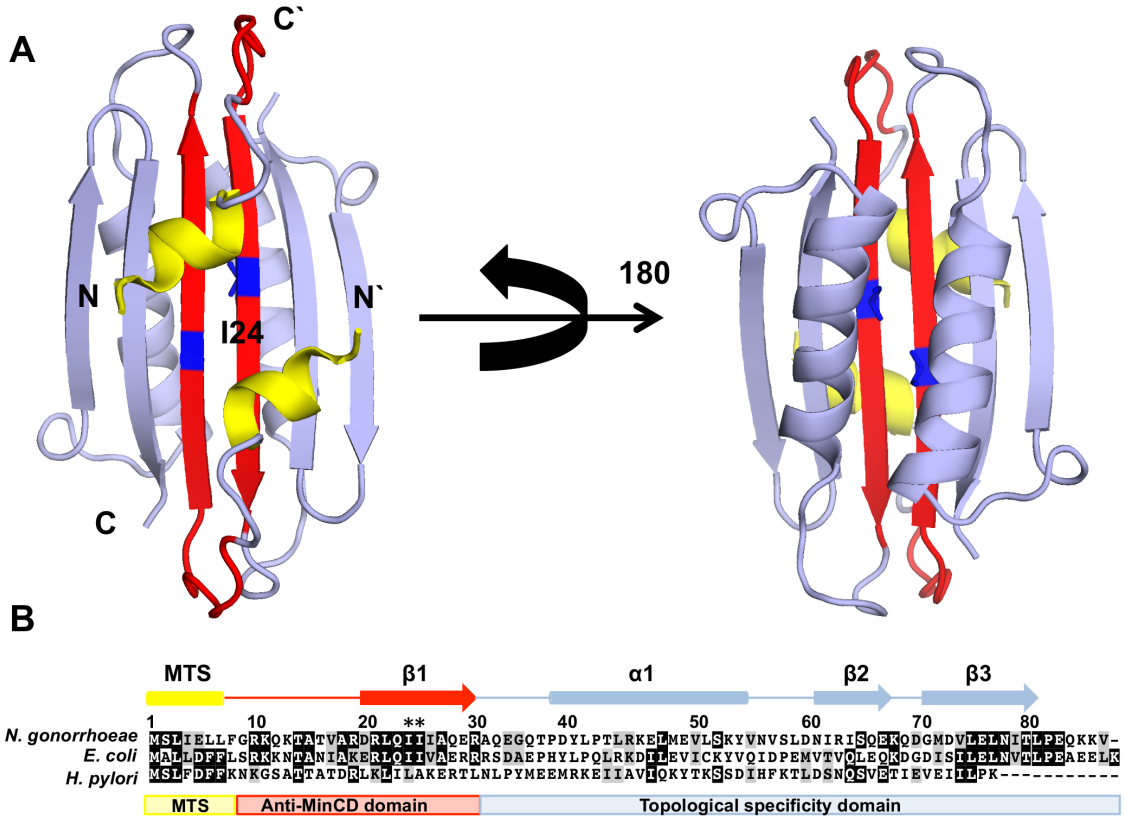

Figure 1.11. Functional and structural domains of MinE mapped onto the *ng*MinE structure (PDB ID 2KXO). A) Structural features of MinE; membrane targeting sequence (MTS) shown in yellow, the anti-MinCD domain involved in stimulation of MinD catalyzed ATP hydrolysis in red, and the topological specificity domain in light blue. Residue Ile24 buried in the hydrophobic core is highlighted in dark blue. B) Alignment of MinE sequences from the three homologues for which high resolution structural data is available performed in ClustalW[76], shown with a schematic diagram of secondary structure elements for *ng*MinE (top) and functional domains (bottom). Residues 24 and 25 are indicated with an asterisk above the sequence. Identical residues are highlighted in black, homologous residues in grey.

Important insight into the conformational change of MinE was obtained by elucidation of the x-ray crystal structure of MinD bound to MinE. In order to trap the MinDE complex structure, it was necessary to use the catalytically inactive *ec*MinD mutant D40A, and remove the C-terminal MTS from MinD[77]. In addition, the N-terminal 11 residues were also removed from *ec*MinE, and the Ile24 residue that is buried at the dimeric interface of MinE on the central β1 strand (Fig 1.11) was mutated to the polar

residue Asn. This mutation was designed to disrupt the hydrophobic core and destabilize the 6-stranded state obtained in the absence of MinD. Interestingly, in this complex structure, MinE residues 35 – 88 adopted a structure that was highly similar to that of the *ec*TSD, with a 4-stranded β sheet and residues from β3 in the full-length structure form part of the new dimeric interface. In this complex, the anti-MinCD domain is no longer buried inside the protein core, but is instead extended away from the main core of the MinE structure to form a helical structure that interacts with MinD.

The helical structure of the anti-MinCD domain seen in the complex structure is consistent with previous structural studies on the MinE peptide containing residues 1 – 22 that showed a nascent helical conformation[73]. In agreement with previous biochemical studies, the MinE binding site is located at MinD dimer interface as shown in Fig 1.12A. Moreover, the MinD residue Ser148 from one subunit is closer to Lys11 of the other subunit relative to its position in the MinD dimer structure (Fig 1.12C). In addition, the orientation of MinD residue Glu146 is also different in the MinDE structure, no longer participating in polar interactions with ATP bound to the other subunit. Based on the extensive interactions made between the MinE residue Arg21 and MinD residues Glu53, Leu48, Ser221 and Asn222, it was proposed that this played a key role in the activation of the MinD ATPase. Support for this hypothesis was provided by the observation that these interactions appear to liberate the MinD residue Asn45 from its interaction with Ser148, allowing it to interact with the γ phosphate group of ATP to play a role in stabilizing the transition state. Consistent with this hypothesis, the MinD N45A mutant is able to bind to ATP, dimerize, and recruit MinC, however its ATPase activity is not stimulated by MinE[69]. This suggests that Asn45 is a MinD catalytic residue that is activated upon MinE binding to MinD.

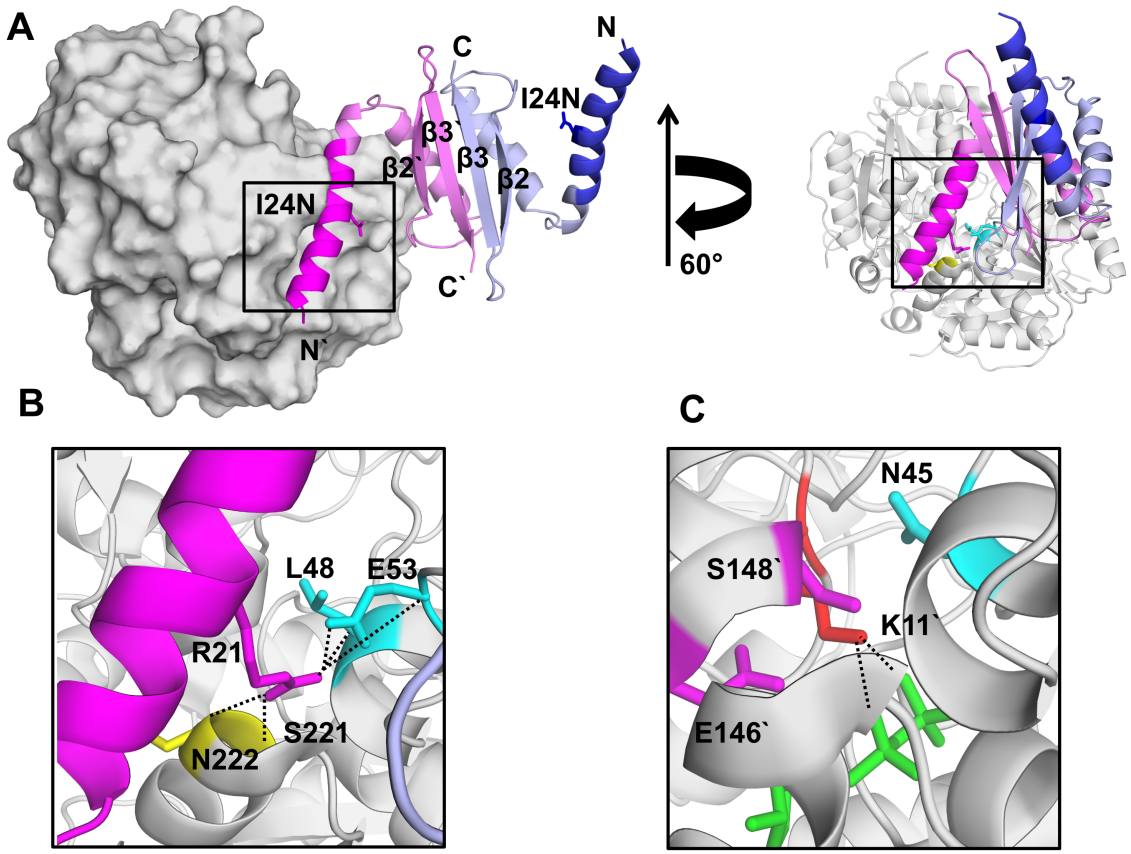

Figure 1.12. X-ray structure of *ec*MinD in complex with *ec*MinE (PDB ID 3R9J)**.** A) ATP-bound *ec*MinD Δ10CT (D40A) in complex with 12-88 *ec*MinE (I24N) mutant (each subunit either colored purple or blue where anti-MinCD domain residues 13 to 30 are highlighted with darker colors. β-strand numbering is as shown in Figure 1.9. B) Expanded view shows MinE Arg21 interactions with MinD residues Leu48, Glu53, Ser221 and Asn222. C) Expanded view of the MinD region that shows differences in conformation from the MinD structure determined in the absence of MinE.

Although introduction of a polar residue in the hydrophobic core is usually unfavorable structurally, it was shown that full-length *ec*MinE I24N was able to retain its interactions with *ec*MinD in a bacterial two-hybrid system[69]. Additionally, I24N MinE was able to restore cell viability in an *E. coli minB* knockout transformed with a plasmid that overexpresses both MinC and MinD at levels that usually prevent cell growth on solid media. These results suggested that the MinE 4-stranded β structure that was trapped in the MinE-MinD complex represents a functional conformation of MinE. However, this raises questions as to how MinE is able to achieve this conformational change in the absence of this I24N mutation *in vivo*. One possible scenario is that direct

interactions between MinE and the membrane might facilitate this conformational change.

1.9: MinE-Membrane Interaction

Although the earliest models of the Min protein interaction cycle suggested that MinE interacts with membrane-bound MinD, evidence has emerged that suggests that MinE is also capable of interacting with the lipid membrane independent of MinD. For example, electron microscopy experiments showed that at high protein:lipid ratios, *ec*MinE can cause deformation of lipid vesicles[78]. Interestingly, a peptide containing just the anti-MinCD domain was also able to induce the same type of deformation into tubule structures. Consistent with this observation, lipid sedimentation experiments showed that this peptide binds to lipid vesicles with a higher affinity than the full-length protein. These studies also demonstrated that the MinE-membrane interaction is largely mediated by electrostatic interactions, since the amount of protein found in the lipid pellets decreased with increasing salt concentration. In addition, an increase in pelleted MinE was also observed with lipid mixture containing anionic headgroups, suggesting that basic residues in MinE may be important for this interaction.

Localization experiments were carried out to understand the role of MinE-membrane interactions *in vivo* with three *ec*MinE mutants where clusters of basic amino acids in the anti-MinCD domain were changed to negatively charged amino acids to create three mutants, called C1 (R10D/K11E/K12E), C2 (K19E/R21D) and C3 (R29D/R30R/R31D). When overexpressed in a Min knockout strain of *E. coli*, C2 and C3 were localized to the membrane while C1 was not, indicating that residues in cluster C1 are important for the MinE-membrane interaction. However, tryptophan fluorescence measurements done on an anti-MinCD peptide containing Trp in place of Ala2, Ala3 or Phe6 showed significant blue shifts in the presence of liposomes, suggesting that the N-terminal helix was directly involved in membrane binding[79]. Mutations introducing polar amino acids into these sites (A2E/L3S/F6D) expressed along with WT MinD in a Min knockout stain of *E. coli* showed mutant MinE distributed throughout the cell cytoplasm, while MinD was uniformly distributed on the membrane. In addition, if single

substitutions were made to any of these amino acids to a negatively charged amino acid (i.e. L3E, L4E, F6E and F7E) in the 4-stranded mutant I24N, then expression of any of these proteins in *Δmin E. coli* caused cytoplasmic localization, in contrast with I24N in the absence of these mutations. Taken together, these observations led to the assignment of the N-terminal amiphipathic helix in MinE as the membrane targeting sequence (MTS)[77].

Indirect evidence that MinE makes direct interactions with the membrane during the Min protein interaction cycle has been provided by fluorescence microscopy studies of Min proteins on planar lipid membranes which show that MinE dissociation is delayed after MinD dissociation. When done under conditions of the flow experiment it was also observed that a *ec*MinE mutant lacking the MTS (ΔMTS)[54] gave rise to faster Min protein wave propagation, and narrower wavelengths compared to full length MinE. Unlike full length MinE, ΔMTS MinE release from the lipid bilayer was found to occur simultaneously with MinD release. These results suggest that the MinE-membrane interaction gives rise to a lag period between successive propagating waves and therefore regulates wave velocity to modulate the overall Min dynamic patterns. However, it still remains unclear how the MinE-membrane interaction is involved in modulation of the Min protein oscillation cycle. Since Min oscillation is linked to MinD ATP hydrolysis, in this thesis I have investigated the role of MinE-membrane interaction in modulation of MinD ATP hydrolysis.

In addition, a previous study of ^{15}N spin relaxation by solution NMR provided evidence for conformational exchange where a small population of the MTS amphipathic helix dissociates from the β-sheet[43], a model that has been recently supported by hydrogen–deuterium exchange MS experiments[80]. It was demonstrated that motions on ms-μs time scale in residues on MTS and on central β1 sheet were detected suggesting that motions could be due to discociation of MTS from structure core of MinE (Fig 1.13A). This would be expected to facilitate the interaction of the MTS with the membrane by exposing the hydrophobic face that is normally buried by interactions with the β-sheet in the closed structure. In addition, side chains from residues that are required to bind to MinD, including Arg-21 and Ile-25, are also obscured by the MTS in the closed structure, suggesting that the first step in the conformational transition to the open state

would involve dissociation of the MTS from the main body of the structure (1.13B). Thus, I think thesis, I investigated the role of MinE conformational equilibrium involving the MTS on modulation of MinD catalyzed ATP hydrolysis.

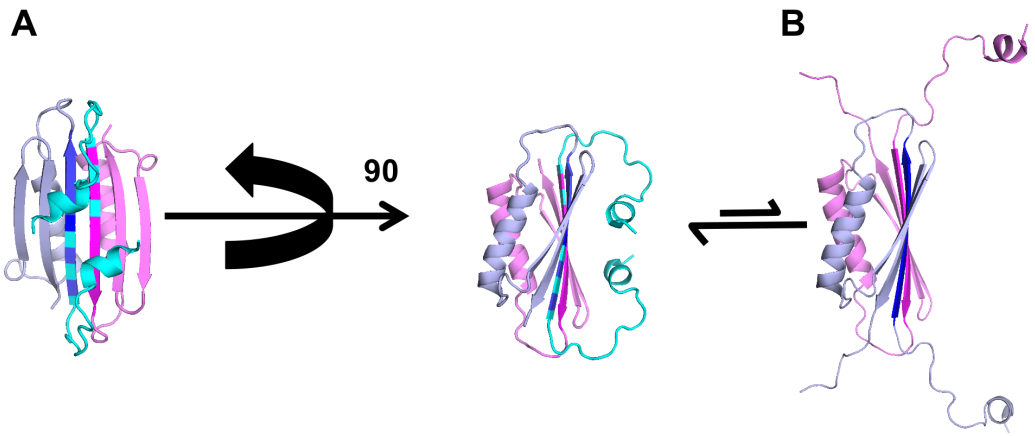

Figure 1.13. MinE residues that showed motions mapped onto *ng*MinE structure (PDB 2KXO). A) MinE residues undergo ms-μs time scale dynamics observed by releaxation experiments (cyan) are located on MTS, N-loop and MTS-interacting residues on central β1 sheet (darker colors). B) Hypothetical model of "semi-open" MinE structure shown MTS is dissociated from the structure core.

1.10: Thesis Objectives

Since MinE-stimulated ATP hydrolysis by MinD is linked to the Min protein oscillation cycle, a primary focus of the Goto lab has been on the characterization of the structure and function of MinE. Previously in the Goto lab, the structure of MinE from *N. gonorrhoeae* was determined to be a 6-stranded β sheet dimer where MinE residues involved in stimulation of MinD ATP hydrolysis were mapped to the central β1 strands, buried within the dimeric interface. This raised the questions regarding how MinD might gain access to these residues. The crystal structure of MinE-MinD complex that was subsequently released, revealed these same MinD-binding residues in an α helix in direct interaction with MinD. However, as a number of modifications to the MinE sequence were required in order to trap it in this state, it is still not known how this conformational transition is stimulated *in vivo*. In Chapter 3, I investigate the role of MinE-membrane interactions in this conformational change, and the modulation of ATP hydrolysis by

MinD. I also probe the role of this MinE conformational change in regulating MinD ATP hydrolysis *in vitro* using a MinE mutant that trapped in the 4-stranded β structure similar to that observed in the MinE-MinD complex. Due to the importance of the MinE conformational change in modulating MinD ATP hydrolysis, I investigated the ability of MinD to induce this conformational change in MinE using solution NMR in Chapter 4. Results from these chapters will help to understand how MinE exposes MinD-binding residues for MinD interaction and stimulation of MinD ATP hydrolysis.

In Chapter 5, I investigate the role of membrane properties such as fluidity and charge on ATP hydrolysis by MinD. While it has been shown that membrane binding and Min oscillation patterns are affected by lipid membrane properties, it is still unclear whether membrane properties such as fluidity, charge and curvature modulate MinD ATP hydrolysis *in vitro*. Results from this chapter will provide insights on the role of lipid bilayer characteristics in modulating the rate MinD-catalyzed ATP hydrolysis, and the ability of MinE to stimulate this activity.

The overall results from this thesis are anticipated to help elucidate how MinD ATP hydrolysis is modulated *in vitro*. Taken together, these findings will give rise to an updated version of Min protein cycle, and enhanced understanding of Min protein function in general.

The principle methods used to probe Min protein structure and function in this thesis include enzyme kinetics, circular dichroism (CD) spectroscopy and solution NMR, using purified MinD and MinE. These tools will be used to examine the following aspects of MinD-catalyzed ATP hydrolysis:

- The MinE-membrane interaction
- The MinE conformational change
- The role of MinE residue Ile25 in the interaction with MinD
- MinD-induced MinE conformational change
- The effects of membrane properties such as fluidly, charge and curvature

The following sections of this chapter will be devoted to the introduction of the basic theory behind these methods, and how they will be applied to MinD and MinE.

1.11: MinD Enzyme Kinetics

Since ATP hydrolysis by MinD requires interactions with MinE, measurement of ATP hydrolysis rates can be used to probe MinD-MinE interactions. Enzyme kinetic measurements are typically done using the Michaelis-Menten model, which requires that the concentration of substrate be present in great excess of the enzyme and rates be measured in the early stages of the reaction (e.g. less than 30% of the substrate consumed)[81]. Based on this model, substrate binding to enzyme forms an enzyme-substrate complex (ES) that can be approximated to be in equilibrium with free enzyme with a dissociation constant that is also referred to as the Michaelis constant (K_M)[82]. In this model, the rate of reaction of the ES complex to form free enzyme and product is a first order reaction with the rate constant k_{cat}, as seen in the scheme:

$$E + S \underset{k_{-1}}{\overset{k_1}{\rightleftharpoons}} ES \xrightarrow{k_{cat}} E + P \qquad \text{(Eq. 1.1)}$$

In this model, the initial rate of reaction (v_o) is described by the equation:

$$v_o = \frac{k_{cat}[E][S]}{K_M + [S]} \qquad \text{(Eq. 1.2)}$$

where [E] and [S] are concentrations for enzyme and substrate, respectively. This equation will give rise to a hyperbolic curve when initial rates are graphed as a function of substrate concentrations, where the plateau represents the maximal rate when the enzyme is saturated with substrate (V_{max}) and the substrate concentration required to reach half maximal rate represents K_M[83].

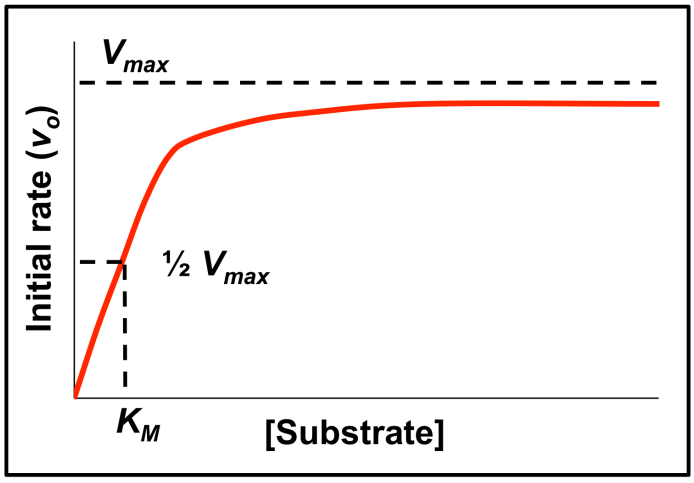

Figure 1.14. Schematic illustration of the Michalis-Menten plot and constants.

In this thesis, the amount of free inorganic phosphate that is generated by ATP hydrolysis was monitored over time to determine initial reaction rates, which were measured over a range of MinE concentrations[43]. Assuming that MinD activity reflects the amount of MinE that it bound, then it is possible to use this activity measurement to monitor the interaction using the hill equation[43,84]:

$$\frac{v_o}{v_{max}} = \frac{[\text{MinE}]^h}{(\text{K}_{0.5})^h + [\text{MinE}]^h} \qquad \text{(Eq. 1.3)}$$

where $K_{0.5}$ is the concentration of MinE that is required to achieve the half maximal MinD ATP hydrolysis rate, h is the Hill coefficient that reports the degree of cooperativity of MinE binding to MinD and [MinE] is the concentration of MinE (Fig. 1.15). Since MinD ATP hydrolysis is proportional to MinE binding, at maximal MinD ATPase activity, all sites are assumed to be occupied by MinE and therefore $\frac{v_o}{v_{max}}$ represents the fraction of MinE-binding sites in MinD protein that are occupied by MinE. In this thesis MinE-stimulated MinD-catalyzed ATP hydrolysis will be used as a tool to probe the role of the MinE-membrane interaction, MinE conformational changes and membrane properties in the modulation of MinD ATP hydrolysis *in vitro*.

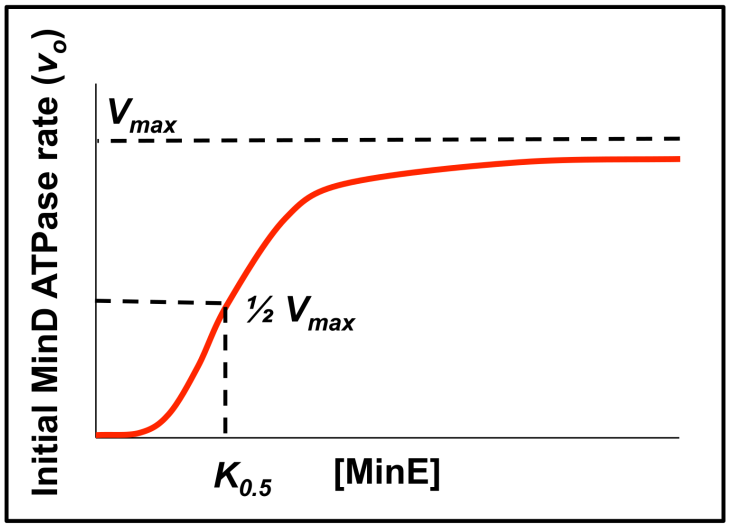

Figure 1.15. Schematic illustration of the Hill plot. Initial MinD ATPase rates can be fit to the Hill equation as a function of MinE concentrations to allow the MinE-MinD apparent binding affinity $K_{0.5}$ and MinD maximal ATPase activity to be determined.

1.12: Circular Dichroism (CD) Spectroscopy

CD is widely used to monitor protein secondary structure, and how it can change in proteins due to interactions with proteins, ligands or lipids. In this thesis, CD spectroscopy was used to monitor structural changes in MinE due to membrane interactions, and to monitor any changes in overall structure induced by mutations introduced into this protein. CD detects differences in the ability of a chiral molecule to absorb left- versus right-handed circularly polarized light, where this difference is reported in units of ellipticity θ[85,86]. In proteins, the CD intensity is usually reported as a mean residue ellipticity (MRE) to normalize the signal to the total concentration of peptide bonds in the sample. Peptide bonds in proteins differentially absorb circularly polarized light in the 200-250 nm range in a way that reflects the overall secondary structural content of the protein in which they are found. Each secondary structure type has characteristic features in a CD spectrum. As shown in Fig 1.16, the CD spectrum of an α-helix usually shows maximum ellipticity at 193 nm and minimum ellipticity at 208 nm and 222 nm, whereas β-sheets show a maximum at 196 nm and minimum at 218 nm. Random coil spectra have a minimum at 195 nm and maximum at 212 nm[87–89].

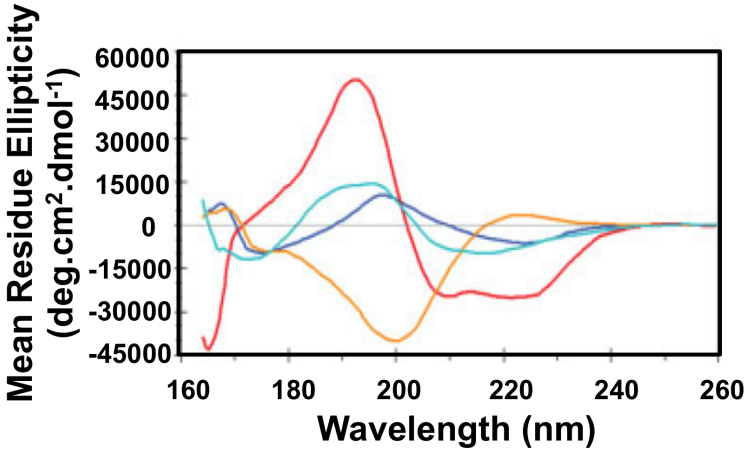

Figure 1.16. Illustration of typical CD spectra arising from different protein secondary structure types. CD spectra are shown for a mostly helical protein such as myoglobin (red), mostly beta sheet protein such as concanavalin A (blue), beta-lactoglobulin (cyan), and a polyproline-rich protein such as collagen (orange). (Reproduced from Whitmore *et al*,[90] with permission).

From the CD spectrum of a protein, secondary structure can be estimated using algorithms that compare the sample spectrum to those in a library of spectra acquired on proteins of known structure. This process is known as secondary structure deconvolution, since contributions to the spectrum from each secondary structure type are estimated[87–89,91,92]. While this can be a useful technique to report on large differences in secondary structure content, it is useful to remember that the accuracy of most structure deconvolution programs remains in the 70-90% range[90,93].

In some cases, it is possible to use changes in CD ellipticity upon ligand binding to estimate apparent binding affinities. In the case of the Min system, this was done to calculate MinE-membrane binding affinities, again using the hill equation:

$$f_b = \frac{\Delta\theta}{\Delta\theta_{max}} = \frac{[\mathrm{PL}]^h}{(\mathrm{K}_{0.5})^h + [\mathrm{PL}]^h} \qquad \text{(Eq. 1.4)}$$

where $\Delta\theta$ is the change in CD ellipticity in MinE in presence and absence of phospholipids (PL), $\Delta\theta_{max}$ is the maximum change in ellipticity induced by saturation of binding, $\mathrm{K}_{0.5}$ is the apparent affinity of MinE-membrane interaction and f_b is the fraction

of lipid-bound MinE protein. A plot of f_b as a function of lipid concentration therefore allows estimation of the apparent affinity of MinE to bind lipid membranes, and h is the Hill coefficient that reports on the degree of MinE binding coopertivity.

1.13: Nuclear Magnetic Resonance (NMR) Spectroscopy

While CD spectroscopy is a useful tool to look at total secondary structure content, NMR spectroscopy is a high-resolution technique that can provide detailed structural and dynamic information at the atomic level. Unlike X-ray crystallography, NMR can also monitor protein motions in the solution state over a wide range of time scales[94,95]. Although NMR is typically limited to macromolecules with sizes of ~25 kDa or less [96], the MinE dimer is ~22 kDa which makes it good target for solution NMR studies. In this thesis, we used solution NMR to probe structural perturbations in MinE caused by mutations.

NMR arises from the magnetic characteristics of nuclei that show intrinsic angular momentum, referred to as spin. Protein NMR mainly uses nuclei with quantum number (I) of ½ such as ^{1}H, ^{15}N and ^{13}C[96]. When these spins are subjected to an external magnetic field (B_o, designated as the z-axis by convention), as is provided by an NMR spectrometer, a dipole moment is induced that precesses about the z-axis at the Larmor frequency (ω_o) according to the equation[97]:

$$\omega_o = \gamma B_o \qquad \text{(Eq. 1.5)}$$

where the gyromagnetic ratio (γ) is an intrinsic property of the nucleus. For these spins, there are two possible orientations, parallel and antiparallel, relative to *Bo*. Transitions between these two states can be induced by absorption of energy provided by the application of a radiofrequency pulse at the Larmor frequency. The ratio of populations between the parallel and antiparallel states is described by the Boltzmann distribution:

$$\frac{N_\alpha}{N_\beta} = e^{-(\frac{\Delta E}{K_B T})} \qquad \text{(Eq. 1.6)}$$

where N_α is the number of spins in low energy state (parallel configuration to magnetic field Bo when γ is positive) whereas N_β is the number of spins in high energy state (anti-parallel configuration for positive γ), ΔE is the energy difference between the two states, k_B is the Boltzmann constant and T is the temperature[98]. This predicts that in a 600 MHz NMR spectrometer, 10001 spins would be in the α configuration for every 10000 spins in the β configuration. Although small, the cumulative effect of this population difference gives raise to a net magnetization vector along the z-axis, and the precession of this bulk magnetization vector is what is detected by the NMR spectrometer. Since the difference between the two population states is very small, NMR is an insensitive technique that requires the use of relatively high sample concentrations; for proteins, this is typically in the range of ~ 0.5 mM or higher[97,99].

NMR detects the absorbance frequencies required to induce the transition between low and high energy states. These absorbance frequencies are dictated by the energy difference between low and high energy spin states (ΔE), which is related to the strength of the external magnetic field given by:

$$\Delta E = h\nu_o = \gamma h B_o \quad \text{where} \quad \nu_o = \frac{\gamma B_o}{2\pi} \qquad \text{(Eq. 1.7)}$$

where h is Planck's constant and ν_o is the Larmor frequency in units of Hz. Thus, the higher the magnetic field strength, the larger the magnitude of the energy difference between states, and the larger the population difference between states, giving rise to an enhancement of signal-to-noise. According to this relationship, nuclei with larger γ values (i.e, protons) are also more sensitive probes for NMR. Due to the low natural abundance and smaller γ for ^{15}N and ^{13}C, isotope enrichment is usually required to use these nuclei in protein NMR[98,100].

Since specific nuclei (e.g. protons) have the same γ value and are subjected to the same external magnetic field, NMR would not be very useful technique if no other factor influenced nuclei absorption frequencies. However, electrons in molecules generate small magnetic fields that change the local magnetic field experienced by each nucleus. This effect changes the absorption frequencies that give raise to the NMR spectrum according to the relationship:

$$\Delta E = \gamma h B_{eff} = \gamma h(1-\sigma) B_o \qquad \text{(Eq. 1.8)}$$

where B_{eff} is the effective magnetic field experienced by the nucleus and σ is the shielding constant that represents the effects of the local chemical environment on the external magnetic field that is sensed by a nucleus[97].

Since absorbance frequencies depend on the strength of spectrometer magnetic field, an NMR spectrum is usually reported in units of chemical shift (δ) in parts per million (ppm), which is defined as the difference in the measured Larmor frequency and that of a reference compound (v_{ref}) such as 2,2-dimethyl-2-silapnetane-5-sulfonic acid (DSS)[97]. DSS is usually used as a reference compound in protein NMR since the protons in its methyl groups are shielded from the external magnetic field more than most protons in protein. The use of an internal reference allows normalization of NMR absorbance frequencies for magnetic field strength according to the following equation

$$\delta = \frac{v_o - v_{ref}}{v_{ref}} \times 10^6 \quad \text{ppm} \qquad \text{(Eq. 1.9)}$$

The size of molecules such as proteins can greatly influence the quality of the NMR signal. Large molecules have slow molecular tumbling rates which leads to efficient loss of the magnetization coherence required to detect the NMR signal[101,102]. This gives rise to broad peaks of low intensity, resulting in low sensitivity and resolution for NMR spectra from large proteins. Peak broadening can also be caused by conformational exchange if it occurs on a millisecond time scale. In this case, spins that sample more than one local chemical environment will have intensity spread over more

than one peak in the NMR spectrum. If the states are relatively long-lived (i.e. at least ms to second timescale) and abundant, then it can be possible to see signals from both species in the spectrum. On the other hand, if exchange between these two states is very rapid (i.e. ps-ns), these two peaks will coalesce into a single sharp peak at the population-weighted average chemical shift. However, if exchange between these states occurs on an intermediate timescale (i.e., μs-ms), these peaks will become broader, and shift towards a population-weighted average chemical shift, making it more difficult to detect in the NMR spectrum[100].

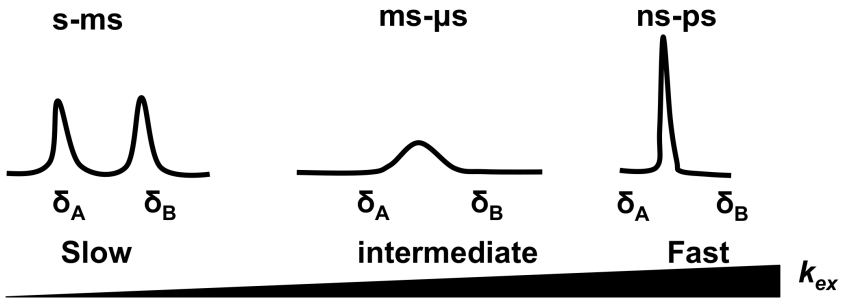

Figure 1.17. Schematic diagram illustrating the effects of exchange rates (k_{ex}) between two states (with chemical shifts δ_A and δ_B) on peak broadening and chemical shifts (δ).

Another challenge in protein NMR is that there are a large number of protons that make it impossible to resolve all signals in a one-dimensional proton NMR experiment. For this reason it is necessary to use multi-dimensional NMR experiments to separate peaks, and provide correlations between spins that are coupled, either through bonds or space. The most commonly used NMR experiment for proteins is the 2D ^{1}H-^{15}N HSQC (heteronuclear single quantum coherence) spectrum[94,97,98,100]. The ^{1}H-^{15}N HSQC experiment gives a 2D spectrum that correlates amide proton chemical shifts on the x-axis with those of the directly bonded nitrogen atom on the y-axis. Ideally, each non-proline residue in a protein sequence gives rise to a single backbone amide peak in this spectrum. Peaks are usually observed from side chain N-H groups as well, specifically, Trp, Asn, Gln, and sometimes Arg and Lys, depending on sample pH. Stably folded proteins display a broad range of chemical shifts in the ^{1}H-dimension while peaks from unfolded proteins would appear in a narrow range of proton chemical shifts. Thus, this

spectrum can be used to report on the integrity of the protein structure, and is also used to determine to evaluate the feasibility of triple-resonance experiments, such as those required to assign chemical shifts.

1.14: Triple Dimensional NMR Experiments to Assign Chemical Shifts

In order to resolve overlapping peaks in two-dimensional NMR spectra and assign chemical shifts to atoms in a protein sequence, triple-resonance 3D experiments can be used[97]. The simplest among these is called the HNCO experiment[103], so named because it correlates amide proton (H) and nitrogen (N) chemical shifts of a residue (i) to that of the carbonyl carbon (CO) in the preceding residue (i-1) as shown in Fig 1.18. The HNCO spectrum can be represented by a cube that is essentially the expansion of the ^{1}H-^{15}N HSQC spectrum into a third dimension that reports on the carbonyl chemical shifts.

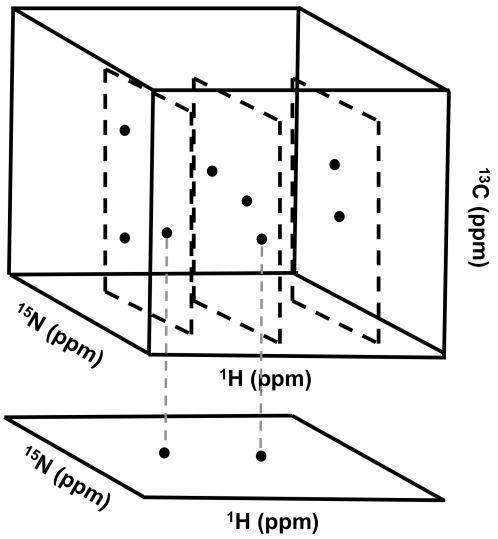

Figure 1.18. Triple resonance 3D cubic representation of HNCO experiment. Amide proton correlated to ^{15}N chemical shifts in 2D-HSQC (lower panel) are separated in carbon dimension (3rd dimension).

Experiments often used to assign protein backbone chemical shifts, and used in this thesis, are the CBCA(CO)NH[104] and HNCACB[105], where chemical shifts of Cα, Cβ, amide ^{1}H and ^{15}N atoms are recorded. The major difference between these two

experiments is that the CBCA(CO)NH experiments shows peaks with amide ^{1}H and ^{15}N chemical shifts of residue (i) correlated with the chemical shifts of Cα, Cβ atoms from the preceding (i-1) residue, while the HNCACB experiment also shows correlations to the carbon atoms from the same residue (i) (Fig 1.19). Each ^{1}H-^{15}N correlation in the HNCACB spectrum therefore typically shows four peaks along the carbon dimension that correspond to Cα and Cβ chemical shifts for residues i and i-1, while the CBCA(CO)NH spectrum will only show these correlations for residue i-1[97].

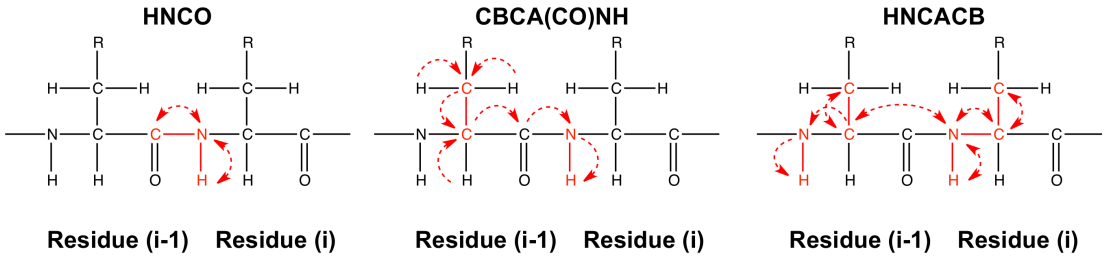

Figure 1.19. Correlations of 3D NMR experiments typically used to assign backbone chemical shifts of a protein. Nuclei involved in magnetization transfer that are correlated in the experiment (red) also indicated in the experiment name.

In addition, the HNCACB spectrum shows Cα peaks with a positive intensity, while Cβ peaks have negative intensities, allowing the two atom types to be easily distinguished. Inter-residue correlations also tend to be weaker than intra-residue correlations. These experiments allow amide proton and nitrogen chemical shifts from sequential residues in a protein sequence to be identified, since the HNCACB spectrum will show identical Cα, and Cβ chemical shifts. Amide peaks arising from adjacent residues can be matched to the protein sequence by comparing the carbon chemical shift to the known range of Cα and Cβ chemical shifts for each amino acid. The process of sequentially assigning chemical shifts is usually facilitated by displaying the data as strips out the 3D cube of data. As shown for the HNCACB spectrum, ^{1}H-^{13}C strips are generated from the plane that is centered on amide proton and ^{15}N chemical shift of one residue (i). In this strip plot, inter-residue peaks have carbon chemical shifts that correspond to the Cα and Cβ shifts of the preceding residue (i-1), which should align with intra-residue peaks in the strip plot for the preceding residue[106] (Fig 1.20). By following

this linkage procedure, backbone chemical shifts from consecutive residues in the sequence can be assigned. Usually it is useful to take advantage of some of the more unique chemical shifts to help match shifts to sequence. For example, Ser and Thr have Cβ shifts that are higher than are found for any other amino acid, glycine has no Cβ chemical shift and the methyl group of alanine has a uniquely low value. This was the general procedure used to assign chemical shifts for MinE in the thesis, which allowed the structure of mutants to be compared to that of wild-type MinE.

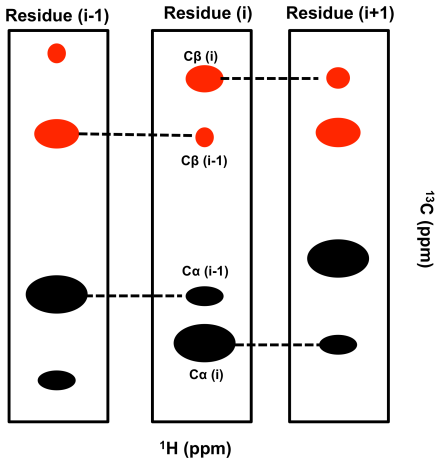

Figure 1.20. Sequential assignment of amide backbone chemical shifts using the HNCACB experiment. ^{1}H-^{13}C strip plots of the HNCACB spectrum are centered at HN and ^{15}N chemical shifts of the residue indicated on top of the strip. Intra and inter residue correlations are shown between Cα peaks (black) and Cβ (red) where intra-residue correlations are more intense relative to inter-residue correlations. Sequential matching between intra and inter-residue peaks from the preceding residue (i-1) is shown by dashed lines.

Chapter 2

Materials and Methods

All chemical reagents specified in this thesis were supplied by Bioshop, otherwise stated.

2.1: Bacterial Plasmids

All Min plasmids; MinD WT and MinE WT, MinE mutants; I24D and I25R and MinE N- terminus truncated mutants ΔMTS were previously described[107]. These were derived from the pET30a vector (EMD Millipore) containing kanamycin resistance for selective screening and a C-terminal hexahistadine tag for nickel affinity chromatography. MinE mutants were made by site-directed mutagenesis using the QuikChange method (Qiagen) as described previously[107]. Briefly, a PCR reaction was set up containing 1X Pfu reaction buffer, 2% dimethyl sulfoxide (Fisher), 0.4 mM dNTPs (BioLabs), 0.3 μM of each forward and reverse primers (Sigma), 0.2 μM DNA template (MinE DNA) and 0.2 μM Pfu DNA polymerase (BioLabs). PCR reactions were placed in Eppendorf Thermal Cycler Personal running the program in table 2.1. All Min plasmids were amplified and sequences confirmed at the Ontario Health Research Institute sequencing facility.

Table 2.1. PCR thermocycle program to generate I25R and I25R ΔMTS mutations.

Step	Temp (°C)	Time (minutes)
1	95	2
2	95	1
3	62	1
4	68	12
5	Go to step 2, (15 cycles)	-
6	72	10
7	4	Hold

Table 2.2. DNA primer sequences used to generate MinE mutants.

Mutant	Primers
6-87	Forward: 5'GTTTAACTTTAAGAAGGAGATATACATATGTTATTCGGTAGAAAGCAG AAAACGGCAACCGTTGCCCG'3 Reverse: 5'CGGGCAACGGTTGCCGTTTTCTGCTTTCTACCGAATAACATATGTATAT CTCCTTCTTAAAGTTAAAC'3
12-87 (ΔMTS)	Forward: 5'GTTTAACTTTAAGAAGGAGATATACATATGCAGAAAACGGCAACCGTTGCCCG CGAC CGCC'3 Reverse: 5'GGCGGTCGCGGGCAACGGTTGCCGTTTTCTGCATATGTATATCTCCTTCTTAAA GTTA AAC'3
I24D	Forward: 5'CGCGACCGCCTTCAAGACATCATTGC'3 Reverse: 5'CTCTTGGGCAATGATGTCTTGAAGGC'3
I25R	Forward: 5'CGCGACCGCCTTCAAATCAGAATTGCCCAA GAGCGC'3 Reverse: 5'GCGCTGTTGGGCAATTCTGATTTGAAGGCG GTCGCG'3

2.2: Plasmid Amplification

E. coli DH5α $CaCl_2$ competent cells were transformed (Section 2.4) and plated on LB-agar plates (10 g/L tryptone, 5 g/L NaCl, 5 g/L yeast extract, 15 g/L agar, 50 μg/mL kanamycin), Cells were allowed to grow overnight at 37 °C (Isotemp incubator, Fisher Scientific). One colony was used to inoculate 35 mL LB media (10 g/L tryptone, 5 g/L NaCl, 5 g/L yeast extract, 50 μg/mL Kanamycin) in a 50 mL polypropylene Falcon tube (Fisher scientific) and placed in Qmax 4000 shaking incubator (Barnstead) overnight at 37 °C at 220 rpm. On day 3, bacterial cells were centrifuged at 4500 xg for 15 minutes at 4 °C using an Avanti J-E centrifuge equipped with JA 25.50 rotor. The bacterial pellet was stored at -20 °C till further purification and analysis. Plasmid DNA purification was carried out using the Qiagen Plasmid Purification Kit following the manufacturer's protocol (3^{rd} edition, 2005). DNA concentrations were determined by absorbance measurements at 260 nm using a Nanodrop spectrometer (Thermo Scientific). A diluted DNA working solution of 10 ng/μL was used for sequencing and transformations.

2.3: Generation of Competent Cells

E. coli BL21(DE3) and DH5α $CaCl_2$ competent cells (Novagen) were regenerated using established protocols[108]. Briefly, cells were streaked on a non-selective LB-agar plate and incubated overnight at 37 °C using an Isotemp incubator. One colony used to inoculate 35 mL of non-selective LB media in a 50 mL polypropylene Falcon tube and cells were allowed to grow using a Qmax 4000 shaker at 37 °C at 220 rpm till the OD reached ~ 0.3 where absorbance readings were taken using an Ultraspec 2100 Pro UV spectrometer. Cells were transferred to ice-cold polypropylene Falcon tubes and incubated on ice for 15 minutes followed by centrifugation at 4500 xg and 4 °C for 10 minutes using an Avanti J-E centrifuge equipped with JA 25.50 rotor. The bacterial pellet was dissolved gently in 10 mL of ice-cold 0.1 M $CaCl_2$ followed by centrifugation at 4500 xg and 4 °C for 10 minutes. The pellet was resuspended in 2 mL of ice-cold 0.1 M $CaCl_2$ containing 15% glycerol and they were divided into 40 µL aliquots followed by flash freezing using liquid nitrogen and storage at -80 °C (Thermo Scientific).

2.4: Transformation

Transformation was carried out according to standard protocols of bacterial chemical competent cells. Briefly, 40 µL aliquot of *E. coli* DH5α and BL21(DE3) $CaCl_2$ competent cells was placed on ice after addition of 2 µL of a 10 ng/µL solution of desired DNA plasmid followed by gentle mixing by flicking. Cells were incubated on ice for 30 minutes. Cells were heat-shocked in a 42 °C water bath (VWR) for 1.5 minutes, followed by incubation on ice for 1 minute. 200 µL of LB broth was added, and cells were allowed to grow in the Qmax 4000 shaker for 1 hour at 37 °C at 220 rpm. After incubation, cells were spread on an LB-agar plate containing 50 µg/mL kanamycin. Cells were allowed to grow overnight at 37 °C using an Isotemp incubator.

2.5: Min Protein Expression

Expression of all Min proteins was carried out using M9 media (42 mM Na_2HPO_4, 22 mM KH_2PO_4, 5 mM NaCl, 1 mM $MgSO_4$, 0.1 mM $CaCl_2$, 0.1 % (w/v)

NH_4Cl, 0.3 % (w/v) D-glucose, 1 % (w/v) LB and 50 μg/mL kanamycin). For NMR samples, $^{15}NH_4Cl$ and ^{13}C-D-glucose were used (Sigma Aldrich). One colony of freshly transformed BL21 cells was used to inoculate 50 mL of M9 media. The culture was allowed to grow at 37 °C and shaking at 220 rpm overnight for 16 hours using Qmax 4000 shaker. On day 3, the culture was transferred into 500 mL of M9 media and incubated in a Qmax 5000 shaking incubator (Barnstead) at 220 rpm, 37 °C for 3 hours till OD reaches ~0.5-0.7. The culture was induced with 0.5 μM of isopropyl β-D-1-thiogalactopyranoside (IPTG) and allowed to grow overnight for 16 hours at 16 °C for full length MinD and MinE proteins, or 37 °C for truncated MinE. Cells were divided into 250 mL Nalgene centrifuge bottles (Fisher) and harvested using an Avanti J-E centrifuge equipped with JA 16.25 rotor at 6000 xg at 4 °C for 10 minutes. The pellet from the 500 mL culture was placed in Falcon tube and stored at -20 °C till further purification. During the process of protein expression, 1 mL of bacterial growth was taken for SDS-PAGE analysis. The sample was centrifuged at 16,000 xg using a tabletop Eppendorf 5415 D centrifuge for 1 minute. The pellet was dissolved in 50 μL of ddH_2O and 50 μL SDS-PAGE sample loading buffer was added, followed by storage at -20 °C.

2.6: Min Protein Purification

A bacterial pellet from 500 mL of expression culture was resuspended in 15 mL of lysis buffer containing 50 mM Tris pH 8.5, 250 mM NaCl,10 mM imidazole 1 mg/mL benzamidine and allowed to incubate on ice for 30 minutes using a rocking platform (VWR).

In the case of full length MinE I24D, 1X cocktail inhibitor (1mg/mL 4-(2-aminoethyl) benzenesulfonyl fluoride hydrochloride (AEBSF), 2 μg/mL pepstatin, 1.2 μg/mL E-64, 1 μg/mL bestatin, 1.6 μg/mL phosphoramidon) was added to the lysis buffer to prevent proteolysis. After incubation, cells were homogenized twice using a homogenizer (Avestin Emulsiflex-B15) under 60 bar of air pressure and 80 bar of valve pressure. The homogenizer was washed with 15 mL of ddH_2O, 70 % (v/v) ethanol, ddH_2O in sequence before and after use. Cells lysates were transferred to a 25 mL Nalgene centrifuge tube (Fisher) and spun at 16000 xg for 20 minutes at 4 °C using an

Avanti J-E centrifuge equipped with JA 25.50 rotor. The supernatant was immediately transferred to a 2.7 cm inner diameter column (Kimble) containing 15 mL of lysis buffer and 5 mL of Ni-NTA resin (Qiagen) that already has been equilibrated with 15 mL lysis buffer. The supernatant was incubated with the resin for 5 minutes to maximize binding, and then the resin was washed twice with 25 mL of lysis buffer, and twice with washing buffer (lysis buffer with 20 mM imidazole). 10 mL of elution buffer (lysis buffer contains 500 mM imidazole) was added to resin and allowed to incubate for 5 minutes. The resin was also washed twice with 10 mL of elution buffer to maximize yields. 0.5 mM EDTA pH 8.5 was added to the elutant to inhibit protease activity. The resin was cleaned by washing twice with 25 mL of ddH_2O followed by storage in 10 mL of 20 % (v/v) ethanol to prevent microbial growth.

Full length MinE I25R was expressed into the insoluble fraction, and therefore needed to be purified under denaturing conditions, followed by on-column refolding during the affinity chromatography. Briefly, cells were lysed and homogenized as mentioned before. After centrifugation, the bacterial pellet containing MinE I25R was suspended in freshly made lysis buffer containing 8 M urea. The suspension left to incubate overnight on a rocking platform at room temperature. Next day, the suspension was centrifuged at 25000 xg and 20 °C for 25 minutes. The supernatant was applied to Ni-NTA resin that has been equilibrated with 5 mL of lysis buffer with 8 M urea, and allowed to incubate for 5 minutes. The resin was washed twice with 25 mL of a series urea dilutions in lysis buffer (6 M, 4 M, 2M Urea), followed by two washes with lysis buffer. The affinity chromatography purification was then performed from the wash step onward as described above.

The elutant was concentrated using an Amicon Ultra concentration device (3 kDa, 10 kDa and 30 kDa MWCO for MinE TSD, MinE and MinD respectively). The concentration device was equilibrated with 8 mL of lysis buffer by centrifugation at 5000 xg for 5 minutes at 4 °C using an Avanti J-E centrifuge equipped with JA 25.50 rotor. Samples were added to the device and spun for 10 minutes intervals to a final volume of 4 mL for full length MinD and MinE or 2 mL for MinE truncated mutants. The sample was transferred to a Falcon tube and centrifuged for 2 minutes at 5000 xg at 4 °C to discard aggregates.

An automated protein chromatography system (AKTA FPLC) attached to a 10/300 Superdex 75 size exclusion chromatography column (GE healthcare) was equilibrated with 2 column volumes (50 mL) of exchange buffer containing 50 mM Tris pH 8.5, 100 mM NaCl and 0.2 mM EDTA. A 2 mL sample injection loop was attached to the FPLC valve and flushed with 5 mL of exchange buffer before and after use. 2 mL of sample was injected with a 0.5 mL/min flow rate and 0.5 mL fractions were collected where the elution profile was monitored by absorbance at 280 nm. The purified proteins were stored at 4 °C till further uses. In case of full length I24D, 1X cocktail inhibitor was also added to protein fractions after FPLC.

50 µL samples were taken and mixed with 50 µL of 2X sample loading buffer for SDS-PAGE analysis at each step of purification to assess the purity of the proteins. Representative samples of gels analyzing fractions from purifications are shown in Figure 2.1.

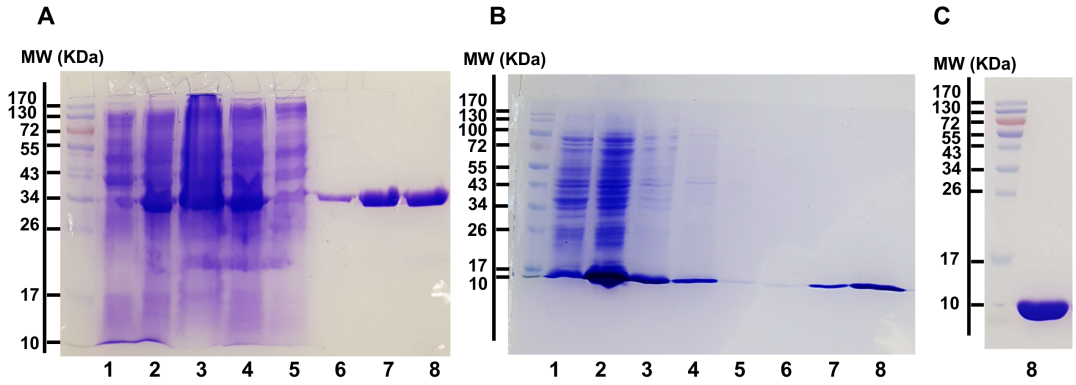

Figure 2.1. SDS-PAGE analysis of fractions taken from purification of MinD (A), WT MinE (B) and ΔMTS MinE (C). Samples were taken from the bacterial culture before (lane 1), and after induction of expression (lane 2), cell lysate after homogenization (lane 3), and the supernatant after centrifugation (lane 4). Samples were also taken from nickel affinity chromatography after the lysis buffer wash (lane 5), 30 mM imidazole wash (lane 6) and elution with 500 mM imidazole (lane 7). Purified samples taken after size exlucusion chromatography are shown in lane 8.

2.7: Ni-NTA Regeneration

Ni-NTA resin was regenerated after being used for ~5 purifications using protocols suggested by QIAexpressionist handbook on nickel affinity chromatography (5th edition). The resin was washed with 2 volume (10 mL) of regeneration buffer

containing 6 M Gu-HCl and 0.2 M acetic acid, 5 column volumes with ddH_2O, 3 column volumes of 2 % (w/v) SDS, 1 column volume of 25 %, 50 %, 75 % (v/v) of ethanol, 5 column volumes of 100 % (v/v) ethanol, 1 column volume of 75 %, 50 % and 25 % (v/v) ethanol and 5 column volumes of ddH_2O. The resin then washed with 5 column volumes of 100 mM EDTA pH 8 to strip nickel ions and 5 column volumes of ddH_2O. The resin was recharged with 2 column volumes of 100 mM $NiSO_4$ then washed with 5 column volumes of ddH_2O. The resin was then washed with 1 column volume of regeneration buffer followed by a 1 column volume wash with ddH_2O. Finally, the resin was stored in 20 % (v/v) ethanol to prevent microbial growth.

2.8: Estimation of Protein Concentrations

Min protein concentrations were determined using bicinchroninic acid (BCA) assay as outlined by the manufacturer's manual (Pierce). To construct a protein concentration standard curve, a serial dilution of 20, 40, 80, 160, 320, 400, 600 and 800 µg/mL of bovine serum albumin (BSA) (Sigma Aldrich) in ddH_2O were made and stored at 4 °C. 1 mL of working solution contains 50 parts of reagent A (200 mM sodium carbonate, 120 mM sodium bicarbonate, 10 mM sodium tartrate, 0.1 M sodium hydroxide and 30 mM bicinchroninic acid) and 1 part of reagent B (4 % w/v cupric sulphate) was added to 50 µL to each standard and unknown sample. The mixture was incubated at 37 °C for 30 minutes using an Isotemp incubator, and absorbance readings at 562 nm on an Ultraspec 2100 pro UV spectrometer, plotted as a function of BSA concentration, and the linear relationship used to determine concentrations of purified samples.

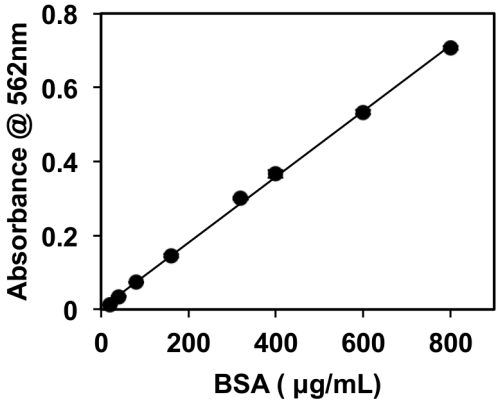

Figure 2.2: Representative sample of the BSA standard curve. Standard errors for each point obtained from 3 independent trials are smaller than the size of the symbols.

2.9: Phospholipid Vesicle Preparation

E. coli total lipid extract was purchased in powder form from Avanti lipid. In glass test tube, lipids were dissolved in chloroform (Fisher) and evaporated under a constant stream of argon gas for 20 minutes in the fume hood. The tube was placed in a glass Erlenmeyer flask and stored in a chamber evacuated with a vacuum pump overnight to remove any residual chloroform. On the next day, the lipid film was dissolved in 1X reaction buffer containing 25 mM Tris pH 8, 50 mM KCl to make a lipid stock of 10 mg/mL. The solution was vortexed several times to ensure that lipids were fully dissolved. A lipid extruder (Avanti lipids) was used to obtain small unilamellar vesicles (SUVs) according to the manufacturer's protocol. Briefly, the extruder was washed with ddH_2O, and then the *E. coli* phospholipid solution was incubated in a Hamilton syringe for 5 minutes at 52 °C to promote lipid fluidity followed by extrusion through a 1 µm then 0.1 µm polycarbonate filter (Avanti lipids). The lipids solution was passed 20 times through each filter to maximize sample homogeneity. SUVs were typically used on same day but could be stored in 4 °C for a maximum of 4 days. For other types of lipids, such as DOPC, DOPG, and POPG, extrusion was preformed at room temperature with a 0.1 µm polycarbonate filter only. To make lipid mixtures for the MinD ATPase assay, different volumes of 25 mg/ml chloroform-dissolved lipids stocks were added to a glass

test tube and mixed using a glass pipette before vesicles were made by using the procedure described mentioned above.

2.10: Malachite Green Colorimetric Assay

Three volumes of 0.2 % (w/v) malachite green (Fisher) dissolved in 3 M HCl (Fisher) was mixed with one volume of 10 % (w/v) molybdic acid dissolved in 3 M HCl and vortexed. The mixture was covered with tin foil and incubated on a rocking platform for 30 minutes at room temperature. The mixture was passed through 0.22 μm sterile filter (Millipore) to remove undissolved particles, and stored at 4 °C. A serial dilution of potassium phosphate was prepared to generate a malachite green standard curve. The malachite green dye was diluted by 4.25 fold in ddH_2O (0.035% (w/v) malachite green, 0.6% (w/v) molybdic acid) with Tween-20 (Fisher) was added to a final concentration of 0.15% (v/v). The dye was covered in tinfoil and incubated on a rocking platform for 30 minutes at room temperature. 85 μL of malachite green dye was added to a polystyrene 96 well microplate (Fisher) followed by addition of 15 μL of either potassium phosphate or a MinD ATP hydrolysis sample. The mixture was mixed gently by pipetting to avoid introducing air bubbles, and then allowed to incubate at room temperature for 15 minutes followed by an absorbance measurement at 620 nm using Spectramax XS plate reader. Typically, MinD ATP hydrolysis produced a maximum amount of phosphate ~ 1 nmol or less. The slope of the standard phosphate curve was used to calculate the amount of phosphate generated during the MinD ATPase assay.

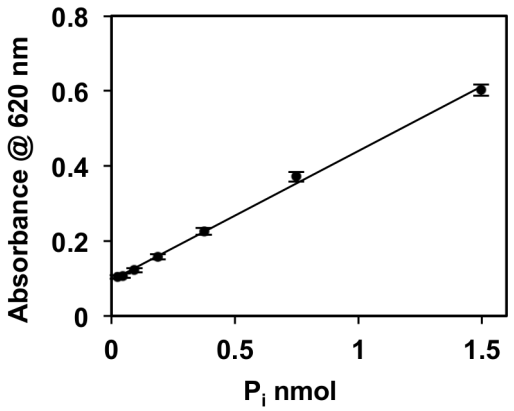

Figure 2.3: Representative example of a phosphate standard curve used to convert absorbance readings into phosphate concentrations. Error bars for each point represent standard error obtained from 3 independent trials.

2.11: MinD ATPase Activity Assay

MinD ATPase assay reactions were preformed in 65 mM Tris pH 8.2, 80 mM NaCl, 50 mM KCl, 0.16 mM EDTA, 5 mM $MgCl_2$, 0.5 mg/mL phospholipids and 1 mM ATP. 2.7 μM MinD was chosen based on previously established in vitro MinE-stimulated MinD ATPase assay[43]. In these reactions, ATP was the last component added to the reaction. Mixing by pipetting gently after adding each component was preformed in order to mix the reaction sample. 35 μL reaction aliquots were taken at different time points of the reaction and incubated in a boiling water bath for 1 minute to quench the reaction. Aliquots were centrifuged at 16000 xg for 2 minutes using tabletop Eppendorf 5415 D. Free phosphate produced by the hydrolysis of ATP was estimated using the malachite green method (Section 2.10). Absorbances were plotted as a function of time, and gave rise to a linear relationship where the slope represents the initial MinD ATP hydrolysis rate. To determine MinD specific activity, initial rates were converted into phosphate concentrations and normalized to MinD mass (mg). In MinD ATPase assays, error bars represent the standard error calculated from three independent trials with different MinD preparations. These MinD ATPase initial rates were fit to the Hill equation (Eq. 1.4) to generate a sigmoidal curve allowing estimation of kinetic parameters, namely maximal activity (V_{max}), MinD-MinE apparent binding affinity ($K_{0.5}$) and Hill coefficient (h).

2.12: Gel Electrophoresis

SDS-PAGE analysis was preformed using the Laemmli protocol [109]. Briefly, 1 part of a sample was mixed with 1 part of 2X sample loading buffer containing 20% (v/v) glycerol, 4 % (w/v) SDS, 0.01 % (v/v) bromophenol blue, 0.02 % (v/v) 2-mercaptoethanol (Fisher) in 125 mM Tris pH 6.8. After incubation in a boiling water bath for 5 minutes, 20 μL of each sample and 5 μL EZ-RUN prestained Rec protein marker (Fisher) were loaded onto SDS-polyacrylamide gel with 5 % stacking gel containing 5 % (v/v) acrylamide mix (acrylamide: bis-acrylamide, 29:1) (Fisher), 0.1 % (w/v) SDS, 0.1 % (w/v) ammonium persulfate (Fisher), 0.06 % (v/v) TEMED (Fisher) in 125 mM Tris pH 6.8, and with 15 % resolving gel (15 % (v/v) acrylamide mix in 560 mM Tris pH 8.8). Gels were run in a PROTEAN electrophoresis cell (Bio-Rad) for 85 minutes at 180 V in Tris-glycine running buffer containing 0.3 % (w/v) Tris pH 8.5, 1.44 % (w/v) glycine and 0.1 % (w/v) SDS.

Gels were rinsed in ddH_2O and microwaved for 30 seconds and repeated 3 times. Gels were stained by Coomassie blue stain solution containing 0.1 % (w/v) Coomassie brilliant blue G-250, 50 % (v/v) methanol and 10 % (v/v) acetic acid and heated for 30 seconds in a microwave, and left on a rocking platform for 20 minutes. For destaining, gels were washed with ddH_2O, and then soaked in destaining solution containing 50 % (v/v) methanol and 10 % (v/v) acetic acid for 1 hour followed by storage in ddH_2O before scanning.

2.13: Circular Dichroism Spectroscopy

The secondary structure of MinE and conformational change upon interaction with *E. coli* lipids were assessed using circular dichroism (CD) spectroscopy. Purified MinE samples obtained from FPLC in exchange buffer were exchanged into CD buffer containing 10 mM Tris pH 8.5 and 130 mM NaCl. The buffer exchange was performed using an equilibrated 10 kDa MWCO concentration device, except for TSD where a 3 kDa MWCO was used. Purified MinE fractions from the FPLC purification were pooled together and centrifuged at 5000 xg and 4 °C for 10 minutes. The retained solution was mixed by gentle pipetting and the volume topped up with 10 mL of CD buffer. The

exchange process was repeated until 40 mL of CD buffer was used. The protein was then concentrated to ~ 1 mL, which served as a stock solution for CD experiments. For CD experiments, a 0.1 cm CD quartz cuvette (Hellma) was cleaned by soaking in nitric acid overnight followed by rising with ddH_2O for 1 hour. The cell was then washed with 70% ethanol and dried under gentle stream of argon gas. CD samples typically contained ~12 μM MinE. For experiments with lipids, 10 mM Tris pH 8.5 was used with 2 mg/mL phospholipids, whereas 0.5 mg/mL were used in the presence of truncation mutants. Spectra were acquired using a JASCO J-815 spectropolarimeter from 200 to 250 nm using 8 accumulations at 20 nm/min and a data integration time of 8 seconds. In case of full length I25R, 10 nm/min and 32 second data integration times were used instead.

Thermal denaturation experiments were performed with 12 μM MinE and monitored by CD with a 0.2 nm pitch and 1 nm bandwidth at 218 nm, while the temperature was increased from 25^{o}C to 99 ^{o}C at a rate of 2 ^{o}C per minute. Melting temperatures were calculated using a differential melting curve. Briefly, the thermal unfolding transition consists of 3 phases; the pre-transition baseline, inflection point and post-transition baseline. To measure the inflection point of the melting curve (T_m), the change in enthalpy of thermal unfolding (ΔH) and thermal melt can be fitted to

$$\theta = \frac{(y_n + m_n T) + (y_d + m_d T)K}{1 + k} \qquad \text{(Eq. 2.1)}$$

where θ is the ellipticity observed at temperature T, y_n and y_d are y-intercepts of pre- and post-transition baseline phases respectively, m_n and m_d are the slopes of pre- and post transition phases, respectively, and K is the equilibrium constant measured from the Van't Hoff relationship below

$$K = \exp\left(\frac{\Delta H m}{R}\left(\frac{1}{T_m} - \frac{1}{T}\right)\right) \qquad \text{(Eq. 2.2)}$$

where R is the gas constant. According to eq. 2.1 and 2.2, both pre-and post-transition baselines are required to determine T_m and ΔH_m from the thermal unfolding curve. However, T_m and ΔH_m can be still measured by fitting the differential form of the thermal

unfolding curve since the fit does not require transition baselines. The average slope of the curve is represented by

$$\frac{d\theta}{dT} = Af(1-f)T^2 \qquad \text{(Eq. 2.3)}$$

where A is a scaling factor and f is the fraction of denatured protein at temperature T that is calculated using equation 4 where the average slope of the thermal unfolding curve was sampled over 2 degree intervals.

$$f = \frac{K}{K+1} \qquad \text{(Eq.2.4)}$$

To confirm that the stability of I25R ΔMTS is comparable to that of WT ΔMTS, melting curves were also preformed in presence of 2 M urea. Secondary structure deconvolution was carried out using CD Pro software (JASCO) with CONTIN algorithm and SP43 reference set where errors represent standard errors of independent triplicates[93,110,111].

2.14: Nuclear Magnetic Resonance Spectroscopy

NMR spectra were recorded at the University of Ottawa NMR Facility at 298 K using a 600 MHz Bruker AvanceIII spectrometer equipped with a pulse-field gradient triple-resonance cyroprobe. Uniformly ^{15}N or ^{13}C-labeled protein was overexpressed and purified as described above. FPLC fractions were pooled together and the buffer was exchanged in a procedure similar to that described in Section 2.13, with at least 40 mL of NMR buffer containing 25 mM Tris pH 7.2, 50 mM NaCl, 0.1 mM EDTA to limit proteolysis, 0.02 % (w/v) NaN_3 (Sigma Aldrich) to prevent microbial growth. Sample was concentrated to 0.5-0.7 mM and ~ 300 µL with an addition of 10 % (v/v) D_2O (Sigma Aldrich). Sample was loaded into a NMR tube that was soaked overnight in nitric acid followed by washing with continuous stream of ddH_2O for ~ 2 hours, then with 70

% (v/v) ethanol, and dried using argon gas. ^{1}H, ^{15}N and ^{13}C backbone chemical shifts were assigned using standard triple-resonance techniques involving ^{15}N HSQC, HNCO, CBCA(CO)NH and HNCACB spectra which were processed by NMRPipe[112] and analyzed by NMRView[113]. Differences in average backbone chemical shifts (Δδ) between WT ΔMTS and I25R ΔMTS were determined using

$$\Delta\delta = \sqrt{\frac{1}{2}(\Delta\delta_{HN}^2 + 0.14\ X\ \Delta\delta_N^2)} \qquad \text{(Eq. 2.5)}$$

whereas, $\Delta\delta_{HN}$ and $\Delta\delta_N$ are chemical shift differences calculated for amide proton and nitrogen atoms, respectively[114]. Secondary chemical shifts for backbone atoms are also calculated from random coil values[115].

Chapter 3

Dissecting the Role of Conformational Change and Membrane Binding by the Bacterial Cell Division Regulator MinE in the Stimulation of MinD ATPase Activity

Collaborators contributions:

Results from this chapter have been published:
Saud H. Ayed, Adam D. Cloutier, Laura J. McLeod, Alexander C. Foo, Adam M. Damry and Natalie K, Goto. Dissecting The Role of Conformational Change and Membrane Binding by The Bacterial Cell Division Regulator MinE in The Stimulation of MinD ATPase Activity. 2017. *J Biol Chem*. 292 (50): 20732-43.

Adam D. Cloutier and Adam, M Damry helped to perform and analyze NMR experiments for I25R ΔMTS. Laura, J McLeod designed, executed and analyzed membrane affinity measurements. Alexander C. Foo helped with experiment design throughout. Authors are thankful to Dr. Jeffery Keillor for allowing the use of the CD instrument and Jiayi Wu for her assistance with the purification of I25R.

3.1: Introduction

A striking feature of the series of interactions that give rise to the Min protein oscillation cycle is a dramatic conformational change in the MinE regulator of MinD ATPase activity. In the absence of MinD, MinE forms a dimeric 6-stranded β-sheet[43]. However, biochemical and genetic studies monitoring the effect of mutations in MinE dimeric interface region provided strong evidence that many residues critical for the MinD interaction are located in this central β-strand, raising questions about how MinD could access these residues[43,71]. These apparent contradictions were reconciled in a subsequent crystal structure determined for MinD in complex with MinE that showed that these residues no longer localized to the central β-strand of the dimer interface but instead were excluded from the sheet, adopting an α-helix that made intimate contacts with a hydrophobic groove formed by the MinD dimer interface[77]. Taken together, these data gave rise to a model where MinE undergoes a structural transition from a 6-stranded state that would be able to diffuse through the cytoplasm to the 4-stranded state that was observed in complex with MinD.

In this work, we seek to identify the triggers required to induce this structural change in MinE to and determine how these are linked to its ability to stimulate MinD-catalyzed ATP hydrolysis. Our results show that MinE from *N. gonorrhoeae* (*ng*MinE)[47] undergoes a structural transition upon binding membranes composed of *E. coli* lipids with a change in secondary structure that is consistent with the adoption of a 4-stranded structure. However, an N-terminal truncation mutant lacking the membrane-targeting sequence (ΔMTS) stimulated higher rates of MinD-catalyzed ATP hydrolysis than wild-type *ng*MinE, demonstrating that membrane binding is not required to stimulate MinD and that the MTS has an inhibitory effect on the rate. Instead, the conformational change required for MinD binding is fast relative to the overall rate of the cycle, because a mutant of ΔMTS in the 4-β-stranded state did not change ATP hydrolysis rates. This conformational change appears to depend on Ile-25, although activity could be restored if the same mutation was introduced into full-length *ng*MinE, suggesting a role for MinE interactions with both MinD and the membrane in the stimulation of MinD activity. Overall, these data provide new insights into the triggers for conformational change and

the role of membrane binding by MinE in the MinD ATPase cycle that underlies oscillation *in vivo*. This gives rise to a new model where MinE interacts with MinD via an encounter complex that facilitates MinE interactions with the membrane, with MinE dissociation from the membrane comprising the rate-determining step in the ATP hydrolysis–Min protein interaction cycle.

3.2: Results

3.2.1: Structural and Functional Impact of MinE–Membrane Interactions

MinE from *Escherichia coli* (*ec*MinE) is capable of undergoing direct interactions with the membrane via its N-terminal amphipathic helix[52,77,116,117], called the MTS. Whereas previous studies have shown that a structural change accompanies membrane binding [77,116], the nature of this change and its relationship to the 4-stranded MinD-bound conformation have not been determined. Using *ng*MinE[12], which shares 42% sequence identity with *ec*MinE and can functionally complement the Min system in *E. coli*[13,28] , we monitored the structural change induced by membrane interactions using CD spectroscopy. As shown in Fig. 3.1A, the CD spectrum of *ng*MinE undergoes a change in shape and amplitude in the presence of small unilamellar vesicles (SUVs) composed of *E. coli* lipids. Secondary structure content based on spectral deconvolution[110] suggests that this change arises from a loss of β-structure and concomitant increase in α-helix (Table 3.1). As expected, this lipid-dependent change in the CD spectrum is not observed in an *ng*MinE N-terminal deletion mutant that is missing the MTS (ΔMTS) (Fig. 3.1B), which has a CD spectrum that is almost identical to that of the full-length protein (Fig. 3.1C). The loss of β-structure suggests that *ng*MinE may adopt a 4-stranded state when bound to the membrane, similar to what was observed in the MinD-bound structure.

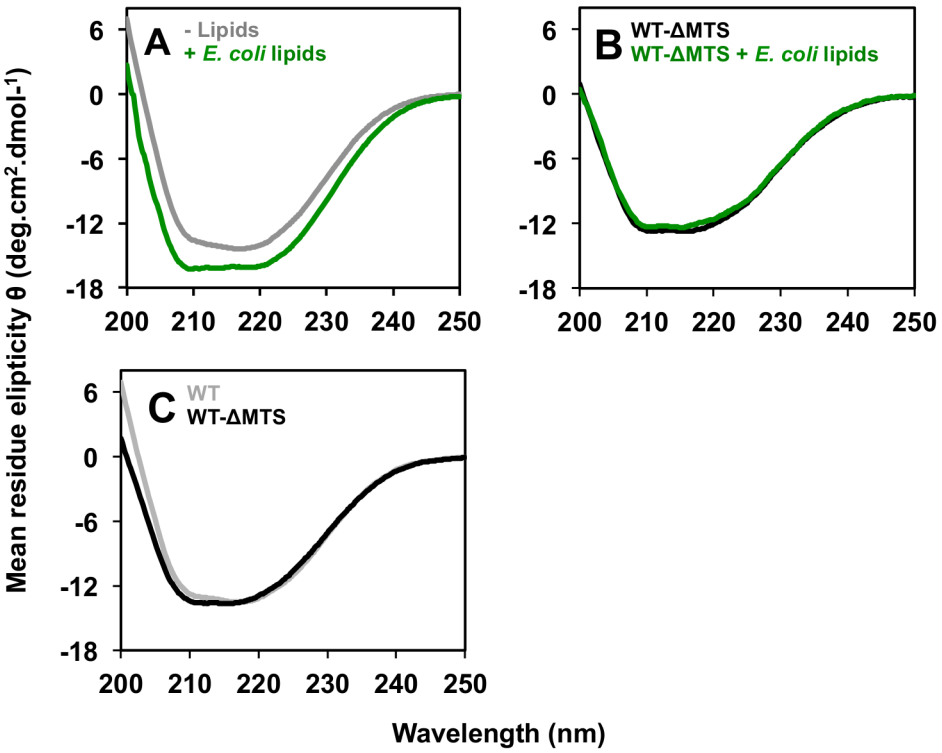

Figure 3.1. MinE–membrane interaction probed by CD spectroscopy. A) CD spectrum of 15 µM *ng*MinE in the absence (gray) and presence (green) of 2 mg/ml *E. coli* lipid SUVs. B) CD spectrum of 12 µM WT-ΔMTS in the absence (black) and presence (green) of 0.5 mg/ml SUVs made from *E. coli* lipids. C) CD spectrum of 12 µM WT (gray) and WT-ΔMTS (black) *ng*MinE.

Table 3.1. Secondary structure content estimated from CD spectra

Sample	Helical %	Sheet %	Random %	Turn %
WT	32 ± 3	20 ± 2	17± 3	32 ± 5
WT + *E. coli*	35 ± 2	15 ± 2	16 ± 4	34 ± 6
ΔMTS	30 ± 3	21 ± 1	20 ± 1	29 ± 2
I24D	35 ± 4	11 ± 3	23 ± 1	27 ± 1
I24D-ΔMTS	36 ± 3	15 ± 2	22 ± 1	27 ± 1
I25R	30 ± 4	22 ± 2	20 ± 1	29 ± 1
I25R-ΔMTS	30 ± 3	22 ± 1	19 ± 1	30 ± 1

Based on the lipid-dependent increase in ellipticity at 208 nm in the *ng*MinE CD spectrum, it was possible to measure the apparent affinity of the MinE–membrane interaction as the lipid concentration required for half-maximal binding ($K_{0.5}^{PL}$), which was found to be 0.52 ± 0.04 mM for *E. coli* lipids (Fig. 3.2). In contrast with previous affinity measurements on supported lipid bilayers with mixtures of synthetic lipids[117], *ng*MinE

binding was best fit to a cooperative model, with a Hill coefficient of 1.9 ± 0.1, where binding of one subunit to the membrane enhanced the affinity of the second subunit to bind the membrane. However, in our experiments, the interaction was indirectly monitored through the binding-induced change in conformation, and therefore the cooperativity observed by this method suggests that the structural change induced in *ng*MinE upon lipid binding by the first MTS is sufficient to induce the conformational change in both subunits of the dimer. Consistent with this idea, the same degree of cooperativity was obtained when SUVs composed of the anionic lipid DOPG were used (Fig. 3.2). This cooperativity in the lipid-dependent change in the CD spectrum of *ng*MinE is consistent with a structural transformation from the native 6-β–stranded state to the 4-β–stranded structure that binds MinD.

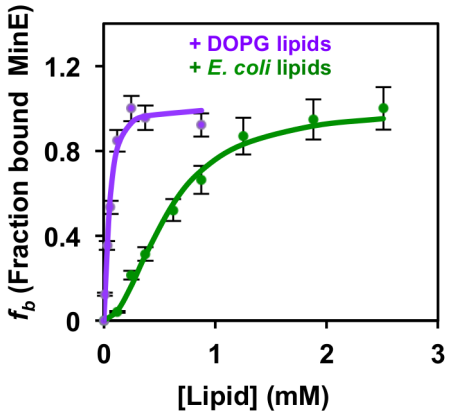

Figure 3.2. MinE-lipid binding affinities measured by CD. The lipid-bound fraction of 15 μM *ng*MinE with SUVs made from DOPG (purple) and *E. coli* lipid extract (green) as determined by ellipticity measured at 208 nm and fit to the Hill equation, with $K_{0.5}^{PL}$ of 520 ± 40 and 40 ± 4 μM, and Hill coefficient of 1.9 ± 0.1 and 2.0 ± 0.1 for *E. coli* and DOPG lipids, respectively.

To assess the impact of the MinE–membrane interaction on its ability to stimulate MinD-catalyzed ATP hydrolysis, activity profiles were acquired for *ng*MinD in the presence of full-length or ΔMTS *ng*MinE. As shown in Fig. 3.3B, there is a cooperative increase in MinD-catalyzed ATP hydrolysis rates with increasing concentrations of *ng*MinE that could be fit to the Hill equation as described previously[43] to allow determination of the maximal activity (V_{max}) from which it is possible to calculate k_{cat}, the concentration of *ng*MinE required for half-maximal saturation ($K_{0.5}^{MinE}$) and Hill

coefficient (*h*) (Table 3.2). This analysis indicates that removal of the N-terminal helix leads to an increase in V_{max}, indicating that the interaction between *ng*MinE and the membrane actually has an inhibitory effect on the Min reaction cycle. The Hill coefficient is slightly greater than 2 in both cases, suggesting longer-range interactions between MinD dimers that allow ATP hydrolysis at one site to enhance hydrolysis at two or more other sites, even in the absence of the MinE MTS. In addition, $K_{0.5}$ MinE is higher for ΔMTS, which may be interpreted as a lower apparent affinity for *ng*MinE binding to *ng*MinD in the absence of the MTS. Overall, the ability of ΔMTS to promote higher levels of *ng*MinD activity demonstrates that direct interactions between MinE and the lipid membrane are not required for stimulation of MinD ATPase activity.

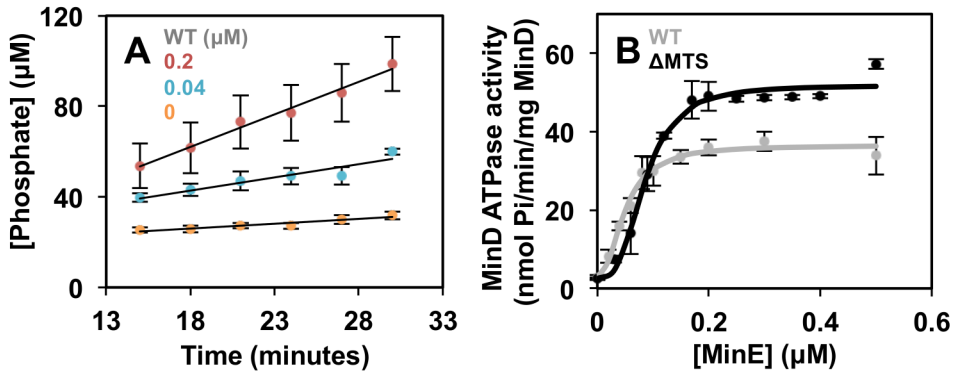

Figure 3.3. MinE–membrane interaction probed by MinE-stimulated MinD ATPase activity. A) phosphate concentration monitored as a function of time for MinD catalyzed ATP hydrolysis with no WT *ng*MinE (orange) or with 0.04 μM (cyan) and 0.2 μM (red) *ng*MinE. The slope of each data series corresponds to the initial reaction rate with the indicated amount of *ng*MinE. B) Initial rates of MinE-stimulated MinD-catalyzed ATP hydrolysis as a function of MinE concentration fit to the Hill equation with WT (gray) and ΔMTS *ng*MinE (black). Error bars, S.E. for each data point from three independent replicates. Kinetic parameters obtained from all fits are summarized in Table 2.

Table 3.2. Kinetic parameters of *ng*MinE-stimulated MinD ATP hydrolysis

MinE	k_{cat} (min^{-1})	$K_{0.5}$ (μM)	*h*
WT	1.1 ± 0.1	0.070 ± 0.008	2.7 ± 0.4
ΔMTS	2.0 ± 0.1	0.100 ± 0.009	2.6 ± 0.3
I24D ΔMTS	1.97 ± 0.01	0.10 ± 0.03	2.0 ± 0.5
I24D	2.0 ± 0.2	0.14 ± 0.02	2.2 ± 0.3
I25R	1.5 ± 0.1	0.18 ± 0.04	1.8 ± 0.2
12-30	2.0 ± 0.1	0.28 ± 0.07	3 ± 1

3.2.2: MinE 4-Stranded β-Sheet Structure Induced by I24D Mutation

Whereas it was surprising that the membrane-MinE interaction was not necessary to stimulate MinD activity, we postulated that the 6- to 4-β–stranded conformational transition might also present a barrier to the activation of MinD. To test this hypothesis, the *ng*MinE residue Ile-24 was mutated to an aspartic acid (I24D) because the introduction of a negatively charged side chain in the hydrophobic core of the 6-stranded state would be expected to destabilize this structure to favor the 4-stranded state, as was observed with the I24N mutant used to capture the open state of *ec*MinE by X-ray crystallography[77]. As shown in Fig. 3.4, the CD spectrum of I24D showed significant differences from the WT spectrum, with some similarities in shape to that of the WT spectrum acquired in the presence of phospholipids. Secondary structure deconvolution suggests that this mutant has helix and β-sheet content that is similar to that of the membrane-bound state of WT *ng*MinE (Table 3.1), as would be expected for the 4-stranded state. In addition, size exclusion chromatography showed similar elution profiles for WT and I24D samples, confirming that the mutant remains dimeric, as was seen for *ec*MinE I24N[77]. Although we were interested to monitor structural changes of I24D in the presence of lipids using CD spectroscopy, poor solubility of vesicle-bound I24D made it impossible to pursue this analysis.

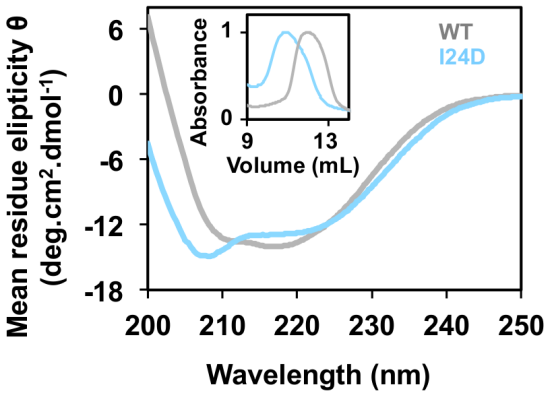

Figure 3.4. CD spectra and size exclusion chromatography characterization of I24D in full-length *ng*MinE. CD spectra of full-length I24D (light blue) with WT (gray). The insets show size exclusion chromatography profiles that confirm a dimeric state for each sample.

Although we were interested in pursuing higher-resolution structure determination to confirm the 4-stranded state in I24D, only low concentrations could be maintained in solution, with the exposed hydrophobic surface of the amphipathic MTS helix probably promoting aggregation. To facilitate higher-resolution structural studies of this mutant, the I24D mutation was also introduced into the more soluble ΔMTS variant. As shown in Fig. 3.5A, CD spectroscopy showed features similar to those of the full-length I24D mutant, with secondary structure deconvolution also indicating a loss of β-sheet content relative to the WT ΔMTS, as expected for the 4-stranded state. As expected, CD spectra of I24D ΔMTS in the presence and absence of *E. coli* lipids are superimposable, confirming that this construct is unable to bind to membranes (Fig. 3.5B).

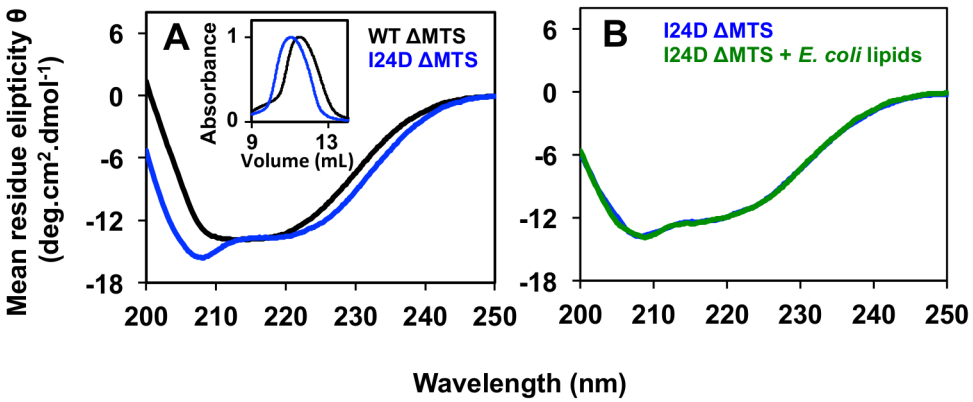

Figure 3.5. CD spectra and size exclusion chromatography characterization of I24D ΔMTS *ng*MinE. A) CD spectra of I24D ΔMTS (blue) and WT- ΔMTS (black). The insets show size exclusion chromatography profiles that confirm a dimeric state for each sample. B) CD spectrum of 12 μM I24D-ΔMTS in the absence (blue) and presence (green) of 0.5 mg/ml SUVs made from *E. coli* lipids.

The enhanced solubility of this mutant made it possible to acquire a ^{1}H-^{15}N HSQC spectrum of I24D ΔMTS and compare it with that of wild-type ΔMTS (Fig. 3.6A). The dramatic difference between these two spectra indicates a significant structural difference from the 6-stranded state for I24D ΔMTS. Broadening was observed for many peaks, with some apparently being broadened beyond detection because only about 65% of the expected backbone amide peaks were observed. This suggests the presence of intermediate-timescale dynamics, raising the possibility that this mutant is not stably folded. However, the thermal denaturation of I24D ΔMTS monitored by CD spectroscopy showed a reversible, cooperative loss of secondary structure with increasing temperature (Fig. 3.6B), with a melting point (Tm) of 85.5 ± 0.5 °C (Table 3.3). Although this is lower than the 91 ± 1.5 °C that we also determined for ΔMTS, these data demonstrate that the structure adopted by the I24D-ΔMTS mutant does contain a stable globular fold, with only a small decrease in stability from the wild-type sequence. In addition, size-exclusion chromatography profiles obtained for I24D mutants showed elution volumes that confirmed a dimeric state, although with a slightly larger size that would be consistent with a loss of globular structure for anti- MinCD residues no longer part of the dimeric interface (Fig. 3.5A,inset).

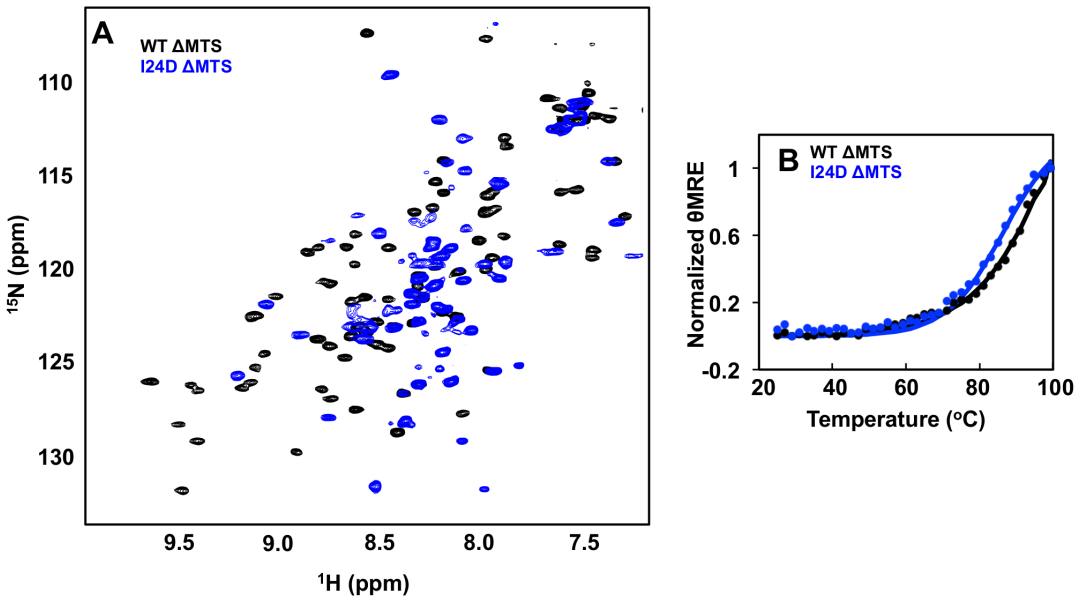

Figure 3.6. Solution NMR and CD thermostability characterization of I24D-ΔMTS *ng*MinE. A) ^{1}H-^{15}N HSQC spectrum of WT (black) or I24D-ΔMTS (blue) *ng*MinE. B) thermostability of *ng*MinE monitored by CD for ΔMTS (black) or I24D-ΔMTS (blue).

Table 3.3. Melting temperatures of *ng*MinE measured by CD spectroscopy

Sample	Tm (°C)	Tm (°C) in 2 M urea	Tm (°C) in 4 M urea
ΔMTS	92 ± 2	73 ± 0.1	61 ± 1
I24D-ΔMTS	85.5 ± 0.5	66.0 ± 0.8	57 ± 0.5
I25R -ΔMTS	92.0 ± 0.8	80 ± 2	61 ± 1
TSD	83 ± 1	ND	ND

Whereas the severity of peak broadening precluded the assignment of chemical shifts that would be required for structure determination of I24D ΔMTS, additional evidence that I24D has adopted the 4-stranded state was also provided by NMR spectra of the topological specificity domain (TSD), composed of residues 31–89 (Fig. 3.7A), previously shown to be a dimer with a 4-strand β-sheet for the *E. coli* homologue. The overall appearance of the TSD spectrum was highly similar to that of I24D ΔMTS, with most of the broad peaks being almost superimposable with those of the TSD. The subset of higher intensity peaks in the central region of the spectrum that would probably correspond to unstructured regions are missing from the TSD spectrum, as would be expected due to the absence of anti-MinCD residues. In addition, reversible thermal denaturation yielded a melting point that was within 2 °C of that determined for I24D

ΔMTS (83 ± 1 °C) as shown in Fig 3.7C and Table 3.3. In addition, CD spectroscopy and size-exclusion chromatography showed strong similarities between I24D ΔMTS and the TSD (Fig 3.7B). These similarities in structure and stability between I24D ΔMTS and the TSD confirm that the I24D mutation has generated a 4 β–stranded state similar to that seen in the crystal structure of the truncated I24N *ec*MinE in complex with *ec*MinD[77].

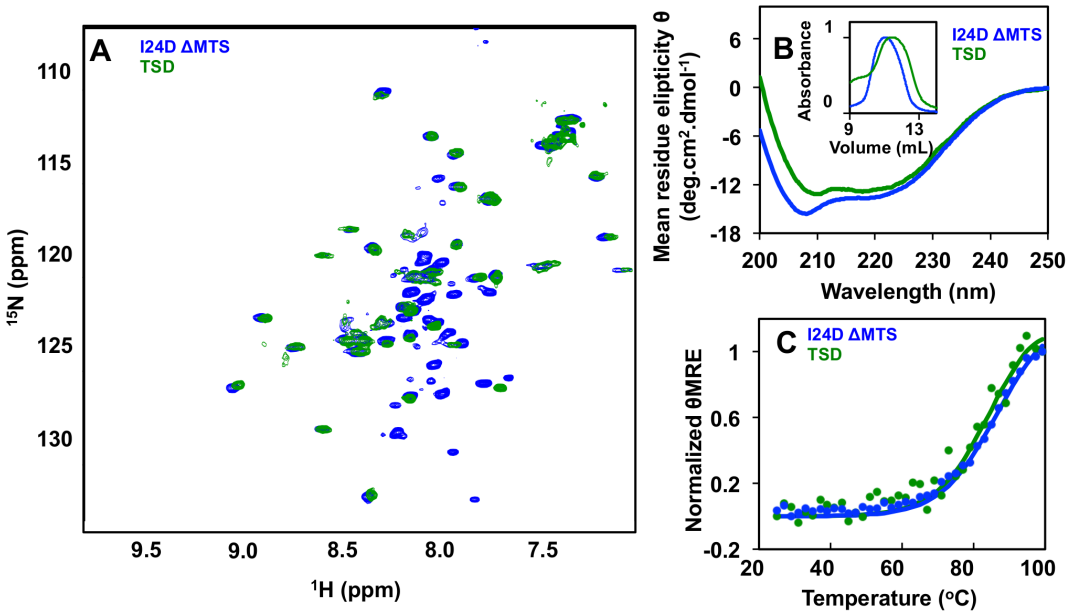

Figure 3.7. Structural characterization of TSD *ng*MinE using solution NMR and CD. A) ^{1}H-^{15}N HSQC spectrum of TSD *ng*MinE (green) superimposed on the I24D ΔMTS *ng*MinE spectrum (blue). B) CD spectrum of the *ng*MinE TSD (green) and I24D ΔMTS mutant (blue). The insets show size exclusion chromatography profiles that confirm a dimeric state for each sample. C) Thermal denaturation curves of the TSD (green) superimposed on that of I24D ΔMTS (blue) as monitored by CD spectroscopy.

3.2.3: Role of the 6- to 4-β–Stranded Conformational Change in Min Activity

The ability of the I24D mutation to trap *ng*MinE in the 4-β–stranded conformation provided a useful tool to evaluate the role of conformational change in the stimulation of MinD ATPase activity. This was tested with I24D ΔMTS, which we confirmed to be unable to bind to membranes by CD spectroscopy (Fig 3.5B). Stimulation of ATP hydrolysis rates for this mutant was virtually indistinguishable from that obtained with ΔMTS (Fig. 3.8B), suggesting that the conformational transition between 6- and 4-stranded states is rapid relative to the rate of the overall cycle.

Curiously, when the same mutation was tested for *ng*MinD activation in the context of full-length *ng*MinE, the maximal rate was not restored to the lower wild-type levels but was the same as that seen for both the WT and I24D ΔMTS mutants (Fig. 3.8A). Therefore, the rate-reducing effect of the MTS does not seem to play a role in MinD activation by this 4-β–stranded state.

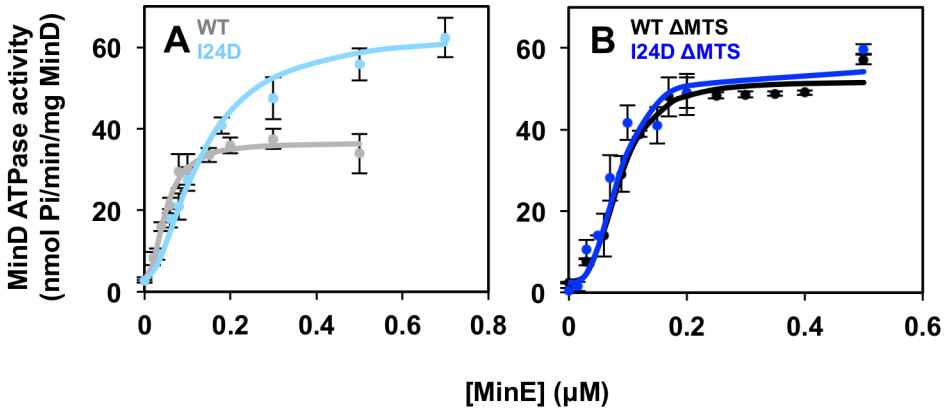

Figure 3.8. Stimulation of *ng*MinD ATPase activity in 4-β–stranded *ng*MinE. Initial rates of ATP hydrolysis are plotted as a function of *ng*MinE concentration for full-length (A) and ΔMTS (B) WT (gray and black) and I24D (light blue and dark blue) *ng*MinE sequences.

3.2.4: I25R unmasks the MTS

As mentioned in introduction, NMR studies suggest that a small population of the MTS amphipathic helix dissociates from the β-sheet of MinE[43]. As indicated earlier, this would be expected to facilitate the interaction of the MTS with the membrane by exposing the hydrophobic face that is normally buried by interactions with the β-sheet in the closed structure. To establish the functional implications of this conformational equilibrium involving the MTS, an arginine residue was introduced at Ile-25 (I25R), which should disrupt the interaction between MTS and the β-sheet to shift the equilibrium and favor a more open intermediate state that exposes the MTS to the solvent while preserving the 6-stranded structure.

As had previously been observed for the analogous mutant made in *ec*MinE[71,77], the solubility of I25R was much lower than that of the WT protein, possibly due to an increase in solvent-exposed hydrophobic surface area caused by MTS dissociation.

Although it was necessary to purify this mutant under denaturing conditions and go through a final refolding step to obtain sufficient amounts for characterization, CD spectra acquired on refolded I25R show that its secondary structure content is very similar to that of the WT protein (Fig. 3.9A and Table 3.1), consistent with the preservation of the 6-stranded state. The ability of I25R to stimulate ATP hydrolysis by MinD was significantly different from WT MinE, with a ~2-fold increase in the amount of MinE required to reach half-maximal activity (Fig. 3.9B and Table 3.2). This reflects the disruptive effect of the arginine in the MinD interaction, because residue 25 comprises a central part of the interface between MinE and MinD. Despite this lower-affinity interaction, it was still possible to achieve a maximal ATPase activity that was larger than the WT maximum.

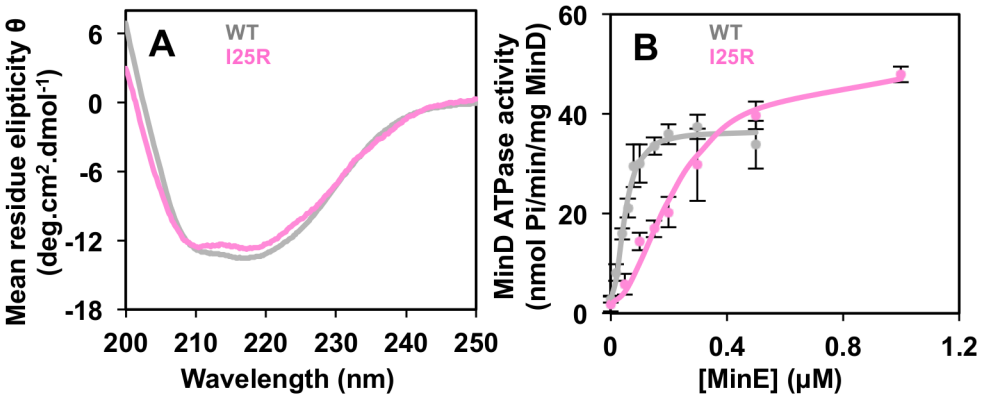

Figure 3.9. Characterization of conformation and function for full length I25R ngMinE. A) CD spectra of full-length I25R ngMinE (pink) and full length WT *ng*MinE (grey). B) rates of ngMinD ATPase activity stimulated by full-length WT (gray) or I25R MinE (pink).

3.2.5: A Critical Role for Ile-25 in the Stimulation of MinD Activity

The fact that I25R did not reach maximum stimulation levels seen for ΔMTS mutants suggests that it should be possible to further increase the activity of this mutant by removing its MTS. As shown in Fig. 3.10A, the CD spectrum of I25R ΔMTS is virtually superimposable with that of WT ΔMTS confirming minimal structural perturbation from the I25R mutation. As expected, the I25R ΔMTS construct was unable to bind to membranes as demonstrated by the absence of a change in its CD spectrum upon addition of lipid vesicles (Fig. 3.10B). However, when the ability of this mutant to

stimulate *ng*MinD-catalyzed ATP hydrolysis was tested, no activity was observed (Fig.3.10C). Even when excess I25R ΔMTS was used (i.e. 40-fold higher than the concentration required to obtain maximal stimulation with full-length I25R), no ATP hydrolysis could be detected.

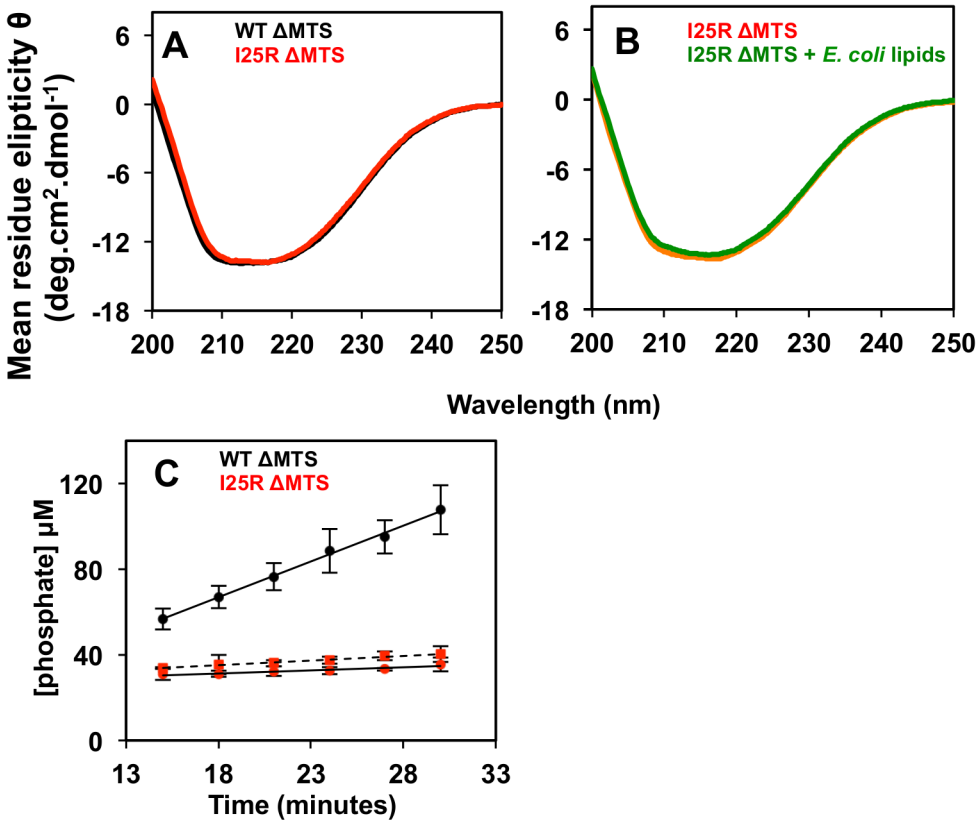

Figure 3.10. Characterization of conformation and function for I25R ΔMTS *ng*MinE. A) CD spectra of I25R-ΔMTS (red) superimposed on WT ΔMTS (black). B) CD spectrum of 12 μM I25R-ΔMTS in the absence (red) and presence (green) of 0.5 mg/ml SUVs made from *E. coli* lipids. C) ATP reaction profiles for *ng*MinD stimulated by I25R-ΔMTS *ng*MinE (0.3 μM (circles) and 40 μM (squares)) with WT ΔMTS (black) or I25R ΔMTS (red) sequences, acquired by monitoring phosphate concentration over time.

Although the CD data provide strong evidence that the structure of this inactive mutant is the same as that of the WT ΔMTS, given its surprising inability to activate MinD, we sought to characterize its structure at higher resolution using solution NMR. As shown in Fig.3.11A, the ^{1}H-^{15}N HSQC spectrum shows a high degree of similarity between WT and I25R ΔMTS spectra. Backbone chemical shift assignments

demonstrated that the largest chemical shift changes were in the local vicinity of the mutation site, as expected (Fig. 3.11B and 3.11C).

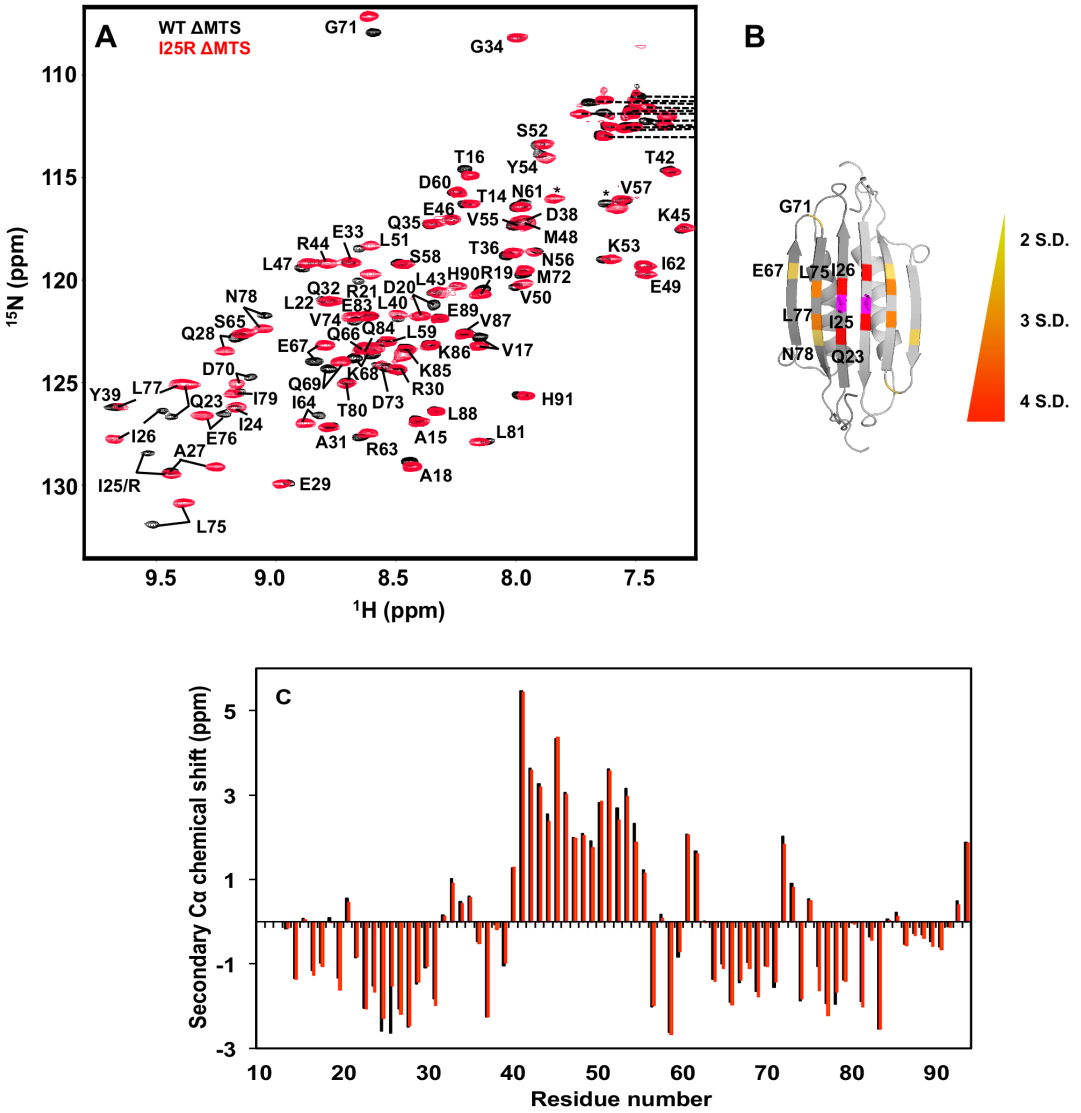

Figure 3.11. Solution NMR confirms a 6-β–stranded structure for_I25R ΔMTS. A) Assigned ^{1}H-^{15}NHSQC spectra of WT-ΔMTS (black) and I25R-ΔMTS (red). B) Average amide chemical shift differences between WT and I25R ΔMTS mapped onto the solution NMR structure. Note that residues comprising the MTS have been removed from the structure for the purpose of clarity. Residues showing average amide chemical shift differences that are greater than the average difference plus 2, 3, and 4 standard deviation values from the mean (S.D.) are colored in yellow, orange, and red, respectively. The mutation site (Ile-25) is highlighted in magenta. C) Secondary Cα chemical shifts of WT-ΔMTS and I25R- ΔMTS confirming that the secondary structure is identical between the two constructs.

Moreover, thermal denaturation experiments on I25R ΔMTS showed a reversible melting curve that is highly similar to that of the WT ΔMTS (Fig. 3.12A), indicating that the introduction of this mutation has not altered the stability of the dimeric structure. This similarity was preserved when the same experiments were done in the presence of low concentrations of urea to allow observation of the full thermal transition, with I25R ΔMTS showing a slightly higher resistance to thermal denaturation relative to ΔMTS (Fig. 3.12B). Collectively, these data demonstrate that I25R ΔMTS is stably folded in the 6-stranded conformation, suggesting a critical role for Ile-25 in the MinD catalyzed conformational transition from the 6-stranded to the 4-stranded state required for MinD activation.

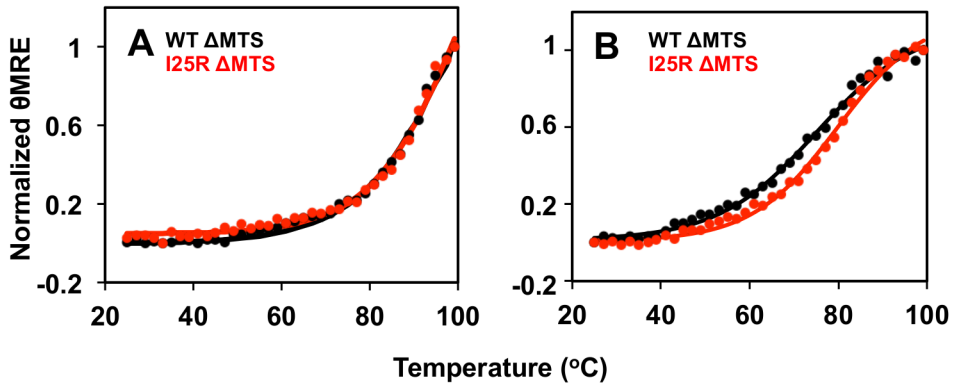

Figure 3.12. Thermostability I25R ΔMTS by CD spectroscopy. A) Thermal denaturation curves of 12 μM of I25R ΔMTS *ng*MinE (red) superimposed on the WT ΔMTS *ng*MinE (black) as monitored by CD spectroscopy. B) In presence of 2 M urea.

3.2.6: Investigation of the Oligomerization State of I25R ΔMTS

The inability of I25R ΔMTS to stimulate MinD ATP hydrolysis raises the possibility this construct may be forming an inactive oligomeric state. At high protein concentrations required for the biophysical studies performed in this chapter, I25R ΔMTS is similar to WT ΔMTS. However, at lower concentrations is it possible that I25R ΔMTS may dissociate into a monomeric state, and this state may be inactive. To test this hypothesis, I25R ΔMTS structure and oligomeric state were examined using the lowest detectable protein concentrations in CD, NMR and size exclusion chromatography

experiments. As shown in Fig. 3.13, for all experiments, the structure and oligomerization states showed no change upon dilution, indicating that I25R ΔMTS remains dimeric at low protein concentrations.

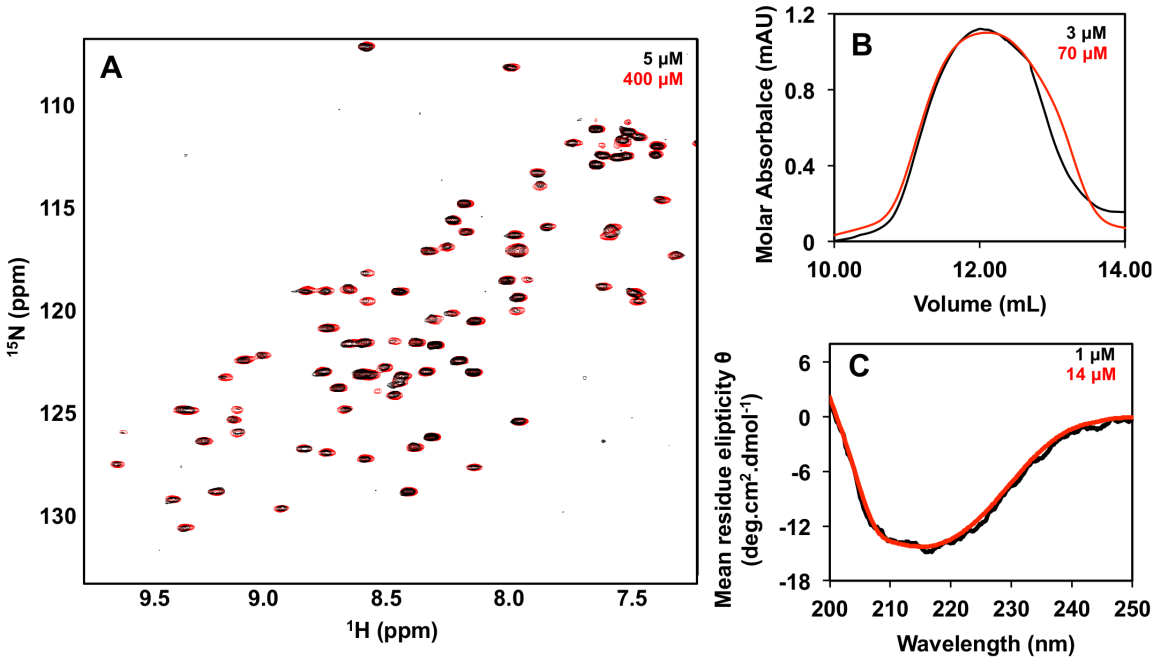

Figure 3.13. Evaluation of the oligomeric state of I25R ΔMTS *ng*MinE. A) ^{1}H-^{15}N HSQC spectra of 5 μM (black) and 400 μM (red) I25R ΔMTS *ng*MinE. B) size-exclusion chromotagraphy of 3 μM (black) and 70 μM (red) I25R ΔMTS. C) CD spectra of 1 μM (black) and 14 μM (red) I25R ΔMTS.

While these studies were performed at the lowest possible concentrations (~1- to 5 μM), the apparent affinity of MinE to bind to MinD is of 0.1 to 0.3 μM. To examine whether the MinE monomer is able to stimulate MinD ATP hydrolysis with a profile that is similar to that of the MinE dimer, a peptide comprised of MinE residues 12-30 was used in the MinD ATP hydrolysis assay. As shown in Fig. 3.14, this peptide was able to stimulate MinD ATP hydrolysis to similar levels found in other ΔMTS constructs.

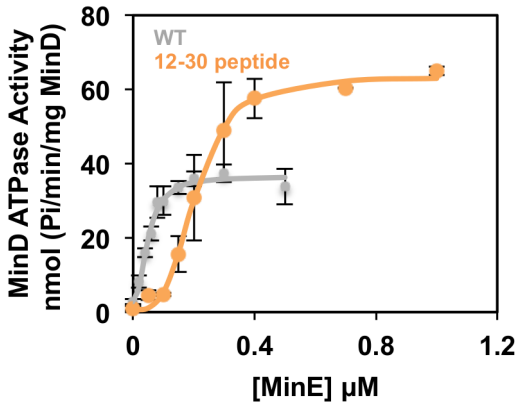

Figure 3.14. Stimulation of MinD ATPase activity by *ng*MinE peptide 12-30 (orange) compared to WT *ng*MinE (grey).

3.3: Discussion

3.3.1: MinD Binding is Sufficient to Trigger Conformational Change in MinE

The ability of MinE to bind lipid membranes has raised questions about the role of this interaction in the Min protein oscillation cycle. In particular, membrane binding could facilitate the structural transition from the closed 6-β–stranded state to the 4-β–stranded state seen in complex with MinD. Indeed, under conditions that shift the equilibrium toward the membrane- bound state (i.e. at high lipid concentrations), our CD spectra do reveal a structural transition in *ng*MinE with secondary structure content that is consistent with a 4-stranded state. However, when expressed in *E. coli* in the absence of MinD, WT *ec*MinE does not localize to the membrane[49,71,118,119], although membrane localization is observed if mutations are introduced that promote exposure of the hydrophobic face of the MTS helix[71,77]. These include mutations that would be expected to destabilize the 6-stranded state (e.g. L22S and I24N) and the I25R mutation that promotes dissociation of the MTS while retaining the 6-stranded state. Therefore, the inherent membrane-binding ability of MinE is not significant until the conformational transition that unmasks the membrane-binding surface of the MTS has occurred. Because MinE stimulation of MinD activity does not require MinE–membrane interactions, MinE binding to MinD appears to be sufficient to stimulate this structural transition, which would then prime MinE for binding to the membrane.

One of the implications of MinD activation by MinE constructs lacking the MTS is that the binding energy of the MinE-MinD interaction alone appears to be sufficient to stimulate the transition from the 6-β–stranded to 4-β–stranded state. This suggests that there are an adequate number of solvent-exposed residues that can initially bind to MinD to trigger this conformational change. As shown in Fig. 3.15, residues from MinE that form the lower half of the MinD-binding helix in the complex (specifically residues 14–21) are not in the dimeric interface, but in loops that are relatively solvent-accessible in the 6-stranded state. Amide proton exchange kinetics measured for *ng*MinE[43] and *ec*MinE[80] show some protection for these residues, suggesting that these residues are less accessible in the closed 6-β-stranded state but would become more accessible when the MTS dissociates from the central β-strand. This raises the possibility that MinE first interacts with MinD via an encounter complex involving these residues and that this would facilitate the structural transition that gives rise to the more extensive interaction surface. Ile-25 appears to play a role in the formation of this encounter complex, because its mutation to arginine rendered the ΔMTS construct inactive. However, the full-length variant of I25R was able to stimulate *ng*MinD ATP hydrolysis, suggesting that membrane binding can overcome this barrier to the conformational transition. Therefore, it appears that interactions with both MinD and the membrane are involved in the rapid conversion of MinE from its closed 6-stranded structure to its MinD-bound 4-stranded state, and this occurs through the formation of an encounter complex that retains some characteristics of the MinE-MinD complex captured in the X-ray crystal structure.

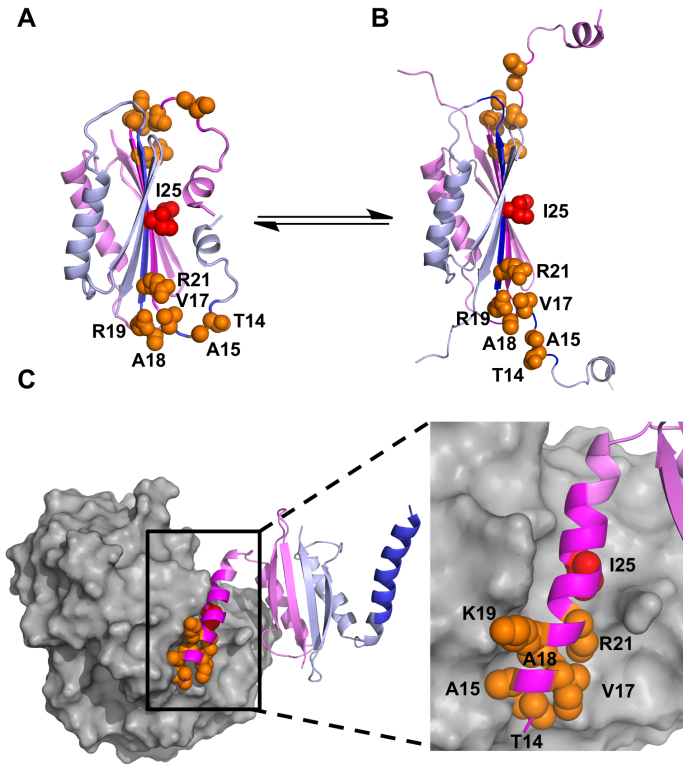

Figure 3.15. MinD binding initiated by interactions with solvent-accessible residues. Side chains of residues proposed to be important for forming the encounter complex are highlighted on the solution NMR structure of *ng*MinE (A), a model of this structure that is transiently sampled as suggested by NMR spin relaxation studies[43] (B), and the structure of ecMinE I24N missing residues 1–12 bound to *ec*MinD (C). The side chain of Ile-25 that is required for membrane-independent stimulation of MinD is highlighted in red for all structures.

3.3.2: Retention of MinE on the Membrane After ATP Hydrolysis

Our measurements of the maximal ATPase activity that can be stimulated by *ng*MinE and its ΔMTS mutant show that the MTS actually reduces the maximal rate of ATP hydrolysis. To understand the origin of the MTS-mediated reduction in ATPase activity, it is necessary to recall that, as with any steady-state kinetic measurement, the rate of the slowest step in the reaction cycle gives rise to the observed rate, although this may not be the step that generates the read-out of the assay (e.g. the generation of free phosphate). In the case of the Min cycle, there are multiple steps involved in MinE-stimulated ATP hydrolysis by MinD, including nucleotide exchange, protein-protein

interactions, and protein-membrane interactions. Our observation that the presence of the *ng*MinE MTS slows down the maximal hydrolysis rate raises the possibility that membrane dissociation of MinE is the rate-limiting step in the reaction cycle. Although it had previously been suggested that ATP hydrolysis is the slowest step in this cycle[72,120], this was based on the observation that it is possible to isolate membrane-bound *ec*MinE and *ec*MinD when ATP is present. However, the same result would also be expected if Min protein dissociation from the membrane, instead of ATP hydrolysis, is rate-determining. It has also been suggested that the interaction between the MTS and the central MinE β-sheet is inhibitory to MinD binding[80]. However, this is not likely to be a rate-determining step in the cycle, because NMR dynamics measurements for *ng*MinE suggest that conformational exchange is fast relative to the Min interaction/ATPase cycle (i.e. millisecond versus tens of seconds)[43]. Moreover, amide solvent deuterium exchange for MinD-binding residues in solvent-accessible regions of *ec*MinE is close to complete within 15 s[80], suggesting that the MTS-dissociated state was frequently sampled over this time. This suggests that MTS dissociation is at least 1 order of magnitude faster than the ~1-min turnover times measured for *ng*MinE.

The rate-reducing effect of MinE–membrane interactions on the Min cycle has also been mirrored in fluorescence imaging performed on labeled *ec*Min proteins on planar lipid bilayers. These studies show concentration gradients of Min proteins that migrate across the surface, with pattern shapes and sizes being determined by a number of factors, including membrane composition, protein concentration, and compartmentalization[52–56,121–123]. A common feature in many of these dynamic patterns is a concentration gradient of MinD that forms a wave, accompanied by a wave of MinE with maximum intensity that peaks just after the trailing edge of the MinD wave. These fluorescence profiles show that MinE is left behind on the membrane after dissociation of MinD before it undergoes dissociation itself, as would be expected if MinE release from the membrane is rate-determining. In addition, the velocity of wave propagation and the dimensions of the wave are determined in part by the ratio of Min proteins used, with faster propagation being accompanied by a decrease in period, indicating a faster cycle of Min proteins on and off the membrane[52,55]. Because increasing ratios of MinE to MinD also increase ATP hydrolysis rates[42,43,60], this suggests that the rate of the ATP hydrolysis

cycle determines the scale and dynamics of long-range ordering by Min proteins. It has been shown in similar experiments that the effect of removing the MTS from *ec*MinE gives rise to faster propagation rates and smaller periods[54], in line with the faster ATP hydrolysis rates, we measured for ΔMTS. As expected, ΔMTS dissociation from the membrane was in sync with MinD dissociation, with no propensity to remain on the membrane after MinD release from the membrane. Intriguingly, the types of patterns that could be formed by this mutant were different from those seen with full-length *ec*MinE, indicating that in addition to modulating the rate of ATP hydrolysis, membrane binding is also crucial for normal pattern formation on bilayers and E-ring formation *in vivo*.

3.3.4: Implications of Slow MinE Membrane Dissociation

Several models of the Min protein interaction/ATPase cycle have been proposed that seek to provide a molecular description of Min protein binding and dissociation from the membrane and its link to ATP hydrolysis by MinD. One of the most prominent of these is known as the "Tarzan of the jungle" model, which provides the foundation for a number of updated models that were subsequently proposed to incorporate new data[54,80,124–126]. According to this model, MinE is able to remain in a membrane-bound state after its first encounter with MinD, where it can stimulate additional cycles of ATP hydrolysis before membrane dissociation. However, this is difficult to reconcile with the faster hydrolysis rates stimulated by ΔMTS, because this mutant is unable to adopt this membrane-bound state. Even the peptide bearing the MinD-interaction domain alone (residues 12–30) promoted a higher level of activity than the wild-type MinE (Table 3.2). Moreover, the cooperativity of ATP hydrolysis was similar for WT and ΔMTS *ng*MinE, which would not be expected if MinE could more effectively activate MinD while bound to the membrane. Taken together, the kinetics of *ng*MinD-catalyzed ATP hydrolysis suggests that *ng*MinE remains bound to the membrane after simulating ATP hydrolysis, but in contrast with previous models of MinD activation, membrane-bound MinE does not stimulate other ATP-bound MinD dimers that may also be on the membrane.

The reason for the inactivity of the MinE membrane-bound state following release from MinD is not clear; however, local accumulation of MinE on the membrane raises

the possibility of higher-order self-association that could be inhibitory to MinD interactions. It has been shown that oligomers with fibril-like properties can be formed on supported bilayers by either full-length *ec*MinE or a peptide containing the first 31 residues from the N-terminal side of *ec*MinE (*ec*MinE (1–31)), with residues 19–29 being proposed to form intermolecular β-strand interactions[116]. This would position key MinD-binding residues on opposite sides of the β-strand, preventing its interaction with MinD. Interestingly, the I24N mutant of *ec*MinE (1–31) did not show this propensity for fibril formation[116], which might indicate that the increased rates observed for full-length I24D reflect this decreased ability to form fibrils and not the effect of fixing the MinE conformation in its 4-stranded state. In the case of I25R, the capacity for fibril formation by *ec*MinE (1–31) containing this mutation was similar to that of WT *in vitro*; however, no ring structures were observed *in vivo* when full-length I25R *ec*MinE was expressed in *E. coli* with *ec*MinD[116]. This might reflect a reduced capacity for self-association on the membrane, which is consistent with the heightened activity that was seen for this mutant.

3.3.5: An Updated Version of the Min Protein Cycle

It is notable that the maximal rates obtained for the more active mutants appeared to hit a ceiling, beyond which further stimulation was not possible. This is highly suggestive of the possibility that the rate-determining step no longer involves the MinE-MinD interaction, but some other step that is independent of MinE for these mutants. This was substantiated by ATPase activity measurements performed on peptide *ng*MinE 12–30, because they yielded a value for k_{cat} identical to that obtained with ΔMTS (Table 3.2). One candidate for the new rate-determining step is the dissociation of MinD from the membrane, which could become a limiting factor in the cycle when MinE is no longer able to bind the membrane and potentially undergo higher-order self-association. It has been shown that *ec*MinD retains membrane-binding affinity when bound to ADP, albeit with a lower affinity than that seen for ATP-bound *ec*MinD[33]. This raises the possibility that loss of key interactions involving the terminal phosphate moiety of ATP[32] upon its hydrolysis could produce a metastable membrane-bound state that is further stabilized by interactions with membrane-bound MinE. Dissociation of the MinE-MinD complex

would precede release of MinD from the membrane, with MinE being released at a slower rate. Alternatively, nucleotide exchange of ADP-bound MinD with ATP could instead be rate-limiting, a scenario that would help to prevent rapid reassociation with the membrane and allow its diffusion to the other side of the cell. However, turnover times measured for ATP hydrolysis stimulated by ΔMTS suggest that the lifetime of this state is on the order of ~30 s, which is in better agreement with residence times measured for *ec*MinD on planar lipid bilayers[53] compared with the 0.3-s residence time measured for *ec*MinD in the *E. coli* cytoplasm[127]. Whereas measurement of rate constants for these two steps will be required to definitively establish the slower step in the reaction cycle, based on these residence time differences, it seems more likely that MinD dissociation from the membrane comprises the slow step when dissociation of MinE from the membrane is no longer rate-determining.

Our results can be incorporated into an updated version of the Min protein interaction cycle as shown in Fig. 3.16. MinE in the cytoplasm predominantly exists in the closed 6-stranded structure and transiently samples an open state that would enhance the accessibility of loop residues 13–20. In this state, MinE can form an encounter complex with MinD, which triggers the conformational change to expose the remainder of the MinD-binding helix. This stimulates ATP hydrolysis in MinD, with membrane binding by MinE accompanying this conformational transition, anchoring it in a state that is no longer able to stimulate ATP hydrolysis. Although the nature of this inhibited state is not known, it may reflect self-association of MinE dimers via interactions involving MinD-binding residues. MinD may also remain bound to the membrane after ATP hydrolysis but dissociate from the membrane before MinE, allowing it to diffuse to the other side of the cell, where the membrane binding would not be hindered by the presence of membrane-localized MinE. In this updated cycle, there is no requirement for both MinE-binding sites in MinD to be occupied to stimulate ATP hydrolysis as proposed previously[54]. Instead, a single MinE-binding event is sufficient, consistent with previous demonstrations that MinD heterodimers that only bind MinE at one site hydrolyze ATP at both sites[69].

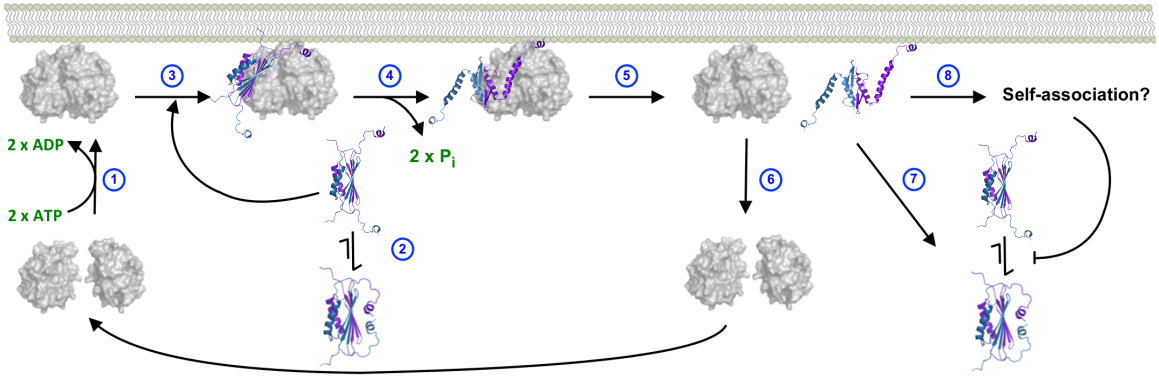

Figure 3.16. Updated model of the Min interaction cycle. ADP-bound MinD (gray surface) forms a dimer when bound to ATP that localizes to the membrane surface[58,128] (1). As suggested by NMR spin relaxation measurements[43], cytoplasmic MinE (ribbon structure) is in equilibrium between a closed state and MTS-exposed state (2). Our work suggests that the MTS-exposed state forms an encounter complex with MinD (3) that triggers the conformational change into the 4-β–stranded open state that binds the membrane while stimulating ATP hydrolysis by MinD (4). Dissociation of the MinDE complex (5) is followed by MinD dissociation from the membrane (6), whereas MinE can also dissociate from the membrane (7) or remain associated with the membrane (8) in a state that inhibits MinD binding and slows membrane dissociation (as shown in the ATP hydrolysis rate measurements in this work), potentially via the self-association of MinE that has been described previously[116].

3.3.6: *N. gonnorhoeae* Min Proteins Reveal Conserved Properties of the Min Cycle

Although much of our understanding on the Min system has been derived from studies with *E. coli* proteins, we have focused on homologues from the coccus *N. gonorrhoeae*, a sexually transmitted human pathogen that is gaining resistance to an increasing number of antibiotics[129]. Despite the fact that cell division in cocci occurs along alternating perpendicular planes to create a tetrad of daughter cells[27], the *ng*Min protein system plays a similar role in the maintenance of normal cell division, morphology, and virulence as it does in *E. coli*[12,28,130]. Moreover, there is strong conservation of function between these two homologues, with *ng*Min proteins oscillating from pole to pole when expressed in *E. coli*, either together or with the complementary *ec*Min protein[28]. Overexpression of *ng*Min proteins in *E. coli* also induced the same irregularities in morphology as seen with *ec*Min proteins[12,13]. In addition, MinD-catalyzed MinE-stimulated ATP hydrolysis rates on membranes made from *E. coli* extracts measured for *ng*Min proteins in this work are very similar to those measured

using *ec*Min proteins[42]. Although the lipid mixture used in our experiments was derived from *E. coli*, membranes from both species are primarily composed of ~ 70 mol % phosphatidylethanolamine, with ~ 20 mol % being the anionic lipid phosphatidylglycerol[131,132]. The main difference is that the cardiolipin fraction is much smaller in *N. gonnorhoeae* ~1 mol % versus ~ 5 mol % for *E. coli*), giving rise to a lower charge density predicted for the membrane surface of *N. gonorrhoeae*. Nonetheless, pattern formation by *ec*Min proteins on planar lipid bilayers was found to occur over a range of lipid headgroup compositions[52], suggesting that the *E. coli* lipids serve as a reasonable substitute for those from *N. gonnorhoeae*. More importantly, the role of the MinE MTS in the Min cycle, as elucidated from our work on *ng*Min proteins, should have implications for Min protein cycles in general, including those linked to the pathogenicity of *Francisella tularensis*[133,134] and enterohemorrhagic *E. coli*[135] as well as the diverse range of eukaryotic species that are predicted to use mitochondrial and plastid Min proteins[136,137].

Chapter 4

Probing MinE Conformational Change Using Solution NMR

4.1: Introduction

As demonstrated in the previous chapter, MinE undergoes a conformational change upon membrane interaction. This membrane-induced conformational change in MinE is expected to expose the anti-MinCD domain to catalyze formation of the structure seen in the complex formed between MinD and MinE. To gain structural insights on how these interactions induce MinE conformational change, various attempts were made in the Goto lab to capture MinE alone in an open state in the presence of phospholipids or detergents by solution NMR[138]. However, this proved to be difficult, since poor NMR spectral quality and sample solubility resulted from exposure of MinE to these conditions. My subsequent results with ΔMTS stimulation of MinD ATP hydrolysis activity suggested that ΔMTS could undergo conformational change independent of membrane binding in order to expose the antiMinCD domain for MinD interaction. This suggests that MinD is capable of inducing conformational change in MinE, although the mechanism by which this change is induced remains unclear. Thus, we were interested in probing the ability of MinD interactions with MinE to induce its conformational change. In order to do so, I employed solution NMR to characterize MinE structure under a range of conditions. Results from this chapter suggest that conserved loop residues between the MTS and first β-strand of MinE may interact first with MinD before conformational change is induced. In addition, changes in MinE ΔMTS NMR spectra suggest that this interaction with MinD may occur even in the absence of phospholipid. However under conditions where MinE binding is saturated by MinD NMR spectral quality was poor, potentially indicating that complex size was too large to allow high resolution characterization by standard solution NMR approaches. Overall, these results will help to guide efforts to characterize the MinD-MinE complex by solution NMR in the future.

4.2: Results

4.2.1: Solution NMR of MinE in the Presence of Membrane-bound MinD

To probe MinD-induced MinE conformational change, the effect of MinD on the NMR spectrum of WT ΔMTS MinE was monitored by solution NMR under assay conditions. In the first experiments, ΔMTS MinE was incubated with ATP-bound MinD at a ratio of 1:10 with SUVs made from *E. coli* lipids. In general the spectrum was almost identical to that obtained in the absence of lipids and MinD.

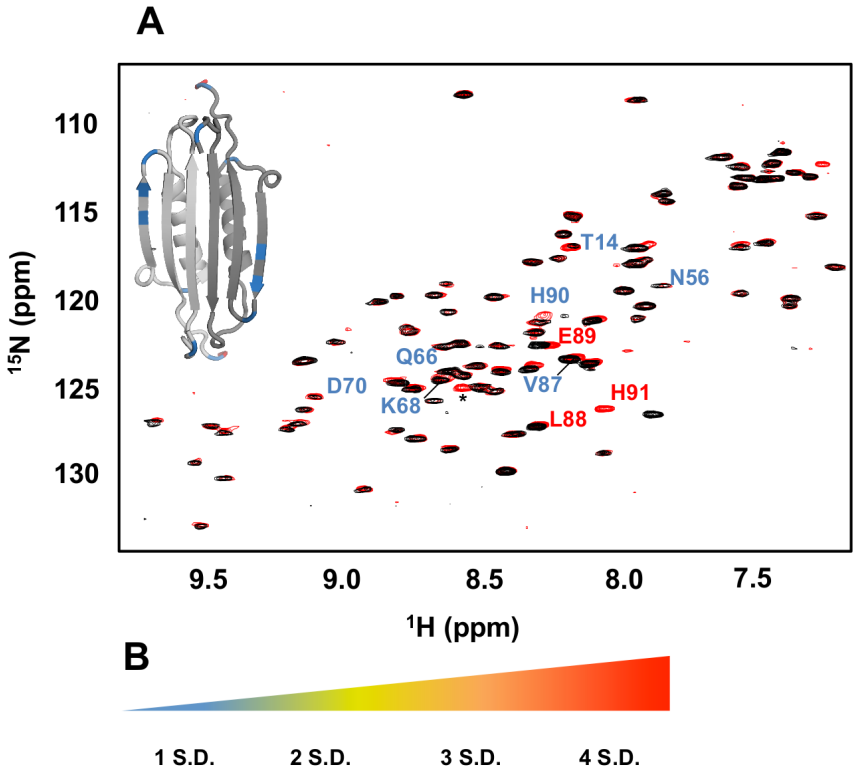

Figure 4.1. ^{1}H-^{15}N HSQC spectrum of WT ΔMTS in MinD ATPase reaction conditions. 20 μM of MinE WT ΔMTS in the absence (black) and in presence (red) of 2 μM MinD, 1 mM ATP, 1 mM $MgCl_2$ and 0.5 mg/ml SUVs made from *E. coli* lipids. Both spectra were obtained at pH 7.2, 25°C. Residues with an average amide chemical shift or intensity difference greater than the average by one standard deviation (S.D.) or more are highlighted in the structure of *ng*MinE (inset) with the MTS removed for clarity (PBD code 2KXO), following the colour scheme in B.

However, a small number of residues showed small chemical shift differences that were mainly located at the C-terminus. In addition, small changes in intensity were seen for polar surface exposed residues on the β-sheet, namely Asn56, Gln66 and Lys68. Also some peaks such as Thr14 and Asp70 showed an increase in intensity suggesting a decrease in pH as result of MinE-stimulated MinD ATP hydrolysis.

Due to low concentration of ΔMTS used (~20 μM), it was necessary to acquire the spectrum in a period of 2.5 hours to ensure adequate signal-to-noise could be obtained. However, according to our MinD ATPase measurements, a significant proportion of ATP was likely hydrolyzed, which would be expected to reduce the amount of ATP available, and simultaneously decrease the pH of the solution. One way to reduce the NMR acquisition time is to use a higher concentration of MinE.

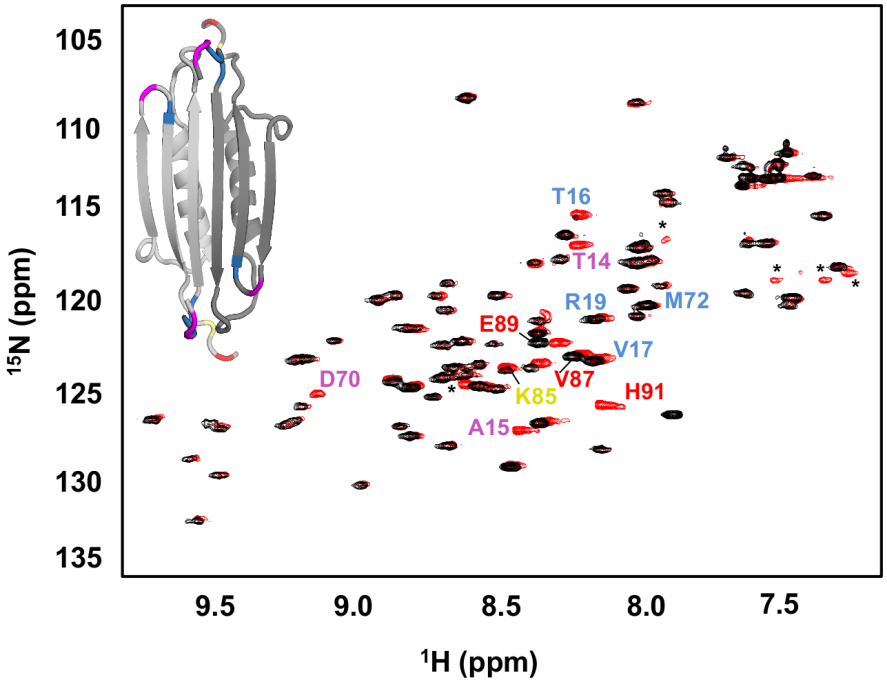

Figure 4.2. Impact of MinD reaction conditions on a higher concentration MinE sample. HSQC spectrum of 200 μM ΔMTS MinE in the absence (black) and presence of 6 μM MinD, 1 mM ATP, 1 mM $MgCl_2$ and 0.5 mg/ml SUVs made from *E. coli* lipids. Residues showing significant changes in chemical shift or intensity are shown on the inset structure following the color scheme shown in Figure 4.1. Assigned peaks that are only visible under reaction conditions are highlighted in magenta. New unassigned peaks that appear in the reaction spectrum are indicated with asterisks.

As shown in Fig 4.2, slightly larger changes in amide chemical shifts and peak intensities were observed. In this spectrum, changes were not only observed at the C-terminal end, but also residues at the N terminus, with Thr14 and Ala15 peak intensities increasing while Thr16 and Arg19 peaks were broadened. These observations suggest that the mobility is altered under these conditions, potentially through an interaction with MinD.

To verify that MinE is active under these NMR conditions, the MinD ATPase reaction assay was performed (Fig 4.3) and showed that ΔMTS was able to stimulate MinD ATPase hydrolysis to a rate that was similar to those measured under our standard assay conditions. Interestingly the concentration of phosphate at the first time point was almost ten times higher with the reaction containing 100 uM ΔMTS. The reason for this is not clear, however, it does suggest that pH changes due to ATP hydrolysis remains a significant factor that may be inducing the changes seen in the NMR spectra. In particular, this would be expected to change the protonation state of the C-terminal His-tag, which would explain the shifts seen at the C-terminus. This may also be the origin of the intensity increase seen for flexible residues, including those close to the N-terminus of the ΔMTS construct.

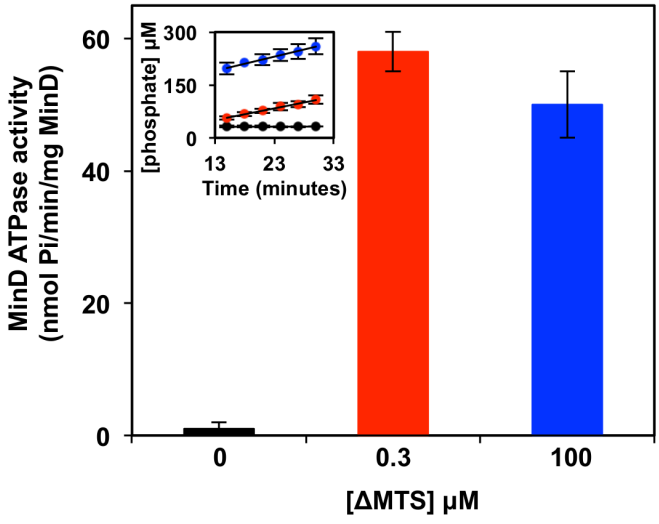

Figure 4.3. MinE-stimulated MinD-catalyzed ATP hydrolysis under NMR conditions. Rates of ATP hydrolysis measured under standard assay reaction conditions without ΔMTS (black) and with 0.3 μM ΔMTS (red), or under NMR conditions (1 mM $MgCl_2$, 1 mM ATP and 0.5 mg/ml SUVs made from *E. coli* lipids in pH 7.2 at room temperature) with 100 μM ΔMTS (blue). Inset shows the rate profiles for each measurement.

To eliminate the potential for changes in pH to influence the NMR spectrum, ΔMTS spectra were also acquired under reaction conditions using the non-hydrolyzable ATP analog ATPγS, since it can be bound by MinD and support MinD interactions with lipids and MinE[31,34,139]. As shown in Fig 4.4, the NMR spectra in the presence and absence of ATPγS under reaction conditions were almost identical, although small changes were found in C-terminal residues, similar to previous experiments. The lack of significant differences in these NMR spectra suggests that the vast majority of MinE does not interact with MinD under these conditions, with potentially only a tiny population of MinE being involved in interaction and conformational dynamics.

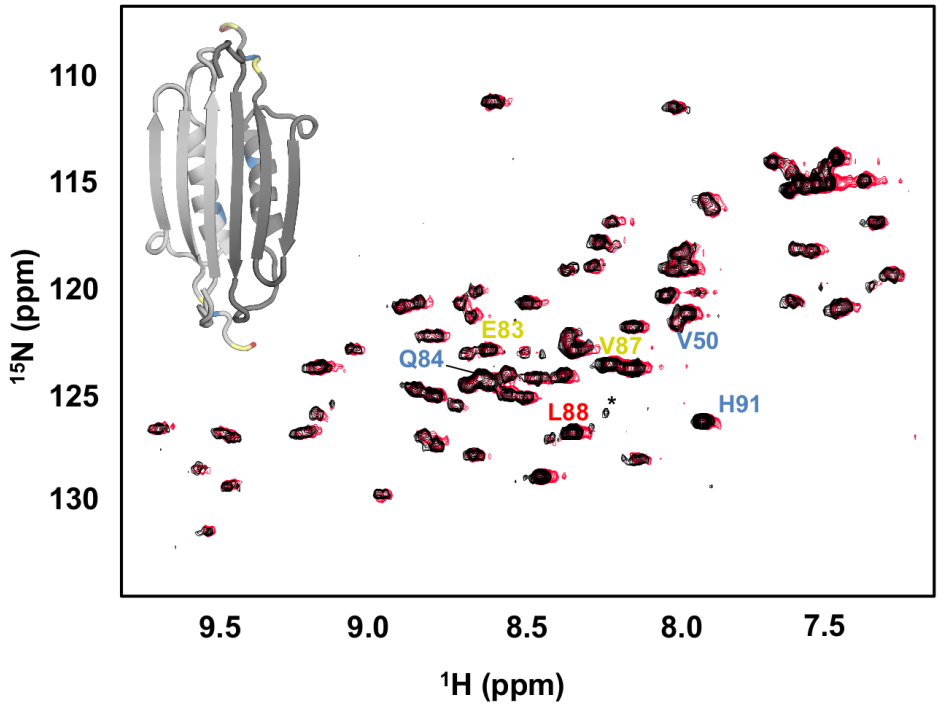

Figure 4.4. Effect of ATPγS on the ΔMTS MinE HSQC spectrum. 95 μM MinE WT ΔMTS in presence of 25 μM MinD, 1 mM $MgCl_2$, and 0.5 mg/ml SUVs made from *E. coli* lipids in the absence (black) and presence of 1 mM ATPγS (red).

Our previous measurements of MinD ATPase activity showed that only 0.1 μM of ΔMTS MinE is required to stimulate ~ 3 μM MinD to half maximal velocity. Under those conditions, only ~ 7% of MinE may be participating in direct interactions with MinD. This raises the possibility that increasing the concentration of MinD may help to increase the fraction of MinE that is bound to MinD. To test this, a spectrum of ΔMTS was

acquired in the presence of an excess of MinD. While no significant change was observed at a 2:1 MinD:MinE ratio, under a 6.5:1 ratio, a subset of residues showed peak broadening of the same N- and C- terminal residues (Fig 4.5) that were also observed in previous conditions (Fig 4.1).

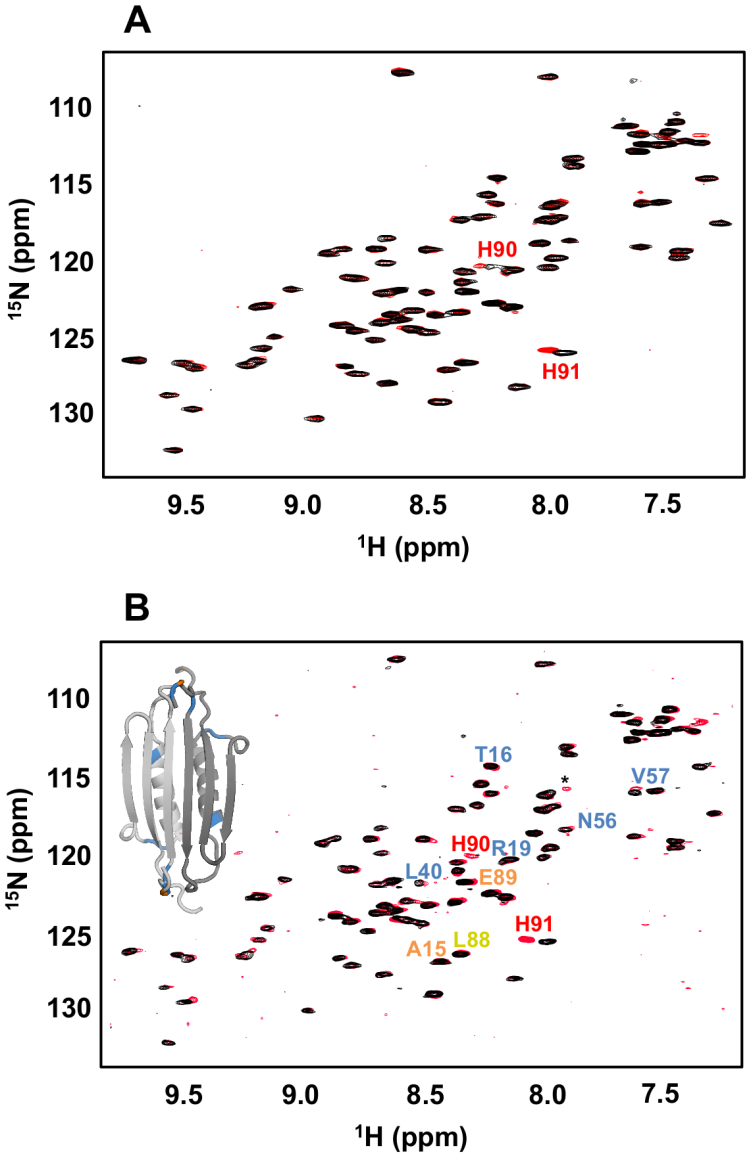

Figure 4.5. Effect of higher MinD concentrations on the MinE ΔMTS spectrum. (A) 20 µM MinE WT ΔMTS in the absence (black) and presence of 40 µM MinD (red). (B) 10 µM MinE WT ΔMTS in the absence (black) and presence of 65 µM MinD (red). In both panels, the samples used to record the red spectrum also contained 1 mM $MgCl_2$, 1 mM ATPγS and 0.5 mg/ml SUVs made from *E. coli* lipids.

4.2.2: Probing MinE Interactions with MinD in the Absence of Lipids

The x-ray structure of the MinD-MinE complex was determined in the absence of phospholipid, although the open state of MinE was induced artificially by the I24N mutation. This raises an interesting question as to whether MinD alone is capable of inducing the MinE conformational change *in vitro*. To address this question, solution NMR was used to probe the interaction between MinE and MinD in the absence of lipids. As shown in Fig 4.6 with a 1:10 MinD to MinE ratio, there were small changes in peak intensities and chemical shifts that followed a pattern that was similar to what was observed previously in Fig 4.1 and 4.5B. Although the changes in previous experiments were proposed to reflect a change in pH as a result of MinD ATP hydrolysis in presence of lipids, these changes also were observed in absence of lipids. These results suggest that these residues may be involved in MinD interactions, even in the absence of lipids.

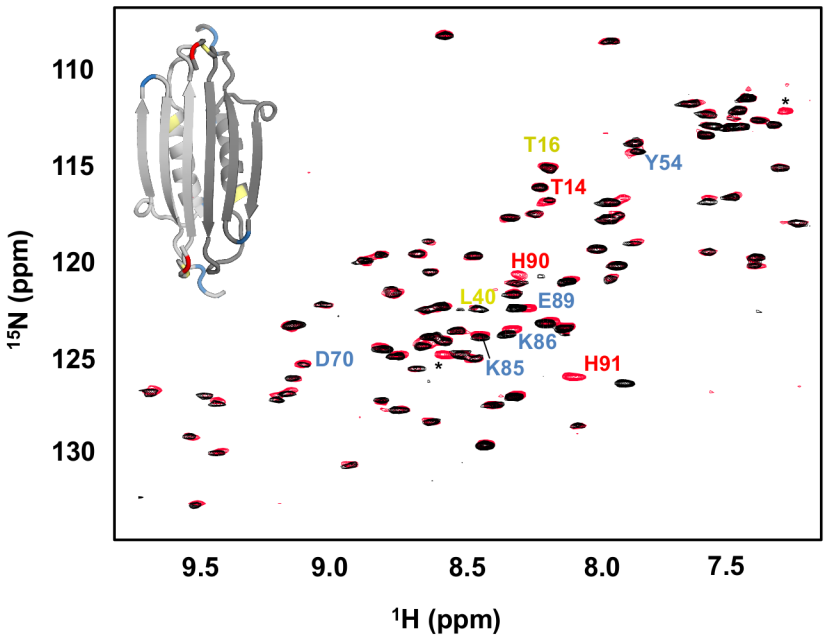

Figure 4.6. WT ΔMTS interactions with MinD probed by solution NMR. 20 μM MinE WT ΔMTS in the absence (black), and presence of 2 μM MinD, 1 mM $MgCl_2$, 1 mM ATP (red).

Similar to Fig 4.5, the relatively small magnitude of changes observed in the previous experiment could be due to the low population of MinE that interacts with MinD at that concentrations that were used. To evaluate this possibility, an NMR spectrum was acquired with a 1:2 ratio of ΔMTS MinE to MinD ratio in presence of ATP. As shown in Figure 4.7A, very few peaks (~15 %) were visible in the HSQC spectrum, with chemical shifts spanning a narrow range of proton chemical shifts that are reminiscent of an unfolded protein. Surprisingly, only residues from N and C termini were visible suggesting that MinD and MinE form a complex that is too large to be seen in conventional solution NMR experiments. However, the sample showed almost immediate signs of precipitation, suggesting that the poor sample quality was due to aggregation. In contrast, when a similar experiment repeated with ATPγS, almost no changes were observed in the spectrum relative to the control (Fig 4.7B). This indicates that MinD bound to ATPγS does not exhibit the same behavior as its ATP-bound state, reducing its utility as a non-hydrolyzable ATP analogue for studying MinD-MinE interactions. This is consistent with previous observations that ATPγS could not be used in place of ATP to induce dimerization and membrane-deforming activity in MinD[72].

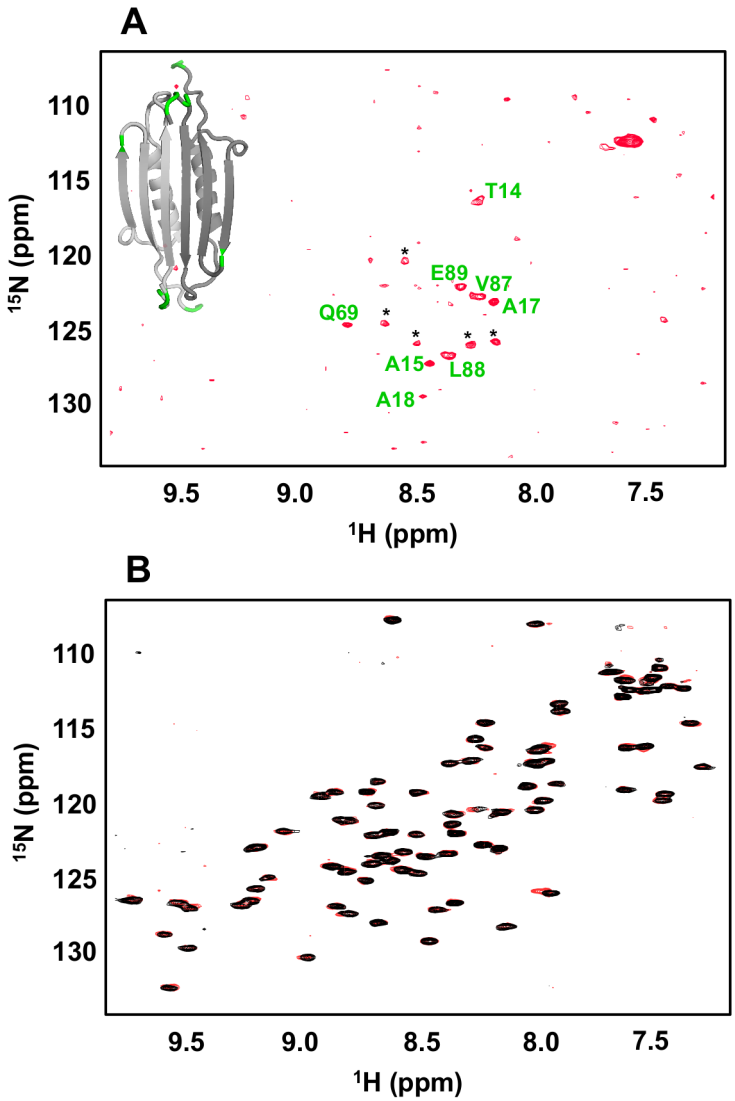

Figure 4.7. Effect of high MinD:MinE ratios on the NMR spectrum of WT ΔMTS MinE. 20 μM MinE ΔMTS in the absence (black) or presence (red) of 40 μM MinD, 1 mM $MgCl_2$ and (A) 1 mM ATP or (B) 1 mM ATPγS. New unassigned peaks that appear in the reaction spectrum are indicated with asterisks while peaks that are visible in both control and reaction spectra are highlighted in green.

Since ATPγS does not seem to be an appropriate substitute for ATP, we decided to try the catalytically deficient MinD mutant D40A to allow study of a complex without the complication of ATP hydrolysis. However, ΔMTS MinE with a 5-fold excess of D40A MinD showed even fewer peaks than seen with the WT MinD (~ 5 peaks from to C terminal residues). Unlike conditions with WT MinD (Fig 4.7), this sample did not show physical signs of aggregation in the form of a precipitate, suggesting that the poor

quality of the spectrum could be due to the formation of a MinD-complex that is too large to detect under the conditions we have used.

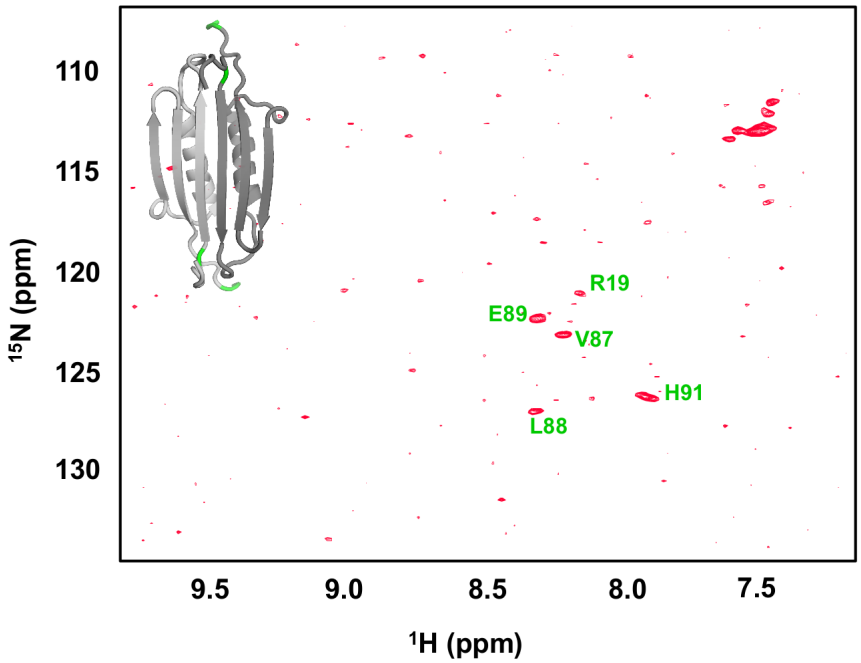

Figure 4.8. HSQC spectrum of WT ΔMTS in the presence of MinD D40A. 10 μM WT ΔMTS MinE in the presence of 50 μM MinD D40A, 1 mM $MgCl_2$, 1 mM ATP. Peaks that are visible in both control and reaction spectra are highlighted in green.

Table 4.1. Summary of NMR experiments used to probe MinE conformational change.

Fig	[ΔMTS] μM	[MinD] μM	NTP	*E. coli* lipids	Shift or intensity changes in C-terminus	Shift or intensity changes in N-terminus	New Peaks?	Lost Peaks?
4.1	20	2	ATP	Y	Y	Y	N	N
4.2	200	6	ATP	Y	Y	Y	Y	N
4.4	95	25	ATPγS	Y	Y	N	Y	N
4.5A	20	40	ATPγS	Y	Y	N	N	N
4.5B	10	65	ATPγS	Y	Y	Y	N	N
4.6	20	2	ATP	N	Y	Y	Y	N
4.7A	20	40	ATP	N	Y	Y	Y	Y
4.7B	20	40	ATPγS	N	N	N	N	N
4.8	10	50**	ATP	N	Y	N	N	Y

*Y indicates yes, N indicates no; **D40A MinD used in place of WT MinD.

4.3: Discussion

As illustrated in the previous Chapter, MinE undergoes a conformational change upon membrane binding, and this change may help expose the antiMinCD domain for interactions with MinD. However, the ability of the ΔMTS mutant to stimulate MinD activity raises questions on the role of MinD in the induction of conformational change in MinE. Our MinD ATPase measurements revealed that MinD is stimulated to similar levels by both the 6- and 4-β sheet structures, as represented by ΔMTS and I24D ΔMTS, respectively. This suggests that interactions with MinD may be sufficient to induce this conformational exchange. As proposed earlier, a subset of MinD-binding residues in MinE, namely residues 14 to 21, are solvent exposed in the 6-β stranded structure. Moreover, the accessibility would be expected to increase if the MTS dissociates from the central β strand, as suggested by solution NMR ^{15}N spin relaxation measurements[43]. This raises the possibility that there is an initial interaction between MinE and MinD that is required to induce the conformational change in MinE. Consistent with this hypothesis, our results showed that chemical shift or intensity changes in this MinE region upon addition of MinD, specifically residues Thr14, Ala15, Thr16 and Arg19. Moreover, a similar pattern of changes was observed even in the absence of lipids under conditions where MinE was present in excess of MinD, suggesting that this initial interaction may occur before MinD binds to membrane. MinE residues in this conserved loop were previously shown to be important for the MinD-MinE interaction by yeast two-hybrid experiments[71]. However, under our current conditions this interaction does not seem to be sufficient to induce MinE conformational change, since chemical shift changes were relatively small, and did not involve residues that would be expected to show a change for the conversion of a 6- to 4-stranded state. On the other hand, it is also possible that the 4-β stranded structure was induced, but was too low in population to be captured by NMR, with MinE being thermodynamically favored in the 6-β stranded structure.

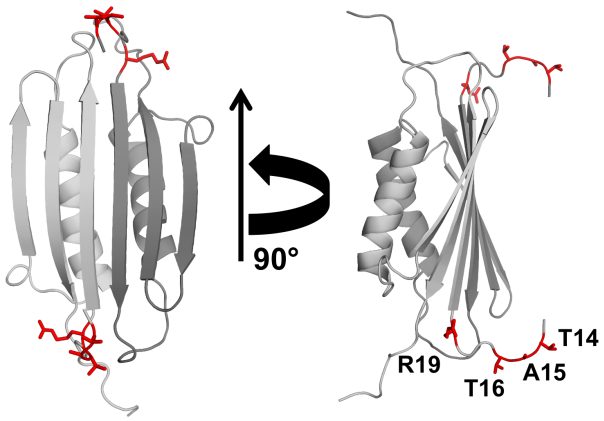

Figure 4.9. Highlighted MinE residues (red) that were shown to experience chemical shifts and intensity changes upon MinD interaction mapped onto *ng*MinE structure (PDB 2KXO) with the MTS removed.

These NMR results suggest that MinE may form a lower-affinity encounter complex with MinD involving exposed loop residues. It will be interesting to determine whether Ile25 plays a role in this initial complex formation, since we found that I25R ΔMTS could not stimulate MinD activity. In the future, it will be interesting to see if the same pattern of shift differences is observed for this mutant, or if the arginine at position 25 somehow interferes with this interaction. Alternatively, Ile25 may instead be important for the conformational transition to the 4-stranded state after formation of the encounter complex, though a mechanism that has yet to be determined. Whatever the scenario, our NMR results provide new evidence of a lower affinity interaction between MinE and MinD that does not require lipids, or a conformational transition in MinE to occur.

One possibility that is raised by the different type of interaction between MinE and MinD that is suggested by our NMR results is that this interaction may be sufficient to stimulate ATP hydrolysis by MinD. According to this scenario, the MinE conformational change would instead be required to regulate another aspect of MinE function, such as E-ring formation. As discussed in the previous chapter, the N-terminal peptide from *ec*MinE containing residues 1 to 31 was shown to form amyloid-like fibrils whereas, the I24N mutant version did not. Based on this study and our MinD ATPase measurements, it was proposed that the higher rate of MinD-catalyzed ATP hydrolysis observed with I24D was a result of the inability of I24D to form fibril-like structures.

Thus, MinE conformational change could be required to create higher order intermolecular interactions that potentially underlie the E ring.

Another potential function of MinE conformational change is to displace MinC from the membrane-bound MinD complex. As demonstrated in Chapter 1, biochemical studies showed that the MinC binding site on MinD overlaps with the MinE binding site (Fig 1.8). However, examination of MinD-MinE complex structure shown in Fig 1.11 revealed that MinE residues 14 to 25 that are important for MinD ATP stimulation are located at the bottom of MinD-binding groove while, MinE residues 26 to 31 bind to the top of the groove where MinC also binds. This suggests that MinE has to undergo the transition from the 6- to 4-β sheet structure to expose the full antiMinCD domain in order to reach the end of the groove where it can compete with MinC binding. Thus, beside its role in modulation MinD ATP hydrolysis, the importance of MinE conformational change could be linked to MinC displacement from membrane-bound MinD.

Interestingly, the quality of the NMR spectrum for ΔMTS was poor in the presence of excess amounts of WT (Fig 4.7A) or inactive mutant D40A MinD (Fig. 4.8), with only peaks from flexible termini being visible, suggesting that a stable complex had formed. While this poor quality could be the result of protein aggregation, there were no visible signs of protein aggregation in the sample with mutant D40A. These results suggest a complex had formed between MinD and MinE, potentially by inducing a conformational change in MinE to give rise to a higher-affinity complex. If this is the case, it may be possible to use labeling and relaxation-optimized NMR experiments that are tailored for larger protein complexes to probe the MinE conformational change induced by MinD[140,141].

The results from this chapter could serve a starting point to characterize MinD-induced MinE conformational change in the future. For example, to ensure that changes in NMR spectra do not arise from time-dependent changes in sample conditions (e.g. pH, ATP concentration, etc.), it would be better to use the catalytically inactive MinD mutant D40A instead of ATPγS with WT MinD, since this analog did not mimic similar functions of ATP-bound MinD. It will also be necessary to develop strategies to reduce the occurrence of protein aggregation upon complex formation. For this purpose, it may be useful to use a MinD mutant that is missing 10 residues from the C-terminus

responsible for membrane binding, since this greatly enhances the solubility of MinD. Even with these changes, the large size of the MinD-MinE complex could be a challenge for solution NMR characterization and will likely require labeling and relaxation-optimized NMR experiments geared towards the study of larger proteins[140]. This may nonetheless remain a significant challenge, however, given the poor quality of the spectrum of the I24D ΔMTS mutant seen in Chapter 3. The broad peaks seen in that spectrum may reflect an inherently dynamic, meta-stable 4-stranded state that could prevent observation of its spectrum when bound to MinD. In this case it might be necessary to turn to lower resolution methods (e.g. fluorescence spectroscopy, CD spectroscopy) to identify the conditions required to induce this conformational change. It may also be possible to study the NMR spectrum of ΔMTS in the presence of small amounts of MinD, and look for evidence of the small population of 4-stranded state through spin relaxation measurements, or amide exchange. Ultimately, through these types of experiments, we hope to understand how MinD induces MinE to cross what is expected to be a significant energy barrier to the conformational change that allows the 6-standed state to be reconfigured into the 4-stranded state that fully exposes the anti-MinCD domain.

Chapter 5

The Role of Membrane Properties in Modulation of MinD ATP Hydrolysis

Collaborators contributions:

Kristopher Fequet executed MinD ATPase reactions stimulated by MinE WT and I24D ΔMTS in absence of phospholipids (Fig 5.8)

5.1: Introduction

As discussed in Chapter 1, membrane characteristics such as charge and fluidity have been shown to modulate MinD-membrane binding affinities. Specifically, MinD interacts with membrane with anionic headgroups and lower melting temperatures preferentially[33,117]. Also, MinD was shown to alter membrane properties such as lipid domain segregation and lipid membrane structure[60,72,142,143]. More importantly, membrane charge and fluidity have been shown to play roles in defining Min pattern formation on planar lipid membranes *in vitro*[52,56]. However, the role of membrane properties in the modulation of MinD ATP hydrolysis is still unknown. Since MinD ATP hydrolysis is the fuel of the Min oscillation cycle, we are interested in exploring the effects of membrane properties such as charge, fluidity and curvature in modulation of MinD ATP hydrolysis *in vitro*. In this chapter, MinE-stimulated MinD ATP hydrolysis was monitored as a function of various membrane properties by using a range of lipid mixtures that mimick different states of membrane charge, fluidity and curvature. Our results demonstrated that membrane properties such as charge and fluidity, but not membrane curvature modulate MinD ATP hydrolysis *in vitro*. MinD ATP hydrolysis was found to be much faster in anionic lipids such as DOPG compared to *E. coli* lipids. In contrast to results obtained with *E. coli* lipids, our data showed that interaction between MinE and the membrane, and the conformational change in MinE do not influence the maximal rate of MinD-catalyzed ATP hydrolysis on DOPG lipids. This suggests that in anionic lipids MinE is no longer linked to the rate-determining step in MinD ATP hydrolysis cycle.

5.2: Results

5.2.1: The Effects of Membrane Charge on MinD-Catalyzed ATP Hydrolysis

Lipid mixtures comprised of anionic and zwitterionic lipids were used to probe the role of membrane change in the modulation of MinD-catalyzed ATP hydrolysis. As shown in Figure 5.1, MinD activity was not stimulated by MinE in the presence of SUVs made from DOPC lipids beyond background levels. However, MinD-catalyzed ATP

hydrolysis rates increased as the anionic lipid DOPG was introduced into the lipid mixture. Although the increase in rate was small, it was approximately linear until the mole fraction reached about 60 %. At that point the MinD ATPase rates showed a much stronger dependence on anionic lipid content. This suggests that there is a minimum membrane charge required in order to activate MinD, and that beyond a threshold value of 60 % DOPG, the anionic lipid plays a strong role in activation of MinD.

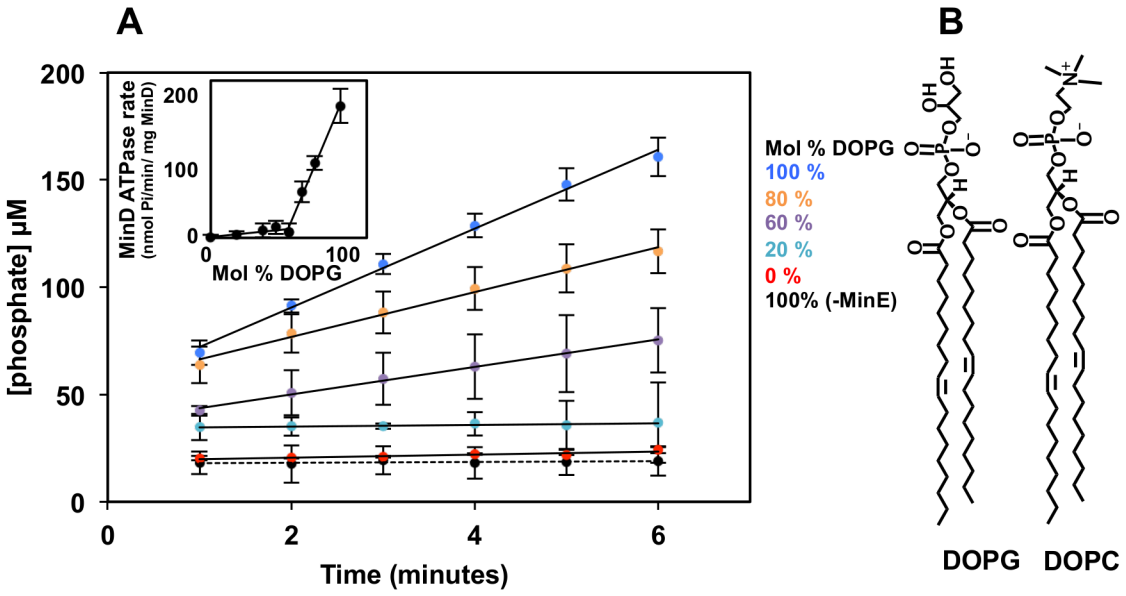

Figure 5.1. The effects of membrane charge in modulation of MinD ATP hydrolysis. A) Initial rate profiles of MinD ATPase activity with liposomes made with lipid mixtures comprised of DOPG and DOPC at the indicated molar ratio. Assays were run with 0.5 mg/ml lipid mixtures in the presence of 3 µM MinE. The inset shows the MinD ATPase rate as function of DOPG mole ratios. Best fit lines for the 0 – 60% ($y = 20x + 0.7$, $R^2 = 0.7$) and the 60 – 100 % range ($y = 420x – 255$, $R^2 = 0.994$) are shown. B) Chemical structures of DOPG and DOPC lipids used in this reaction.

5.2.2: The Role of Membrane Fluidity in Modulation of MinD-Catalyzed ATP Hydrolysis

Membrane fluidity is another characteristic of the membrane that may influence MinD-catalyzed ATP hydrolysis. To probe the role of membrane fluidity, MinD ATPase activity was measured in lipid environments where membrane fluidity was gradually increased. To do so, MinE-stimulated MinD ATP hydrolysis was examined in the presence of POPG, an asymmetric lipid that contains a phosphoglycerol headgroup similar to DOPG but with a singly unsaturated C18 acyl chain and a saturated C16 acyl

chain, in contrast to the two singly unsaturated C18 acyl chains contained in DOPG. The differences in length of acyl chains and saturation level between POPG and DOPG result in a higher phase-transition temperature for POPG relative to DOPG (-2 versus -18 °C)[144,145]. These differences give rise to a lower degree of fluidity in POPG relative to DOPG membranes. As shown in Figure 5.2, the initial rates of MinD-catalyzed ATP hydrolysis increased linearly with the mole fraction of DOPG increased in lipids mixtures. Interestingly, no activity was observed for MinD with vesicles made from pure POPG. These results show that the fluidity of the bilayer is also an important factor in regulating MinD ATPase activity.

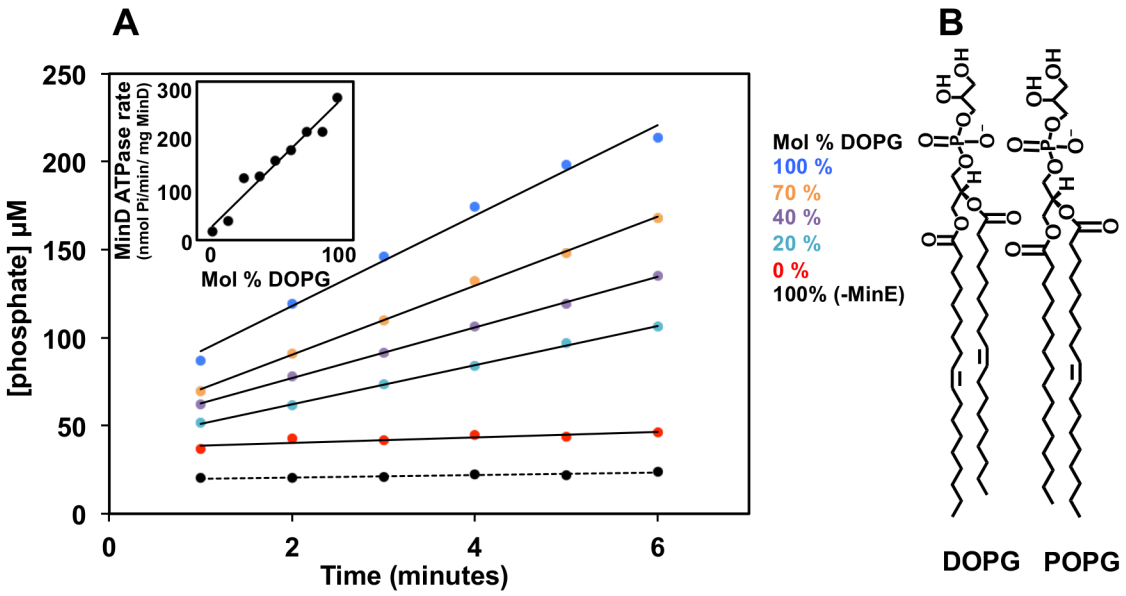

Figure 5.2. The effect of membrane fluidity on the modulation of MinD-catalyzed ATPhydrolysis. A) Initial rate profiles of MinD ATPase activity on membranes comprised of mixtures of DOPG and POPG. The inset shows the MinD ATPase rate as a function of the mole percent of DOPG in POPG, with the least squares fit shown as a ling ($y = 30x - 3$, $R^2 = 0.96$) B) The structure of DOPG and POPG lipids used in this reaction.

5.2.3: The Role of Membrane Curvature in Modulation of MinD ATP Hydrolysis

One hypothesis that has been forwarded to explain the oscillation pattern of Min proteins is that recruitment of MinD to the cell poles in rod-shaped bacteria is favored by the abundance of anionic lipids such as PG and CL at the cell poles[117]. However, the initiation of the oscillation cycle at the cell pole has also raised questions about the potential for membrane curvature to play a role in modulating ATP hydrolysis by MinD.

To test this hypothesis, small unilamellar vesicles with a diameter of 100 nm, and large unilamellar vesicles with a diameter of 1000 nm were compared for their ability to stimulate MinD ATPase activity. As illustrated in Figure 5.3, initial rates of MinD ATP hydrolysis in the presence of small unilamellar vesicles (SUVs) and large unilamellar vesicles (LUVs) were indistinguishable, suggesting that membrane curvature does not affect the rate of ATP hydrolysis by MinD.

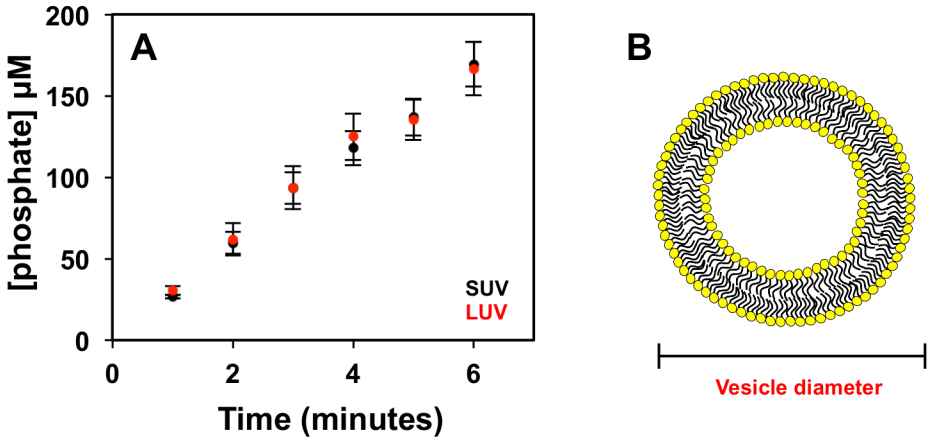

Figure 5.3. The role of membrane curvature in modulation of MinD ATP hydrolysis. A) Initial rate profiles of MinD ATPase activity stimulated by 1 µM MinE in presence of small unliamellar vesicles (black) and large unliamellar vesicles (red). B) Cartoon representation of a vesicle.

5.2.4: MinD ATPase Activity on DOPG Phospholipids

Our data shows that MinD ATPase activity is higher in presence of vesicles made of DOPG lipids compared to those made from *E. coli* lipid extracts. As shown in Figure 5.4, the catalytic constant for MinD ATPase activity is ~10-fold higher with DOPG relative to that obtained in *E. coli lipids* (Table 5.1). Interestingly, the apparent MinD-MinE binding affinity ($K_{0.5}$) on DOPG lipids is ~6.5-fold weaker than apparent binding affinity on *E. coli* lipids. A Hill coefficient equivalent to ~ 2 was observed with both DOPG and *E. coli* lipids, suggesting that the oligomeric state of the MinD-MinE complex is similar in both cases, where binding of MinE to one MinD dimer site stimulates ATP hydrolysis at the other subunit.

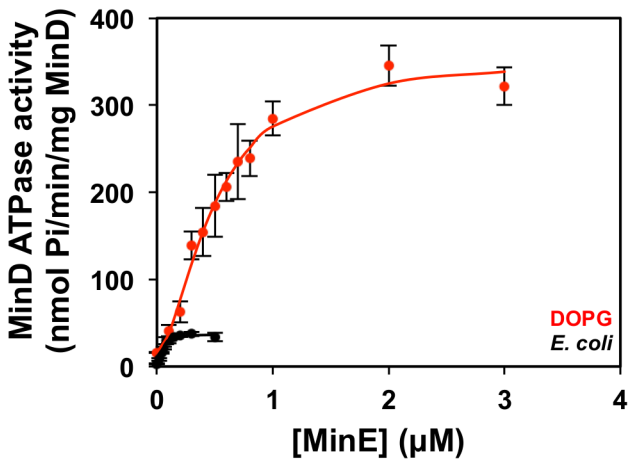

Figure 5.4. Comparison of MinD ATPase activities on DOPG and *E. coli* lipid membranes. MinD ATPase activity with 0.5 mg/ml *E. coli* lipid SUVs (black) and DOPG SUVs (red) as a function of MinE concentrations fitted to Hill equation.

Table 5.1. Kinetic parameters of MinE-stimulated MinD ATP hydrolysis in different lipids

Lipids	k_{cat} (min^{-1})	$K_{0.5}$ (μM)	h
E. coli	1.1 ± 0.1	0.070 ± 0.008	2.7 ± 0.4
DOPG	10.7 ± 0.7	0.5 ± 0.05	1.9 ± 0.08

5.2.5: The Role of the MinE-Membrane Interaction in Modulation of MinD ATPase Activity on DOPG membranes

As presented in Chapter 3, the interaction between MinE and the membrane slows down the rate of MinD-catalyzed ATP hydrolysis on *E. coli* lipids. Since MinE-membrane binding affinity is 10-times stronger with anionic lipids (DOPG) compared to *E. coli* lipids[33], we were interested to determine whether the MinE-membrane interaction also slows the rate of ATP hydrolysis by MinD. For this purpose, a similar suite of MinD ATPase assays with the ΔMTS MinE construct was performed in presence of DOPG lipids. Surprisingly, ΔMTS MinE was able to stimulate MinD ATP hydrolysis to a similar extent as observed with the full length WT MinE. However, these profiles are not superimposable, with maximal MinD-catalyzed ATP hydrolysis by WT being slightly faster (by ~10%) with an apparent MinE binding affinity ($K_{0.5}$) that was slightly weaker

than ΔMTS. This suggests that the MinE-membrane interaction does not contribute significantly to modulation in MinD ATP cycle on DOPG lipids (Figure 5.5 and Table 5.2).

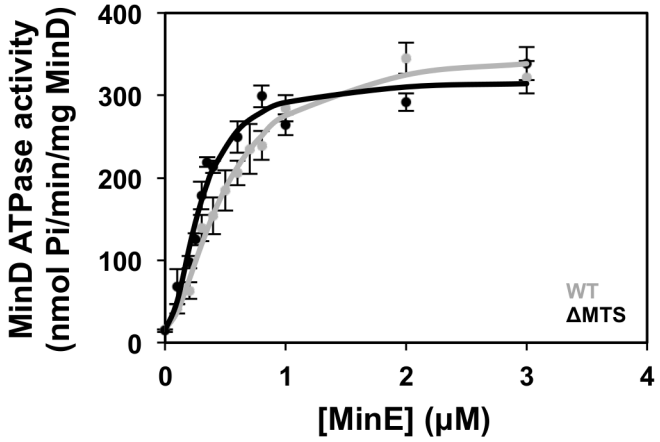

Figure 5.5. MinE-stimulated MinD ATPase activity to probe the MinE-membrane interaction in the presence of DOPG lipids. Initial rates of MinD-catalyzed ATP hydrolysis stimulated by WT (grey) and ΔMTS (black) MinE fitted to Hill equation.

Table 5.2. Kinetic parameters of stimulated MinD ATP hydrolysis by different MinE constructs on DOPG lipids

	k_{cat} (min^{-1})	$K_{0.5}$ (μM)	h
WT	10.8 ± 0.1	0.50 ± 0.05	2.0 ± 0.1
ΔMTS	10.0± 0.1	0.30 ± 0.10	2.2 ± 0.2
I24D ΔMTS	10.4 ± 0.1	0.22 ± 0.03	3.0 ± 0.5
12-30	11.4 ± 0.1	0.85 ± 0.08	2.0 ± 0.3

5.2.6: Investigation of the Effect of the MinE Conformational Change on the Stimulation of MinD ATPase Activity on DOPG Membranes

The similarity in stimulation of MinD ATPase activity by both WT and ΔMTS MinE with DOPG lipids raises the question as to whether the MinE conformational change plays any role in the modulation ATP hydrolysis by MinD on these negatively charged membranes. To address this question, stimulation of MinD ATP hydrolysis by the 4-stranded MinE mutant I24D ΔMTS was compared to full length WT and ΔMTS MinE. As shown in Figure 5.6, I24D ΔMTS showed a similar MinD ATP hydrolysis

activation profile to those obtained for full-length and ΔMTS MinE in DOPG. While there was only a very small difference in V_{max} and $K_{0.5}$ between WT and I24D ΔMTS, the 4-stranded mutant I24D ΔMTS showed higher cooperativity compared to both full-length and ΔMTS WT MinE. Overall, our results suggest that the MinE conformational change influences its ability to stimulate ATP hydrolysis at more than one site in the presence of anionic lipids (DOPG).

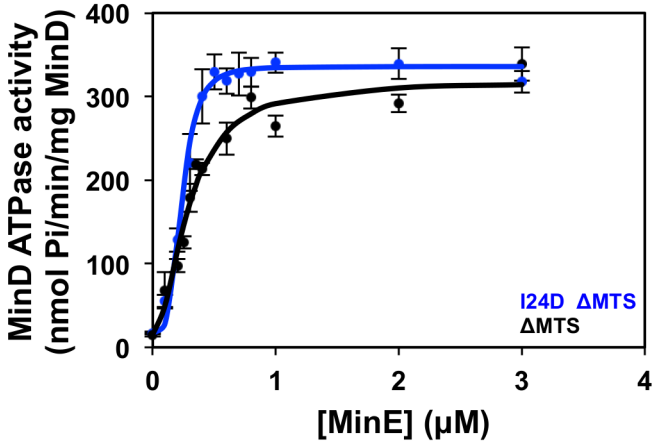

Figure 5.6. Comparison of MinD ATPase activity stimulated by WT or I24D ΔMTS MinE to probe the conformational change of MinE in the presence of DOPG lipids. Initial rates of Min-catalyzed ATP hydrolysis stimulated by ΔMTS (black) and I24D ΔMTS (blue) fit to the Hill equation.

5.2.7: The Dimeric State of MinE is not Required to Stimulate MinD ATP hydrolysis on DOPG Membranes

The ability of a MinE peptide containing residues 12-30 to stimulate MinD ATP hydrolysis in *E. coli* lipids suggests that MinE dimerization is not required to stimulate MinD ATP hydrolysis. However, since the roles of MinE-membrane interaction and MinE conformational change in modulating MinD ATP hydrolysis depends on lipid identity, we were interested in exploring the role of MinE dimerization in MinD activation. We therefore tested the ability of the MinE (12-30) peptide to stimulate MinD ATP hydrolysis in DOPG. As shown in Figure 5.7 and Table 5.2, this peptide was also able to stimulate MinD ATP hydrolysis at rates that were slightly faster than those observed for both full length and ΔMTS MinE (5 - 10%). However, the apparent affinity

of this peptide appears to be ~2 times lower for MinD relative to ΔMTS, which may reflect the regions of MinE C-terminal to residue 30 that may also influence binding.

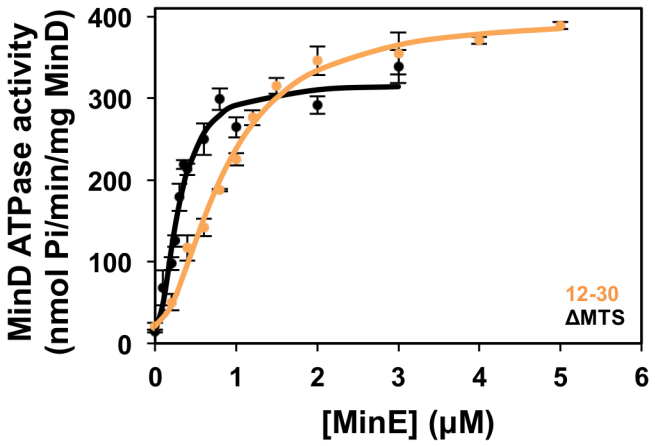

Figure 5.7. Comparison of MinD ATPase activity stimulated by full length MinE and MinE (12-30) in the presence of DOPG lipids. Initial rates of MinD-catalyzed ATP hydrolysis stimulated by ΔMTS MinE (black) and the MinE (12-30) peptide (orange) fit to the Hill equation.

5.2.8: Membrane is Required to Activate MinD ATP Hydrolysis

The high degree of similarity in MinD ATP hydrolysis profiles stimulated by WT and I24D ΔMTS MinE on DOPG indicates that MinE conformational change does not play a significant role in modulation of MinD ATP hydrolysis on anionic lipids. However, this does not rule out the possibility that direct interactions between MinE and the membrane may help to stimulate the transition from the 6-stranded to the 4-stranded state. To explore this question, we tested the ability of the I24D ΔMTS MinE to stimulate MinD ATP hydrolysis in absence of lipids, since its MinD-binding sequence is solvent-exposed in the 4-stranded state. However, as shown in Fig 5.8, I24D ΔMTS MinE was unable to stimulate MinD ATP hydrolysis beyond background level in the absence of lipids similar to WT MinE. These findings reinforce the importance of interaction between MinD and the membrane for the activation of its ATPase activity.

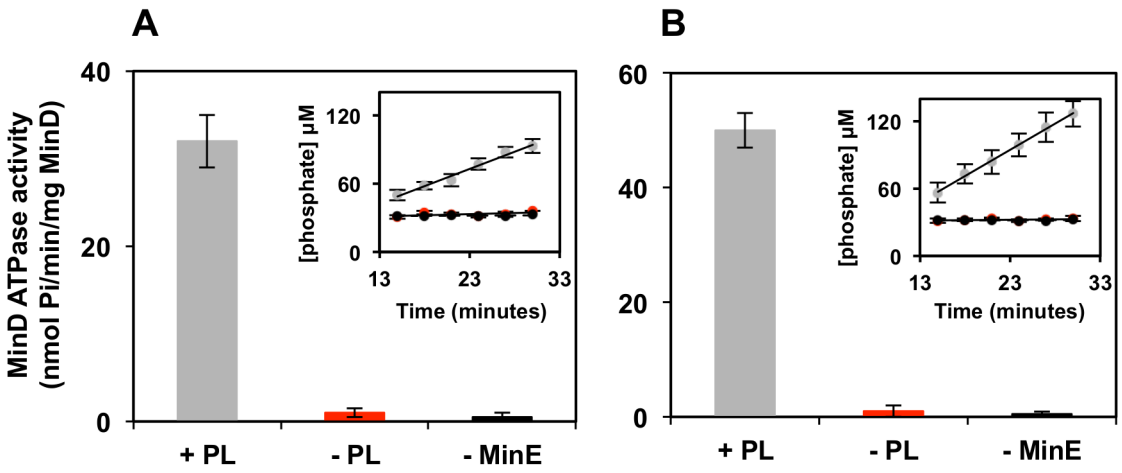

Figure 5.8. Examination of the ability of MinE to stimulate MinD ATPase activity in the absence of the membrane. MinD ATPase activity stimulated by A) MinE WT and B) I24D ΔMTS in the presence of *E. coli* phospholipids (PL) (gray) and in the absence of *E. coli* phospholipids (red) where background levels of MinD ATP hydrolysis with no MinE (black) is shown. Insets show the initial rate profiles.

5.3: Discussion

The results from this study show that MinD activity is dramatically affected by changes in membrane properties. Specifically, a minimum threshold of anionic lipid was required for any stimulation of ATP hydrolysis, which in binary mixtures of DOPG in DOPC required a mole fraction of at least 60 % before significant activation was observed. In spite of the low activity observed at lower ratios of DOPG, it is likely that MinD is still able to bind the membrane, as MinD binding to membranes comprised of PC alone has been demonstrated[33,117]. This 60 % threshold may be higher than the ~30 % anionic lipid that is estimated to be contained by weight in the *E. coli* lipid extracts used to make membranes in our study, although this is a difficult comparison to make since fluidity also affects activity. In the case of anionic lipids, there was a clear linear relationship between fluidity and MinD activity, with greater fluidity giving rise to greater activity. Both lipids are significantly more fluid than *E. coli* membranes, which typically have a phase transition temperature in the ambient room temperature range[144,145] However, our results highlight the importance of the membrane in the MinD ATPase cycle, and suggest that at least some part of the lipid surface must be negatively charged

in order for activation to occur.

As demonstrated in Chapter 3, the rate-determining step in the Min cycle is the dissociation of MinE from the membrane when *E. coli* lipids are used. Based on the higher binding affinity measured for MinD on membranes containing anionic lipids, this gave rise to the hypothesis that the ATP hydrolysis reaction might be slower on membranes containing higher proportions of anionic charge relative to the *E. coli* membrane. Surprisingly, MinE-stimulated MinD ATPase activity was significantly higher on DOPG lipids, and did not show a significant difference in V_{max} when stimulated by the MinE construct missing the MTS. However, the amount of MinE required to reach half-maximal stimulation was lower for the ΔMTS construct, suggesting that on anionic membranes, the MTS makes the interaction between MinD and MinE less favorable. A similar result was also obtained with I24D ΔMTS, suggesting that the MinE conformational change does not modulate the rate of MinD ATP hydrolysis in this system. While the absence of an effect on V_{max} for the ΔMTS mutants indicates that MinE-membrane dissociation is not a rate-determining step for the reaction on highly fluid anionic membranes, the change in the $K_{0.5}$ is consistent with an inhibitory effect of the MTS on the MinD-catalyzed ATP hydrolysis cycle.

The absence of a large effect on V_{max} for the ΔMTS MinE mutants indicates that the dissociation of MinE from the membrane is not the rate-limiting step in the Min cycle on DOPG membranes. It is likely that all steps in the Min protein cycle that involve the lipid membrane have altered rates, making it difficult to identify what the rate-determining step would be under these conditions. However, some insight into the role of the membrane is provided by the observation that the interaction with the membrane is a fundamental requirement for the activation of MinD, since the 4-stranded mutant I24D ΔMTS was not able to promote ATP hydrolysis by MinD in the absence of lipids, even though an equivalent mutant of *ec*MinE binds *ec*MinD in the absence of membranes. In fact, this interaction was strong enough to allow the x-ray crystal structure of the MinDE complex to be determined without the need for any membrane-mimetic agents[77]. Given the requirement for membrane binding to promote catalysis, it is likely that this MinDE structure did not capture the activated state of MinD. Therefore, there appears to be an additional conformational change induced in MinD upon membrane binding that gives

rise to a catalytically competent state. This would explain why the crystal structure of the complex did not provide clear insight into how MinD is activated by MinE, since the absence of a lipid membrane kept MinD in its inactive state. Our results suggest that negatively charged lipids are a critical component of this activating interaction, with more fluid bilayers being more effective at promoting catalysis, potentially through the increased affinity of MinD for the membrane.

Although there are local differences in lipid composition in bacteria, with cardiolipin being enriched in the polar regions, *in vitro* studies of Min protein pattern formation have demonstrated that pole-to-pole oscillation can be established in rod-shaped compartments on synthetic mixtures of lipids[123]. Therefore it is not necessary for local composition differences to be established *in vivo* for proper Min protein function. However, *in vitro* observations that MinD binding to lipid can induce the formation of microdomains of negatively charged lipid, and simultaneously increase the fluidity of the lipid bilayer[142], suggest this can have an impact on ATP hydrolysis rates, with MinD binding essentially modulating the local lipid environment to increase rates of MinD-catalyzed ATP hydrolysis. Consistent with this hypothesis, the hill coefficient for MinE-stimulated MinD activity consistently shows values that are slightly larger than two. Although the uncertainty in cooperativity values makes it difficult to evaluate the significance of this observation, it is interesting that it has been observed consistently for most profiles on both DOPG and *E. coli* membranes. This may help to explain why a critical mass of MinD accumulates on the membrane before it undergoes rapid cooperative dissociation from the membrane, as seen on planar bilayers *in vitro*[53].

One aspect of the MinD-membrane interaction that cannot be ruled out is the potential for higher order structures to be formed by MinD on the membrane. A number of *in vitro* experiments have suggested that MinD can form polymeric structures on membranes, although these are often with concentrations that are far from a physiological range[34,60]. Nonetheless, these observations could be a reflection of higher-order interactions occurring between MinD dimers on the membrane, which raises the possibility that differences in membrane properties might have an impact on these polymers. In the future it will be interesting to determine whether MinD polymer formation actually underlies oscillation and pattern formation, and if so, how membrane

properties effect these interactions.

Although ATP hydrolysis is the chemical energy source that is required for oscillation and pattern formation, the link between ATP hydrolysis rates and dynamic long-range ordering of Min proteins is not clear. Nonetheless, it has been shown that a mutant of Lys19 in *ec*MinE stimulates ATP hydrolysis by MinD at a slower rate than WT *ec*MinE, and also gives rise to a slower oscillation rate[42]. Also, studies with fluorescently labeled MinD and MinE on a planar lipid surface showed that the velocity of Min propagating waves increases as MinE concentration increases, conditions that would also be expected to increase the rate of MinD-catalyzed ATP hydrolysis[52,56,54]. Meanwhile, the morphology of Min patterns was also shown to depend on the concentration of anionic lipid present in the membrane, with no patterns being observed at higher PG concentrations (e.g. 73 %). This raises the possibility that long-range order cannot be established if ATP hydrolysis rates are too fast. Along with membrane charge, membrane fluidity also influences the formation of Min pattern (i.e. amoeba-like structure like more fluidic membrane)[54,56]. Overall, these results suggest that the modulation of the rate of MinD-catalyzed ATP hydrolysis may serve as a regulatory mechanism to control the timing of Min oscillation.

To conclude, membrane charge is required for MinD activation while membrane fluidity modulates MinD ATPase activity. In *E. coli*, it appears that the Min proteins have evolved to allow activation by the membrane charge and fluidity that is typical for the composition of lipids that make up the inner membrane. While the role of the membrane in the activation of MinD activity is still unclear, we speculate that it induces a conformational change in MinD that is necessary to promote catalysis of the hydrolytic reaction. In the future it will be interesting to probe this conformational change, and to determine the role that anionic lipid headgroups play in generating the activated state.

Chapter 6

Conclusion and Future Goals

Previously in the Goto lab, identification of MinD-interacting residues in the MinE structure showed that they were located on the central β1 strand at the dimeric interface[43]. A subsequent structure determination of MinE bound to MinD[77] showed that these residues become exposed to allow interactions with MinD. This led to our investigation into how MinE adopts these different conformational states *in vivo*. In this work, we have demonstrated that MinE undergoes conformational changes upon interaction with the membrane consistent with the 4-β sheet structure seen in the MinD-MinE complex. We also have shown that MinE interactions with the membrane and MinE conformational change modulate the rate of ATP hydrolysis by MinD on *E. coli* lipids. Our results suggest that the dissociation of MinE from the membrane is the rate-limiting step in the Min interaction cycle on membranes comprised of *E. coli* lipids.

Interestingly, when MinE is in the 4-stranded state it is able to bind MinD in the absence of membranes, but is not capable of stimulating ATP hydrolysis by MinD. Moreover, the physical properties of the membrane play an important role in modulation of MinD-catalyzed ATP hydrolysis rates, where negatively charged lipids are required to activate MinD ATP hydrolysis while membrane fluidity modulates it. Interestingly, in a pure anionic lipid environment, the rate-determining step is no longer linked to MinE dissociation. In the absence of measured rates for all steps involved in the Min protein interaction cycle, it is not possible to identify the rate-determining step under these conditions.

6.1. The Rate of MinE Conformational Change

The ability of both ΔMTS and I24D ΔMTS to stimulate MinD ATP hydrolysis to similar levels and the absence of large differences in NMR spectra of ΔMTS in the presence of MinD and lipids suggests that MinD-induced MinE conformational change is fast, and that the 4-stranded state is not long-lived. A recent study combined mathematical modeling and experimental data to predict that MinE conformational change back from the 4- to 6-stranded state occurs in order of 10 ms[146]. This MinE conformational change is proposed to be a mechanical force that drives the formation of

Min pattern. However, more direct rate measurements are needed in order to verify this hypothesis. To accomplish this, MinD-induced MinE conformational change could be measured by introducing a fluorescent probe that where the fluorescence intensity is modulated by MinE conformational change. For example, fluorescent labels such as ATTO can be quenched by a Trp residue that is within 10 Å, as was previously used to characterize conformational changes in FtsZ[147]. This would require one subunit in the MinE dimer to be mutated to introduce Trp and the other subunit to have a mutation to Cys to allow derivitization by the ATTO probe. For example, the intramolecular distance between Ala31 and Gly71 is predicted to place probe and quencher < 10 Å apart in the 6-β sheet structure, and >18 Å in the 4-β sheet state (Fig 6.1).

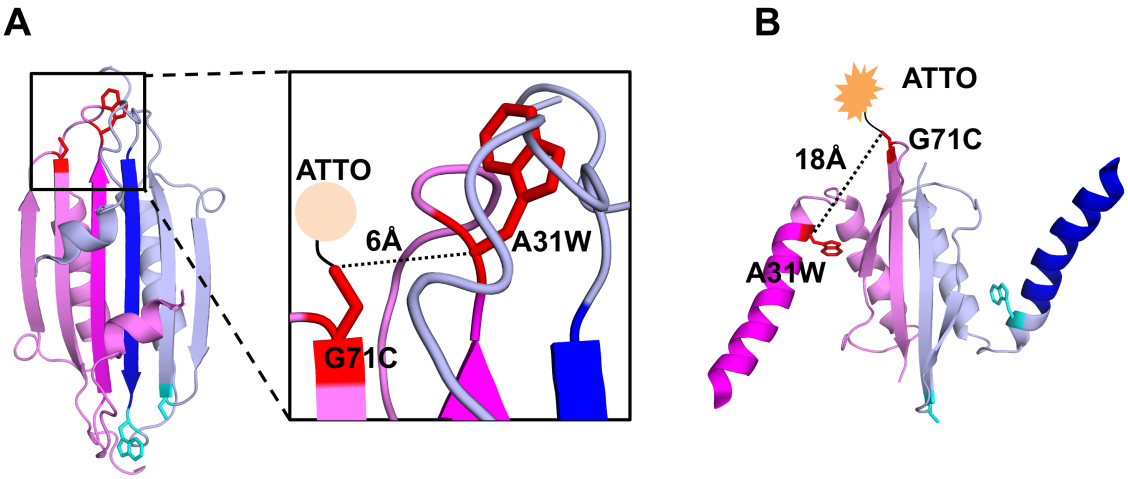

Figure 6.1. Structure of MinE showing the proposed mutations to probe MinE conformational change. A) *ng*MinE (PDB 2KXO) with mutations A31W and G71C that, when derivatized by the ATTO-655 probe, would give rise to a < 10 Å distance separating fluorophore and quencher. B) *ec*MinE (PDB 3R9J) in the 4-stranded β sheet state predicts the distance between ATTO-655 and Trp to be ~18 A, giving rise to fluorescent ATTO that is no longer quenched by Trp. (Note that the structure of ATTO-665 (Sigma-Aldrich) is propriety, although it suggested by the manufacturer to be more rigid and photostable than fluorescein and cyanine-based dyes).

With this type of labeling, the rate of membrane-induced MinE conformational change could be measured for WT MinE, and compared to the rate for ΔMTS MinE by stopped flow fluorescence measurements. Meanwhile, it is interesting to measure how long induced MinE 4-stranded state conformational change persists. This could be done by single particle fluorescence which is becoming a popular technique to measure protein

conformational rates. The results from these experiments will provide additional information on whether membrane-induced MinE conformational change persists in the 4-stranded state and how long it takes to revert back to 6-stranded state.

6.2. MinE as a Regulatory Point in the Min Interaction Cycle

Our proposal that MinE-membrane dissociation is the rate-determining step in the Min interaction cycle suggests that membrane-bound MinE is not more efficient at stimulating MinD activity than its aqueous 6-stranded state. We proposed that self-association of membrane-associated MinE could be inhibitory to both membrane dissociation and interactions with MinD (Chapter 3). While this hypothesis is supported by EM of fibrils formed by MinE on bilayers, it is not clear if this self-association occurs in the presence of MinD. Thus, in the future it will be interesting to probe the role of MinE self association in the modulation of MinD ATP hydrolysis. One method to investigate this is to measure MinD ATP hydrolysis stimulated by a MinE mutant that could trap higher order oligomeric states. This could be done by introducing a cysteine mutation at a residue that may be in close proximity with another cysteine residue in an adjacent dimer. For example, Ala27 in central β1 sheet is in the anti-MinCD α-helix in the 4-stranded state, where it might have the potential to cross-link with another cysteine residue at position 27 as shown in Fig 6.2. If MinE crosslinks and forms the a higher-order structure involving this part of MinE, then under oxidizing, but not reducing conditions, the MinD ATPase activity would be inhibited. Ultimately, results from these types of experiments could help to better understand why MinE-membrane dissociation is the rate-determining step in Min interaction cycle.

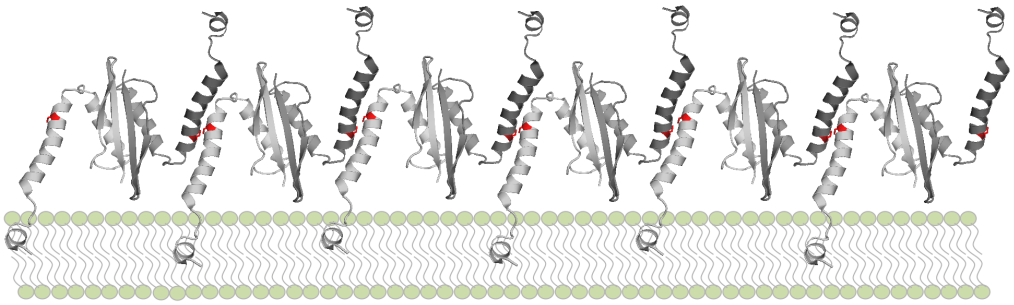

Figure 6.2. Proposed model of higher order *ng*MinE oligomers. *ec*MinE (PDB 3R9J) highlighting the Ala27 site that might be used to probe the interaction (red).

6.3 Importance of MinD-Membrane Interactions

The inability of I24D ΔMTS to stimulate MinD ATP hydrolysis in the absence of lipids raises an important question regarding the role of the membrane in the Min interaction cycle. All reported MinD ATPase activities were obtained in the presence of lipids, suggesting that the membrane induces a conformational change in MinD that is required to allow for MinE binding to stimulate ATP hydrolysis. Thus, it is necessary to gain structural details on membrane-bound MinD. However, in order to crystalize both the MinD dimer and MinD-MinE complex, it was necessary to remove the C-terminal MTS. Therefore structural studies on the full-length protein are not likely to be possible by x-ray crystallography due to its poor solubility. Solution NMR of the MinD dimer would also be very challenging given its large molecular weight, which would be exacerbated by the addition of a membrane-mimetic solvent such as bicelles or micelles. However, it has been shown that selective ^{13}C methyl labeling for a subset of aliphatic amino acids can be done in combination with deuterium labeling to allow the study of macromolecular complexes in the mega-Dalton range, although it remains to be seen whether the membrane-bound state of MinD would be amenable to these types of approaches. With the recent successful progress in the field of cryo-electron microscopy, the structures of a number of challenging complexes, including those of membrane proteins, have been recently elucidated[148,149]. For example, cryo-EM was able to produce a structure of glutamate dehydrogenase (334 kDa) to a similar resolution as previously determined by x-ray crystallography (1.8Å)[150]. The ability to determine structures in the

presence of detergents or lipids has also allowed structures to be determined for membrane proteins such as human γ-secretase (3.4Å)[151]. Although cryo-EM tends to be better suited for larger proteins, the membrane-bound MinD dimer is above the molecular weight (~40kDa) considered to be a limit for this technique[152,153] .In addition, cryo-EM has been used to visualize MinD polymer formation in presence of lipids but with lower resolution[34,60]. Thus, it may be possible to use cryo-EM to characterize the membrane-bound MinD complex to address our questions.

While structural characterization of membrane-bound MinD by cryo-EM is being conducted, site-directed mutagenesis can be also carried out in order to identify regions on MinD region that interact with the membrane. As demonstrated in Chapter 1, MinD interacts with membrane via its MTS at the C-terminus. Analysis of the MinD structure from *E. coli* that lacks the MTS along with sequence alignment analysis of MinD[36,58,154] suggests that the linker loop between the core structure of MinD and MTS is short, giving rise to the proposal that MinD sits on the membrane in the orientation shown in Fig 6.3[77]. As demonstrated in previous chapters, MinD has a higher binding affinity to anionic membrane, therefore, the MinD region that is believed to be involved in membrane interactions is expected to be rich in positively charged residues. MinD sequence alignment identified highly conserved positively charged residues such as Arg188, Arg190 and Arg219 that are located close to the MTS and far from the as MinC-MinE binding groove as shown (Fig 6.3). By using established protocols of Trp fluorescence enhancement upon membrane binding[58], the role of these residues in modulation MinD-membrane interaction can be investigated by introducing mutations at these locations in a MinD variant that contains a Trp probe in the MTS. Moreover, the role of these residues in the modulation membrane-activated MinD could be examined by monitoring the rate of MinD ATP hydrolysis in these mutants. The results from these experiments should provide molecular details to help answer the question as to why MinD-membrane interactions are essential for ATP hydrolysis by MinD.

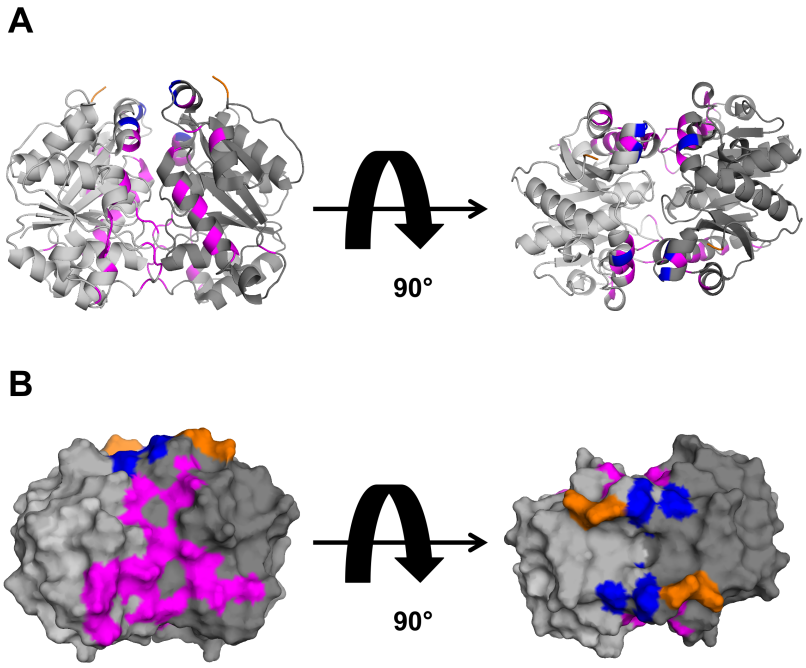

Figure 6.3. Structure of MinD highlighting the region where MinD may bind to the membrane. A) Cartoon representation of the catalytically deficient ATP-bound MinD D40A dimer (light and dark gray) lacking the MTS from *E. coli* (PDB 3Q9L) with the conserved positively charged residues in blue, the MinC/MinE binding site in magenta and the C-terminus where the missing MTS would normally be located in orange. B) Surface representation of the views of MinD in shown in (A).

6.4 MinD Polymerization

Electron microscopy images showed that MinD tends to form lipid tubes and filamentous bundles of MinD polymeric structures in presence of ATP and lipid vesicles[34,60]. EM also showed that the lipid tubes disappeared upon addition of MinE, suggesting that MinE can cause MinD depolymerization, likely through stimulation of its ATPase activity. Dynamic light scattering also showed that the MinE reduces the light scattered by a mixture of MinD bound to lipid vesicles in the presence of ATP, consistent with the disassembly of higher order protein-lipid assemblies[34]. Altogether, this suggests that MinD can form a polymeric structure upon membrane interaction that is disassembled by MinE-stimulated ATP hydrolysis. Thus, the formation of higher-order MinD oligomers on the membrane could be another factor that influences the Min oscillation cycle.

In the future it will be interesting to characterize the MinD polymer and determine its role in the Min interaction cycle. While EM has been used to study MinD oligomerization, lipid:protein ratios that are more representative of physiological conditions do not seem to give rise to a polymer that can be observed by this technique. In addition, routine biophysical approaches for studying protein self-association, such as size-exclusion chromatography, analytical ultracentrifugation, or multi-angle light scattering are not informative for systems that assemble on lipid membranes.

To gain insight into the MinD interactions that give rise to oligomers, site-directed mutagenesis could be done to mutate conserved surface-exposed MinD residues that do not form a part of either the MinD dimer interface or the MinC-MinE binding groove[155]. As shown in Fig 6.4, MinD contains surface residues that are highly conserved forming hydrophobic and charged regions possibility as contact points for MinD polymer formation. For example, Lys30, Lys31, Lys32 and Lys76 in *ec*MinD form a positively charged region located far from the MinD C-terminus, MinC-MinE binding site and MinD dimer interface. The role of these residues in MinD polymerization can be evaluated by EM and DLS, as was previously done[34,60]. If these residues are found to be important for MinD polymerization, they could be used to investigate the role of MinD polymerization in ATP hydrolysis *in vitro* and Min protein oscillation *in vivo* using established methods.

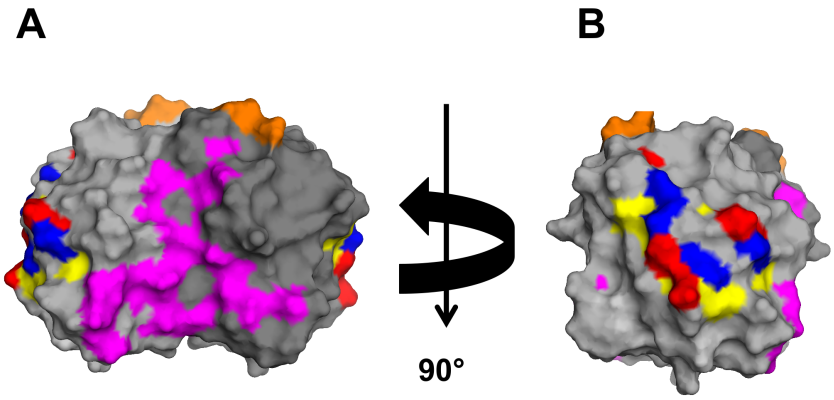

Figure 6.4. Surface representation of the MinD structure highlights possible regions involved in MinD polymerization. Subunits of ATP-bound *ec*MinD (D40A) lacking the MTS (light and dark gray) show surface exposed conserved positively charged residues (blue), negatively charged residues (red), hydrophobic residues (yellow), the MinC-MinE binding site (magenta) and the C-terminus (orange).

6.5. Future Prospects for the Development of New Antimicrobials

The results presented in this thesis demonstrated the role of MinE-membrane interactions and conformational change in the modulation of MinD ATP hydrolysis *in vitro*. Based on our measurements, we concluded that the rate-determining step in the Min interaction cycle on *E. coli* membranes is MinE-membrane dissociation. Although we originally hypothesized that MinE-membrane interactions were required to facilitate its dramatic conformational change to expose the anti-MinCD domain, our findings instead demonstrate that the membrane is required to activate MinD for MinE-stimulated ATP hydrolysis. It is still unclear how the membrane activates MinD, and therefore future structural studies on membrane-bound MinD will be required to address this question.

Ultimately, understanding the molecular details of this cycle has the potential to help develop antimicrobial agents that could reduce the virulence of pathogenic bacteria such as *N. gonorrhoeae* or hemorrhagic *E. coli*. As discussed in Chapter 1, interference with Min system can compromise cell viability, and in pathogenic strains disruption of normal Min system function has been shown to reduce virulence[13,50,77]. Therefore, future development of compounds that can interfere with the Min protein system may be a novel means to treat infections by gram-negative pathogenic bacteria. However, it may be difficult to produce an inhibitor that can effectively alter the Min interaction cycle. For example, based on our proposal that membrane interactions induce conformational changes in MinD, an inhibitor that targets this activated state may be difficult to design until this state is structurally characterized. In contrast, it would be straightforward to synthesize an activator of the Min system, such as a peptide that mimics the MinE antiMinCD domain. As demonstrated in Chapter 1, the rate of MinD ATP hydrolysis is directly linked in Min oscillation cycle such that disruption of this rate alters the Min oscillation and pattern formation. Thus it may be possible to synthesize a peptide that alters the rate of MinD ATP hydrolysis and ultimately disrupt the finely tuned timing of Min protein oscillation.

In efforts to control the Min dynamics by altering MinD ATPase rates *in situ*, the Schwille group[156] developed an optically controlled photoswitch based on a MinE

peptide that is capable of stimulating MinD ATP hydrolysis and triggering MinD-membrane dissociation. In this peptide, Cys mutations were made at Asn13 and Glu20 in a peptide containing *ec*MinE residues 13 to 31 and crosslinked with a photoisomerizable azobenzene moiety. When the azobenzene is in the *trans* configuration, the MinE peptide adopts a random coil while exposure to UV light induces a *cis* configuration that gives rise to a helical structure in the peptide. By doing so, Min pattern formation was shown to be disrupted in a UV light-dependent manner. Using a similar principle, an antimicrobial agent could be developed by synthesizing a *ng*MinE peptide encompassing these same residues with the helical conformation fixed through stapling of residues 13 and 20 with an appropriate linker. Due to potential susceptibility to proteolysis, peptoid analogues of this peptide may be more effective alternatives, as has been demonstrated in previous development of bacteriostatic peptoids[157,158]. This type of activator could induce a faster rate of ATP hydrolysis by MinD, which would be expected to result in uncoupling of MinD ATP hydrolysis from the rest of the Min oscillation cycle. This has the potential to disrupt the Min oscillation pattern to reduce the virulence of targeted pathogens, an intriguing possibility that could be investigated in the future.

Chapter 7

References and Reprint Permissions

1. Lutkenhaus, Joe and Addinall, S. Bacterial cell division and the Z ring. *Annu. Rev. Cell Dev. Biol.* **13,** 395–424 (1997).
2. Erickson, H. P., Anderson, D. E. & Osawa, M. FtsZ in bacterial cytokinesis : cytoskeleton and force generator All in One. *Am. Soc. Microbiol.* **74,** 504–528 (2010).
3. Bramhill, D. Bacterial cell division. *Annu. Rev. Cell Dev. Biol.* **13,** 395–424 (1997).
4. de Boer, P. A. J., Crossley, R. E. & Rothfield, L. I. A division inhibitor and a topological specificity factor coded for by the minicell locus determine proper placement of the division septum in E. coli. *Cell* **56,** 641–649 (1989).
5. Sun, Q., Yu, X. C. & Margolin, W. Assembly of the FtsZ ring at the central division site in the absence of the chromosome. *Mol. Microbiol.* **29,** 491–503 (1998).
6. Barák, I. & Wilkinson, A. J. Division site recognition in Escherichia coli and Bacillus subtilis. *FEMS Microbiol. Rev.* **31,** 311–326 (2007).
7. De Boer, P. A. J., Crossley, R. E. & Rothfield, L. I. Roles of MinC and MinD in the site-specific septation block mediated by the MinCDE system of Escherichia coli. *J. Bacteriol.* **174,** 63–70 (1992).
8. Woldringh, C. L., Mulder, E., Huls, P. G. & Vischer, N. Toporegulation of bacterial division according to the nucleoid occlusion model. *Res. Microbiol.* **142,** 309–320 (1991).
9. Pichoff, S., Vollrath, B., Touriol, C. & Bouché, J. P. Deletion analysis of gene minE which encodes the topological specificity factor of cell division in Escherichia coli. *Mol. Microbiol.* **18,** 321–329 (1995).
10. De Boer, P. A. J., Crossley, R. E. & Rothfield, L. I. Isolation and properties of minB, a complex genetic locus involved in correct placement of the division site in Escherichia coli. *J. Bacteriol.* **170,** 2106–2112 (1988).
11. Ramirez-Arcos, S. *et al.* Conserved glycines in the C terminus of MinC proteins are implicated in their functionality as cell division inhibitors. *J. Bacteriol.* **186,**

2841–2855 (2004).

12. Ramirez-Arcos, S. *et al.* Deletion of the cell-division inhibitor MinC results in lysis of Neisseria gonorrhoeae. *Microbiology* **147,** 225–237 (2001).
13. Szeto, J. *et al.* Gonococcal MinD affects cell division in Neisseria gonorrhoeae and Escherichia coli and exhibits a novel self-interaction. *Am. Soc. Microbiol.* **183,** 6253–6264 (2001).
14. King, G. F. *et al.* Structural basis for the topological specificity function of MinE. *letters* **7,** 1013–1017 (2000).
15. Hu, Z. & Lutkenhaus, J. Topological regulation of cell division in Escherichia coli involves rapid pole to pole oscillation of the division inhibitor MinC under the control of MinD and MinE. *Mol. Microbiol.* **34,** 82–90 (1999).
16. Rowland, S. L. *et al.* Membrane redistribution of the Escherichia coli MinD protein induced by MinE membrane redistribution of the Escherichia coli MinD protein induced by MinE. *J. Bacteriol.* **182,** 613 (2000).
17. Boer, P. A. J. D. E. *et al.* Isolation and properties of minB, a complex genetic locus involved in correct placement of the division site in Escherichia coli. *J. Bacteriol.* **170,** 2106–2112 (1988).
18. Eng, N. F., Szeto, J., Acharya, S., Tessier, D. & Dillon, J. A. R. The C-terminus of MinE from Neisseria gonorrhoeae acts as a topological specificity factor by modulating MinD activity in bacterial cell division. *Res. Microbiol.* **157,** 333–344 (2006).
19. Nguyen, H. N., Romero Jovel, S. & Nguyen, T. H. K. Nanosized minicells generated by lactic acid bacteria for drug delivery. *J. Nanomater.* **2017,** (2017).
20. Jivrajani, M. & Nivsarkar, M. Ligand-targeted bacterial minicells: futuristic nano-sized drug delivery system for the efficient and cost effective delivery of shRNA to cancer cells. *Nanomedicine.* **12,** 2485–2498 (2016).
21. Public Health. Canadian guidelines on sexually transmitted infections. *Can. Med. Assoc*. **176** (2)**,** 175–176 (2006).
22. Tapsall J, M, D. Multi drug resistant Neisseria gonorrhoeae. *Can. Med. Assoic.* **180,** 268–269 (2009).
23. Tapsall, J. Antimicrobial resistance in Neisseria gonorrhoeae. *Who* **1,** 1–58 (2001).

24. Ota, K. V. *et al.* Prevalence of and risk factors for quinolone-resistant Neisseria gonorrhoeae infection in Ontario. *Can. Med. Assoc.* **180,** 287–290 (2009).
25. Martin, I. *et al.* Emergence and characterization of neisseria gonorrhoeae isolates with decreased susceptibilities to ceftriaxone and cefixime in Canada: 2001-2010. *Sex. Transm. Dis.* **39,** 316–323 (2012).
26. Public Health Ontario. Guidelines for Testing and Treatment of Gonorrhea in Ontario. Quick Reference Guide. 1–2 (2013).
27. Westling-Häggström, B., Elmros, T., Normark, S. & Winblad, B. Growth pattern and cell division in Neisseria gonorrhoeae. *J. Bacteriol.* **129,** 333–342 (1977).
28. Ramirez-Arcos, S., Szeto, J., Dillon, J. A. R. & Margolin, W. Conservation of dynamic localization among minD and minE orthologues: Oscillation of Neisseria gonorrhoeae proteins in Escherichia coli. *Mol. Microbiol.* **46,** 493–504 (2002).
29. Szeto, J. *et al.* Gonococcal MinD affects cell division in Neisseria gonorrhoeae and Escherichia coli and exhibits a novel self-interaction. *Am. Soc. Microbiol.* **183,** 6253–6264 (2001).
30. Szeto, J., Eng, N. F., Acharya, S., Rigden, M. D. & Dillon, J. A. R. A conserved polar region in the cell division site determinant MinD is required for responding to MinE-induced oscillation but not for localization within coiled arrays. *Res. Microbiol.* **156,** 17–29 (2005).
31. Zhou, H. *et al.* Analysis of MinD mutations reveals residues required for MinE stimulation of the MinD ATPase and residues required for MinC interaction. *J. Bacteriol.* **187,** 629–638 (2005).
32. Wu, W., Park, K. T., Holyoak, T. & Lutkenhaus, J. Determination of the structure of the MinD-ATP complex reveals the orientation of MinD on the membrane and the relative location of the binding sites for MinE and MinC. *Mol. Microbiol.* **79,** 1515–1528 (2011).
33. Mileykovskaya, E. *et al.* Effects of phospholipid composition on MinD-membrane interactions in vitro and in vivo. *J. Biol. Chem.* **278,** 22193–22198 (2003).
34. Hu, Z. *et al.* Dynamic assembly of MinD on phospholipid vesicles regulated by ATP and MinE. *Proc. Natl. Acad. Sci. U. S. A.* **99,** 6761–6766 (2002).
35. Hu, Z. *et al.* Recruitment of MinC, an inhibitor of Z-ring formation, to the

membrane in Escherichia coli : role of MinD and MinE. *J. Bacteriol.* **185,** 196–203 (2003).

36. Hu, Z. & Lutkenhaus, J. A conserved sequence at the C-terminus of MinD is required for binding to the membrane and targeting MinC to the septum. *Mol. Microbiol.* **47,** 345–355 (2003).
37. Hu, Z., Mukherjee, a, Pichoff, S. & Lutkenhaus, J. The MinC component of the division site selection system in Escherichia coli interacts with FtsZ to prevent polymerization. *Proc. Natl. Acad. Sci. U. S. A.* **96,** 14819–14824 (1999).
38. Hu, Z. & Lutkenhaus, J. Analysis of MinC reveals two independent domains involved in interaction with MinD and FtsZ. *J. Bacteriol.* **182,** 3965–3971 (2000).
39. Hernández-Rocamora, V. M. *et al.* MinC protein shortens FtsZ protofilaments by preferentially interacting with GDP-bound subunits. *J. Biol. Chem.* **288,** 24625–24635 (2013).
40. Okuno, T., Ogoh, M., Tanina, H., Funasaki, N. & Kogure, K. Direct monitoring of interaction between Escherichia coli proteins, MinC and monomeric FtsZ, in solution. *Biol. Pharm. Bull.* **32,** 1473–5 (2009).
41. Park, K-T., Dajkovic, A., Wissel, M., Du, S. & Lutkenhaus, J. MinC and FtsZ mutant analysis provides insight into MinC/MinD-mediated Z Ring disassembly. *J. Biol. Chem.* **293,** 5834 –5846 (2018).
42. Hu, Z. & Lutkenhaus, J. Topological regulation of cell division in E. coli: Spatiotemporal oscillation of MinD requires stimulation of its ATPase by MinE and phospholipid. *Mol. Cell* **7,** 1337–1343 (2001).
43. Ghasriani, H. *et al.* Appropriation of the MinD protein-interaction motif by the dimeric interface of the bacterial cell division regulator MinE. *Proc. Natl. Acad. Sci. U. S. A.* **107,** 18416–18421 (2010).
44. Huang, J., Cao, C. & Lutkenhaus, J. Interaction between FtsZ and inhibitors of cell division. *J. Bacteriol.* **178,** 5080–5085 (1996).
45. Zhao, C. R., de Boer, P. a & Rothfield, L. I. Proper placement of the Escherichia coli division site requires two functions that are associated with different domains of the MinE protein. *Proc. Natl. Acad. Sci. U. S. A.* **92,** 4313–4317 (1995).
46. Raskin, D. M. & de Boer, P. A. Rapid pole-to-pole oscillation of a protein required

for directing division to the middle of Escherichia coli. *Proc. Natl. Acad. Sci. U. S. A.* **96,** 4971–4976 (1999).

47. Raskin, D. M. & Boer, P. a J. De. MinDE-dependent ole-to-pole oscillation of division inhibitor MinC in Escherichia coli. *J. Bacteriol.* **181,** 6419–6424 (1999).
48. Shih, Y-L., Le, T. & Rothfield, L. Division site selection in Escherichia coli involves dynamic redistribution of Min proteins within coiled structures that extend between the two cell poles. *Proc. Natl. Acad. Sci. U. S. A.* **100,** 7865–7870 (2003).
49. Raskin, D. M. & de Boer, P. a. The MinE ring: an FtsZ-independent cell structure required for selection of the correct division site in E. coli. *Cell* **91,** 685–694 (1997).
50. Hale, C. A., Meinhardt, H. & de Boer, P. A. Dynamic localization cycle of the cell division regulator MinE in Escherichia coli. *EMBO J.* **20,** 1563–72 (2001).
51. Raskin, D. M. & De Boer, P. A. J. MinDE-dependent pole-to-pole oscillation of division. *J. Bacteriol.* **181,** 6419–6424 (1999).
52. Vecchiarelli, A. G., Li, M., Mizuuchi, M. & Mizuuchi, K. Differential affinities of MinD and MinE to anionic phospholipid influence Min patterning dynamics in vitro. *Mol. Microbiol.* **93,** 453–463 (2014).
53. Loose, M., Fischer-Friedrich, E., Herold, C., Kruse, K. & Schwille, P. Min protein patterns emerge from rapid rebinding and membrane interaction of MinE. *Nat. Struct. Mol. Biol.* **18,** 577–583 (2011).
54. Vecchiarelli, A. G. *et al.* Membrane-bound MinDE complex acts as a toggle switch that drives Min oscillation coupled to cytoplasmic depletion of MinD. *Proc. Natl. Acad. Sci. U. S. A.* E1479–E1488 (2016).
55. Loose, M. *et al.* Spatial regulators for bacterial cell division self-organize into surface waves in vitro. *Science.* **320,** 789–792 (2008).
56. Ivanov, V. & Mizuuchi, K. Multiple modes of interconverting dynamic pattern formation by bacterial cell division proteins. *Proc. Natl. Acad. Sci. U. S. A.* **107,** 8071–8078 (2010).
57. Barák, I., Muchová, K., Wilkinson, A. J., O'Toole, P. J. & Pavlendová, N. Lipid spirals in Bacillus subtilis and their role in cell division. *Mol. Microbiol.* **68,** 1315–

1327 (2008).

58. Zhou, H. & Lutkenhaus, J. Membrane binding by MinD involves insertion of hydrophobic residues within the C-terminal amphipathic helix into the bilayer. *J. Bacteriol.* **185,** 4326–4335 (2003).

59. Szeto, T. H., Rowland, S. L., Habrukowich, C. L. & King, G. F. The MinD membrane targeting sequence is a transplantable lipid-binding helix. *J. Biol. Chem.* **278,** 40050–40056 (2003).

60. Suefuji, K., Valluzzi, R. & RayChaudhuri, D. Dynamic assembly of MinD into filament bundles modulated by ATP, phospholipids, and MinE. *Proc. Natl. Acad. Sci. U. S. A.* **99,** 16776–16781 (2002).

61. Mileykovskaya, E. & Dowhan, W. Role of membrane lipids in bacterial division-site selection. *Curr. Opin. Microbiol.* **8,** 135–142 (2005).

62. Sakai, N. *et al.* The three-dimensional structure of septum site-determining protein MinD from Pyrococcus horikoshii OT3 in complex with Mg-ADP. *Structure* **9,** 817–826 (2001).

63. Cordell, S. C. & Lowe, J. Crystal structure of the bacterial cell division regulator MinD. *FEBS Lett.* **492,** 160–165 (2001).

64. Hayashi, I. *et al*. Structural and functional studies of MinD ATPase: implications for the molecular recognition of the bacterial cell division apparatus. *EMBO J.* **20,** 1819–1828 (2001).

65. Leonard, T. A., Butler, P. J. & Löwe, J. Bacterial chromosome segregation: Structure and DNA binding of the Soj dimer - A conserved biological switch. *EMBO J.* **24,** 270–282 (2005).

66. Schindelin, H., Kisker, C., Schlessman, J. L., Howard, J. B. & Rees, D. C. Structure of ADP x AIF4(-)-stabilized nitrogenase complex and its implications for signal transduction. *Nature* **387,** 370–376 (1997).

67. Leipe, D. D., Wolf, Y. I., Koonin, E. V. & Aravind, L. Classification and evolution of P-loop GTPases and related ATPases. *J. Mol. Biol.* **317,** 41–72 (2002).

68. Hayashi, I. *et al*. Structural and functional studies of MinD ATPase: implications for the molecular recognition of the bacterial cell division apparatus. *EMBO J.* **20,** 1819–1828. (2001).

69. Park, K. T., Wu, W., Lovell, S. & Lutkenhaus, J. Mechanism of the asymmetric activation of the MinD ATPase by MinE. *Mol. Microbiol.* **85,** 271–281 (2012).

70. Zhou, H. & Lutkenhaus, J. MinC mutants deficient in MinD- and DicB-mediated cell division inhibition due to loss of interaction with MinD, DicB, or a septal component. *J. Bacteriol.* **187,** 2846–2857 (2005).

71. Ma, L. Y., King, G. & Rothfield, L. Mapping the MinE site involved in interaction with the MinD division site selection protein of Escherichia coli. *J. Bacteriol.* **185,** 4948–4955 (2003).

72. Hu, Z., Gogol, E. P. & Lutkenhaus, J. Dynamic assembly of MinD on phospholipid vesicles regulated by ATP and MinE. *Proc. Natl. Acad. Sci. U. S. A.* **99,** 6761–6766 (2002).

73. King, G. F. *et al.* The dimerization and topological specificity functions of MinE reside in a structurally autonomous C-terminal domain. *Mol. Microbiol.* **31,** 1161–1169 (1999).

74. Zhang, Y., Rowland, S., King, G., Braswell, E. & Rothfield, L. The relationship between hetero-oligomer formation and function of the topological specificity domain of the Escherichia coli MinE protein. *Mol. Microbiol.* **30,** 265–273 (1998).

75. Kang, G. *et al.* Crystal structure of Helicobacter pylori MinE, a cell division topological specificity factor. *Mol. Microbiol.* **76,** 1222–1231 (2010).

76. Larkin, M. A. *et al.* Clustal W and Clustal X version 2.0. *Bioinformatics* **23,** 2947–2948 (2007).

77. Park, K. T. *et al.* The min oscillator uses MinD-dependent conformational changes in MinE to spatially regulate cytokinesis. *Cell* **146,** 396–407 (2011).

78. Hsieh, C. W. *et al.* Direct MinE-membrane interaction contributes to the proper localization of MinDE in E. coli. *Mol. Microbiol.* **75,** 499–512 (2010).

79. Shih, Y. L. *et al.* The N-terminal Amphipathic Helix of the topological specificity factor mine is associated with shaping membrane curvature. *PLoS One* **6,** (2011).

80. Park, K., Villar, M. T., Artigues, A. & Lutkenhaus, J. MinE conformational dynamics regulate membrane binding , MinD interaction , and Min oscillation. *Proc. Natl. Acad. Sci. U. S. A.***114,** 7497–7504 (2017).

81. Rami Tzafriri, A. & Edelman, E. R. Quasi-steady-state kinetics at enzyme and

substrate concentrations in excess of the Michaelis-Menten constant. *J. Theor. Biol.* **245,** 737–748 (2007).

82. George, B. Y. & Briggs, E. A further note on the kinetics of enzyme action. *Biochem* **19,** 1037–1038 (1925).
83. Berg, Heremy. Tymoczko, John and Stryer, L. *Biochemistry*. (W H Freeman, 2002).
84. James, N. W. The Hill equation revisited: uses and misuses. *FASEB J.* **11,** 835–841 (1997).
85. Kelly, S. M., Jess, T. J. & Price, N. C. How to study proteins by circular dichroism. *Biochim. Biophys. Acta - Proteins Proteomics* **1751,** 119–139 (2005).
86. Yang, J. T. & Doty, P. The Optical rotatory dispersion of polypeptides and proteins in relation to configuration. *J. Am. Chem. Soc.* **79,** 761–775 (1957).
87. Johnson Jr., W. C. Secondary structure of proteins through circular dichroism spectroscopy. *Ann. Rev. Biophys. Biophys. Chem.* **17,** 145–66 (1988).
88. Johnson Jr., W. C. Protein secondary structure and circular dichroism: a practical guide. *Proteins Struct. Funct. Genet.* **7,** 205–214 (1990).
89. Greenfield, N. J. Using circular dichroism spectra to estimate protein secondary structure. *Nat. Protoc.* **1,** 2876–2890 (2007).
90. Whitmore, L. & Wallace, B. A. Protein secondary structure analyses from circular dichroism spectroscopy: Methods and reference databases. *Biopolymers* **89,** 392–400 (2008).
91. Lobley, A., Whitmore, L. & Wallace, B. A. DICHROWEB: An interactive website for the analysis of protein secondary structure from circular dichroism spectra. *Bioinformatics* **18,** 211–212 (2002).
92. Whitmore, L. & Wallace, B. A. DICHROWEB, an online server for protein secondary structure analyses from circular dichroism spectroscopic data. *Nucleic Acids Res.* **32,** 668–673 (2004).
93. Sreerama, N. & Woody, R. W. Estimation of protein secondary structure from circular dichroism spectra : comparison of CONTIN , SELCON , and CDSSTR methods with an expanded reference set. *Anal. Biochem.* **287,** 252–260 (2000).
94. Marion, D. An introduction to biological NMR spectroscopy. *Mol. Cell.*

Proteomics **12,** 3006–3025 (2013).

95. Yee, A. A. *et al.* Article NMR and X-ray crystallography , complementary tools in structural proteomics of small proteins. *J. Am. Chem. Soc.* **127,** 16512–16517 (2005).
96. Sugiki, T., Kobayashi, N. & Fujiwara, T. Modern technologies of solution nuclear magnetic resonance spectroscopy for three-dimensional structure determination of proteins open avenues for life scientists. *Comput. Struct. Biotechnol. J.* **15,** 328–339 (2017).
97. John, Cavanagh. Wayne, Fairbrother. Arthur, Palmer and Nicholas, S. *Protein NMR spectroscopy; principles and practice*. (Academic Press, 1996).
98. Keeler, J. *Understanding NMR spectroscopy*. (Wiley & sons, 2010).
99. Claridge, T. *High resolution NMR techniques in organic chemistry*. (Elsevier Science, 2008).
100. Levitt, M. *Spin Dynamics; basics of nuclear magnatic resonance.* (Wiley & sons, 2008).
101. Clore, G. M. & Gronenborn, A. M. NMR structure determination of proteins and protein complexes larger than 20 kDa. *Curr. Opin. Chem. Biol.* **2,** 564–570 (1998).
102. Wider, G. & Wüthrich, K. NMR spectroscopy of large molecules and multimolecular assemblies in solution. *Curr. Opin. Struct. Biol.* **9,** 594–601 (1999).
103. Kay, L. E., Ikura, M., Tschudin, R. & Bax, A. Three-dimensional triple-resonance NMR spectroscopy of isotopically enriched proteins. *J. Magn. Reson.* **89,** 496–514 (1990).
104. Grzesiekt, S. & Bax, A. Correlating Backbone Amide and Side Chain Resonances in Larger Proteins by Multiple Relayed Triple Resonance NMR. *J. Am. Chem. Soc.* **114,** 6291–6293 (1992).
105. Grzesiek, S. & Bax, A. An efficient experiment for sequential backbone assignment of medium-sized isotopically enriched proteins. *J. Magn. Reson.* **99,** 201–207 (1992).
106. Lawrence, B. *Protein NMR; Modren techniques and biomedical applications*. (Springer Sciences, 2015).

107. Ayed, S. H. *et al.* Dissecting the role of conformational change and membrane binding by the bacterial cell division regulator MinE in the stimulation of MinD ATPase activity. *J. Biol. Chem.* **292,** 20732–20743 (2017).

108. Chang, A. Y., Chau, V. W., Landas, J. A. & Yvonne. Preparation of calcium competent Escherichia coli and heat-shock transformation. *JEMI methods* **1,** 22–25 (2017).

109. Laemmli, U. K. Cleavage of structural proteins during the assembly of the head of bacteriophage T4. *Nature* **227,** 680–685 (1970).

110. Sreerama, N. & Woody, R. W. A self-consistent method for the analysis of protein secondary structure from circular dichroism. *Analytical Biochemistry* **209,** 32–44 (1993).

111. Provencher, S. W. & Glöckner, J. Estimation of globular protein secondary structure from circular dichroism. *Biochemistry* **20,** 33–37 (1981).

112. Delaglio, F. *et al.* NMRPipe: A multidimensional spectral processing system based on UNIX pipes. *J. Biomol. NMR* **6,** 277–293 (1995).

113. Johnson, B. A. & Blevins, R. A. NMR View: A computer program for the visualization and analysis of NMR data. *J. Biomol. NMR* **4,** 603–614 (1994).

114. Williamson, M. P. Using chemical shift perturbation to characterise ligand binding. *Prog. Nucl. Magn. Reson. Spectrosc.* **73,** 1–16 (2013).

115. Wishart, D. S., Sykes, B. D. & Richards, F. M. The chemical shift index : a fast and simple method for the assignment of protein secondary structure through NMR spectroscopy. *Biochemistry* **31,** 1647–1651 (1992).

116. Zheng, M. *et al.* Self-assembly of MinE on the membrane underlies formation of the MinE ring to sustain function of the Escherichia coli Min system. *J. Biol. Chem.* **289,** 21252–21266 (2014).

117. Renner, L. D. & Weibel, D. B. MinD and MinE interact with anionic phospholipids and regulate division plane formation in Escherichia coli. *J. Biol. Chem.* **287,** 38835–38844 (2012).

118. Taghbalout, A., Ma, L. & Rothfield, L. Role of MinD-membrane association in min protein interactions. *J. Bacteriol.* **188,** 2993–3001 (2006).

119. Fu, X., Shih, Y. L., Zhang, Y. & Rothfield, L. I. The MinE ring required for proper

placement of the division site is a mobile structure that changes its cellular location during the Escherichia coli division cycle. *Proc. Natl. Acad. Sci. U. S. A.* **98,** 980–985 (2001).

120. Huang, K. C., Meir, Y. & Wingreen, N. S. Dynamic structures in Escherichia coli: Spontaneous formation of MinE rings and MinD polar zones. *Proc. Natl. Acad. Sci. U. S. A.* **100,** 12724–12728 (2003).
121. Zieske, K. & Schwille, P. Reconstitution of pole-to-pole oscillations of min proteins in microengineered polydimethylsiloxane compartments. *Angew. Chem. Int. Ed.* **52,** 459–462 (2013).
122. Zieske, K., Schweizer, J. & Schwille, P. Surface topology assisted alignment of Min protein waves. *FEBS Lett.* **588,** 2545–2549 (2014).
123. Zieske, K. & Schwille, P. Reconstitution of self-organizing protein gradients as spatial cues in cell-free systems. *Elife* **3,** 1–19 (2014).
124. Sengupta, S., Derr, J., Sain, A. & Rutenberg, A. D. Stuttering Min oscillations within E. coli bacteria: A stochastic polymerization model. *Phys. Biol.* **9,** (2012).
125. Walsh, J. C., Angstmann, C. N., Duggin, I. G. & Curmi, P. M. G. Molecular interactions of the Min protein system reproduce spatiotemporal patterning in growing and dividing Escherichia coli cells. *PLoS One* **10,** 1–23 (2015).
126. Bonny, M., Fischer-Friedrich, E., Loose, M., Schwille, P. & Kruse, K. Membrane binding of MinE allows for a comprehensive description of Min-protein pattern formation. *PLoS Comput. Biol.* **9,** (2013).
127. Meacci, G. *et al.* Mobility of Min-proteins in Escherichia coli measured by fluorescence correlation spectroscopy. *Phys. Biol.* **3,** 255–263 (2006).
128. Lackner, L. L., Raskin, D. M. & De Boer, P. A. J. ATP-dependent interactions between *Escherichia coli* Min proteins and the phospholipid membrane *in vitro*. *J. Bacteriol.* **185,** 735–749 (2003).
129. Unemo, M. & Shafer, W. M. Antimicrobial resistance in Neisseria gonorrhoeae in the 21st Century: Past, evolution, and future. *Clin. Microbiol. Rev.* **27,** 587–613 (2014).
130. Parti, R. P. *et al.* Attenuated virulence of min operon mutants of Neisseria gonorrhoeae and their interactions with human urethral epithelial cells. *Microbes*

Infect. **13,** 545–554 (2011).

131. Sud, I. J. & Feingold, D. S. Phospholipids and fatty acids of Neisseria gonorrhoeae. *J. Bacteriol.* **124,** 713–717 (1975).
132. Morein, S. *et al*. Wild-type Escherichia coli cells regulate the membrane lipid composition in a " Window " between Gel and non-lamellar structures. *J. Biol. Chem.* **271,** (12) 6801–6809 (1996).
133. Su, J. *et al.* Genome-wide identification of Francisella tularensis virulence determinants. *Infect. Immun.* **75,** 3089–3101 (2007).
134. Anthony, L., Cowley, S., Mdluli, K. & Nano, F. Isolation of a Francisella tularensis mutant that is sensitive to serum and oxidative killing and is avirulent in mice: Correlation with the loss of MinD homologue expression. *FEMS Microbiol. Lett.* **124,** 157–165 (1995).
135. Parti, R. P., Biswas, D., Wang, M., Liao, M. & Dillon, J. A. R. A MinD mutant of enterohemorrhagic E. coli O157:H7 has reduced adherence to human epithelial cells. *Microb. Pathog.* **51,** 378–383 (2011).
136. Shih, Y.-L. & Zheng, M. Spatial control of the cell division site by the Min system in *Escherichia coli*. *Environ. Microbiol.* **15,** 3229–3239 (2013).
137. Leger, M. M. *et al.* An ancestral bacterial division system is widespread in eukaryotic mitochondria. *Proc. Natl. Acad. Sci. U. S. A.* **112,** 10239–10246 (2015).
138. Hafizi, F. Characterization of the interactions of the bacterial cell division regulator MinE. (University of Ottawa, 2012).
139. Lackner, L. L., Raskin, D. M. & De Boer, P. A. J. ATP-dependent interactions between Escherichia coli Min proteins and the phospholipid membrane in vitro. *J. Bacteriol.* **185,** 735–749 (2003).
140. Kay, L. E. NMR studies of protein structure and dynamics. *J. Magn. Reson.* **173,** 193–207 (2005).
141. Xu, Y. & Matthews, S. in (eds. Heise, H. & Matthews, S.) 97–119 (Springer Berlin Heidelberg, 2011).
142. Mazor, S. *et al.* Mutual effects of MinD-membrane interaction: II. Domain structure of the membrane enhances MinD binding. *Biochim. Biophys. Acta - Biomembr.* **1778,** 2505–2511 (2008).

143. Mazor, S. *et al.* Mutual effects of MinD-membrane interaction: I. Changes in the membrane properties induced by MinD binding. *Biochim. Biophys. Acta - Biomembr.* **1778,** 2496–2504 (2008).

144. Silvius, J. R. *Thermotropic phase transitions of pure lipids in model membranes and their modifications by membrane proteins*. (John Wiley & Sons, Inc, 1982).

145. Caffrey, M. *Lipid thermotropic phase transition database (LIPIDAT): User's Guide.* (1993).

146. Denk, J. *et al.* MinE conformational switching confers robustness on self-organized Min protein patterns. *Proc. Natl. Acad. Sci. U. S. A.* **115** (18): 4553-4558 (2018).

147. Chen, Y., Milam, S. L. & Erickson, H. P. SulA inhibits assembly of FtsZ by a simple sequestration mechanism. *Biochemistry* **51,** 3100−3109 (2012).

148. Murata, K. & Wolf, M. Cryo-electron microscopy for structural analysis of dynamic biological macromolecules. *Biochim. Biophys. Acta - Gen. Subj.* **1862,** 324–334 (2018).

149. Vonck, J. & Mills, D. J. Advances in high-resolution cryo-EM of oligomeric enzymes. *Curr. Opin. Struct. Biol.* **46,** 48–54 (2017).

150. Merk, A. *et al.* Breaking cryo-EM resolution barriers to facilitate drug discovery. *Cell* **165,** 1698–1707 (2016).

151. Bai, X. *et al.* An atomic structure of human γ-secretase. *Nature* **525,** 212 (2015).

152. Nogales, E. & Scheres, S. H. W. Cryo-EM: A unique tool for the visualization of macromolecular complexity. *Mol. Cell* **58,** 677–689 (2015).

153. Thompson, R. F., Walker, M., Siebert, C. A., Muench, S. P. & Ranson, N. A. An introduction to sample preparation and imaging by cryo-electron microscopy for structural biology. *Methods* **100,** 3–15 (2016).

154. Szeto, T. H., Rowland, S. L., Rothfield, L. I. & King, G. F. Nonlinear partial differential equations and applications: Membrane localization of MinD is mediated by a C-terminal motif that is conserved across eubacteria, archaea, and chloroplasts. *Proc. Natl. Acad. Sci. U. S. A.* **99,** 15693–15698 (2002).

155. Ayed, S. Investigation of the effect of changes in lipid bilayer properties on the activity of the bacterial cell division regulator protein MinD. (University of

Ottawa, 2012).

156. Glock, P. *et al.* Optical control of a biological reaction–diffusion system. *Angew. Chem. Int. Ed.* **57,** 2362–2366 (2018).

157. Mojsoska, B., Carretero, G., Larsen, S., Mateiu, R. V. & Jenssen, H. Peptoids successfully inhibit the growth of gram negative E. coli causing substantial membrane damage. *Sci. Rep.* **7,** 1–12 (2017).

158. Chongsiriwatana, N. P. *et al.* Peptoids that mimic the structure, function, and mechanism of helical antimicrobial peptides. *Proc. Natl. Acad. Sci. U. S. A.* **105,** 2794–2799 (2008).

Figure 1.1

ELSEVIER LICENSE
TERMS AND CONDITIONS

Mar 15, 2018

This Agreement between Mr. Saud Ayed ("You") and Elsevier ("Elsevier") consists of your license details and the terms and conditions provided by Elsevier and Copyright Clearance Center.

License Number	4310280193465
License date	Mar 15, 2018
Licensed Content Publisher	Elsevier
Licensed Content Publication	Cell
Licensed Content Title	A division inhibitor and a topological specificity factor coded for by the minicell locus determine proper placement of the division septum in E. coli
Licensed Content Author	Piet A.J. de Boer,Robin E. Crossley,Lawrence I. Rothfield
Licensed Content Date	Feb 24, 1989
Licensed Content Volume	56
Licensed Content Issue	4
Licensed Content Pages	9
Start Page	641
End Page	649
Type of Use	reuse in a thesis/dissertation
Intended publisher of new work	other
Portion	figures/tables/illustrations
Number of figures/tables/illustrations	1
Format	both print and electronic
Are you the author of this Elsevier article?	No
Will you be translating?	No
Original figure numbers	figure 1
Title of your thesis/dissertation	Invesitgation of the role of MinE-membrane interaction and conformational change in modulation of MinD ATP hydrolysis
Expected completion date	May 2018
Estimated size (number of pages)	200
Requestor Location	Mr. Saud Ayed 10 marie curie private ottawa, ON k1n9a4 Canada Attn: Mr. Saud Ayed
Publisher Tax ID	GB 494 6272 12

Figure 1.3

JOHN WILEY AND SONS LICENSE TERMS AND CONDITIONS

Mar 15, 2018

This Agreement between Mr. Saud Ayed ("You") and John Wiley and Sons ("John Wiley and Sons") consists of your license details and the terms and conditions provided by John Wiley and Sons and Copyright Clearance Center.

License Number	4310270464043
License date	Mar 15, 2018
Licensed Content Publisher	John Wiley and Sons
Licensed Content Publication	The EMBO Journal
Licensed Content Title	Dynamic localization cycle of the cell division regulator MinE in Escherichia coli
Licensed Content Author	Cynthia A. Hale,Hans Meinhardt,Piet A.J. de Boer
Licensed Content Date	Apr 2, 2001
Licensed Content Pages	10
Type of use	Dissertation/Thesis
Requestor type	University/Academic
Format	Print and electronic
Portion	Figure/table
Number of figures/tables	3
Original Wiley figure/table number(s)	Figure 2, 3, 4 and 6
Will you be translating?	No
Title of your thesis / dissertation	Invesitgation of the role of MinE-membrane interaction and conformational change in modulation of MinD ATP hydrolysis
Expected completion date	May 2018
Expected size (number of pages)	200
Requestor Location	Mr. Saud Ayed 10 marie curie private ottawa, ON k1n9a4 Canada Attn: Mr. Saud Ayed
Publisher Tax ID	EU826007151
Total	0.00 CAD

Figure 1.4

THE AMERICAN ASSOCIATION FOR THE ADVANCEMENT OF SCIENCE LICENSE TERMS AND CONDITIONS

May 30, 2018

This Agreement between Mr. Saud Ayed ("You") and The American Association for the Advancement of Science ("The American Association for the Advancement of Science") consists of your license details and the terms and conditions provided by The American Association for the Advancement of Science and Copyright Clearance Center.

License Number	4358580836779
License date	May 30, 2018
Licensed Content Publisher	The American Association for the Advancement of Science
Licensed Content Publication	Science
Licensed Content Title	Spatial Regulators for Bacterial Cell Division Self-Organize into Surface Waves in Vitro
Licensed Content Author	Martin Loose,Elisabeth Fischer-Friedrich,Jonas Ries,Karsten Kruse,Petra Schwille
Licensed Content Date	May 9, 2008
Licensed Content Volume	320
Licensed Content Issue	5877
Volume number	320
Issue number	5877
Type of Use	Thesis / Dissertation
Requestor type	Scientist/individual at a research institution
Format	Print and electronic
Portion	Figure
Number of figures/tables	1
Order reference number	
Title of your thesis / dissertation	Invesitgation of the role of MinE-membrane interaction and conformational change in modulation of MinD ATP hydrolysis
Expected completion date	May 2018
Estimated size(pages)	200
Requestor Location	Mr. Saud Ayed 10 marie curie private ottawa, ON k1N9A4 Canada Attn: Mr. Saud Ayed
Billing Type	Invoice
Billing Address	Mr. Saud Ayed 10 marie curie private ottawa, ON k1N9A4 Canada Attn: Mr. Saud Ayed

SPRINGER NATURE LICENSE TERMS AND CONDITIONS

May 30, 2018

This Agreement between Mr. Saud Ayed ("You") and Springer Nature ("Springer Nature") consists of your license details and the terms and conditions provided by Springer Nature and Copyright Clearance Center.

License Number	4358590850850
License date	May 30, 2018
Licensed Content Publisher	Springer Nature
Licensed Content Publication	Nature Structural & Molecular Biology
Licensed Content Title	Min protein patterns emerge from rapid rebinding and membrane interaction of MinE
Licensed Content Author	Martin Loose, Elisabeth Fischer-Friedrich, Christoph Herold, Karsten Kruse, Petra Schwille
Licensed Content Date	Apr 24, 2011
Licensed Content Volume	18
Licensed Content Issue	5
Type of Use	Thesis/Dissertation
Requestor type	academic/university or research institute
Format	print and electronic
Portion	figures/tables/illustrations
Number of figures/tables/illustrations	1
High-res required	no
Will you be translating?	no
Circulation/distribution	501 to 1000
Author of this Springer Nature content	no
Title	Invesitgation of the role of MinE-membrane interaction and conformational change in modulation of MinD ATP hydrolysis
Instructor name	n/a
Institution name	n/a
Expected presentation date	May 2018
Portions	Fig 3
Requestor Location	Mr. Saud Ayed 10 marie curie private ottawa, ON k1N9A4 Canada Attn: Mr. Saud Ayed
Billing Type	Invoice
Billing Address	Mr. Saud Ayed 10 marie curie private

Figure 1.16

JOHN WILEY AND SONS LICENSE TERMS AND CONDITIONS

May 30, 2018

This Agreement between Mr. Saud Ayed ("You") and John Wiley and Sons ("John Wiley and Sons") consists of your license details and the terms and conditions provided by John Wiley and Sons and Copyright Clearance Center.

License Number	4321711173717
License date	Apr 04, 2018
Licensed Content Publisher	John Wiley and Sons
Licensed Content Publication	Biopolymers
Licensed Content Title	Protein secondary structure analyses from circular dichroism spectroscopy: Methods and reference databases
Licensed Content Author	Lee Whitmore, B. A. Wallace
Licensed Content Date	Sep 25, 2007
Licensed Content Volume	89
Licensed Content Issue	5
Licensed Content Pages	9
Type of use	Dissertation/Thesis
Requestor type	University/Academic
Format	Print and electronic
Portion	Figure/table
Number of figures/tables	1
Original Wiley figure/table number(s)	1
Will you be translating?	No
Title of your thesis / dissertation	Invesitgation of the role of MinE-membrane interaction and conformational change in modulation of MinD ATP hydrolysis
Expected completion date	May 2018
Expected size (number of pages)	200
Requestor Location	Mr. Saud Ayed 10 marie curie private ottawa, ON k1N9A4 Canada Attn: Mr. Saud Ayed
Publisher Tax ID	EU826007151
Total	0.00 USD
Terms and Conditions	

TERMS AND CONDITIONS

This copyrighted material is owned by or exclusively licensed to John Wiley & Sons, Inc. or one of its group companies (each a"Wiley Company") or handled on behalf of a society with which a Wiley Company has exclusive publishing rights in relation to a particular work